

Jagiellonian University
The Faculty of Physics, Astronomy
and Applied Computer Science
Marian Smoluchowski Institute of Physics

Isospin dependence of the η' meson production in nucleon–nucleon collisions

Joanna Klaja

Ph.D. dissertation prepared at the Nuclear Physics Department
of the Marian Smoluchowski Institute of Physics of the Jagiellonian University
and at the Institute for Nuclear Physics in the Research Centre Jülich
guided by: Prof. Paweł Moskal

Cracow 2009

Abstract

The upper limit of the total cross section for quasi-free $pn \rightarrow pn\eta'$ reaction has been determined in the excess energy range near the kinematical threshold.

The measurement has been carried out at the COSY-11 detection setup using a proton beam and a deuteron cluster target. The identification of the η' meson has been performed using the missing mass technique. The energy dependence of the upper limit of the cross section is extracted with a fixed proton beam momentum of $p_{beam} = 3.35$ GeV/c and exploiting the Fermi momenta of nucleons inside the deuteron. The data cover a range of centre-of-mass excess energies from 0 to 24 MeV.

The experimentally determined upper limit of the ratio $R_{\eta'} = \frac{\sigma(pn \rightarrow pn\eta')}{\sigma(pp \rightarrow pp\eta')}$, which is smaller than the ratio for the η meson, excludes the excitation of the $S_{11}(1535)$ resonance as a dominant production mechanism of the η' meson in nucleon-nucleon collisions. At the same time, the determined upper limits of $R_{\eta'}$ go in the direction of what one would expect in the glue production and production via mesonic currents. For quantitative tests of these mechanisms an order of magnitude larger statistics and a larger energy range would be required. This can be reached with the WASA-at-COSY facility.

Streszczenie

Górna granica całkowitego przekroju czynnego dla kwazi-swobodnej reakcji $pn \rightarrow pn\eta'$ została wyznaczona w przyprogowym obszarze energii.

Pomiar został przeprowadzony wykorzystując układ detekcyjny COSY-11, wiązkę protonową oraz klastrową tarczę deuteronową. Mezon η' został zidentyfikowany przy użyciu techniki masy brakującej. Zależność górnej granicy całkowitego przekroju czynnego od energii (funkcję wzbudzenia) przy stałej wartości pędu wiązki $p_{beam} = 3.35$ GeV/c, uzyskano dzięki pędowi Fermiego nukleonów w deuteronie. Dane zostały zmierzone w przedziale energii nadprogowej Q od 0 MeV do 24 MeV.

Otrzymana górna granica stosunku $R_{\eta'}$ całkowitych przekrojów czynnych dla reakcji $pn \rightarrow pn\eta'$ i $pp \rightarrow pp\eta'$, której wartość okazała się być znacznie mniejsza od analogicznego stosunku zmierzonego dla mezonu η , wyklucza hipotezę iż dominującym procesem w produkcji mezonu η' jest wzbudzenie rezonansu $S_{11}(1535)$. Równocześnie, uzyskany wynik nie wyklucza innych mechanizmów produkcji mezonu η' takich jak prądy mezonowe czy wzbudzenie gluonów.

Dla przeprowadzenia ilościowych testów możliwych mechanizmów produkcji mezonu η' wymagane jest wykonanie eksperymentu z większą statystyką oraz w większym zakresie energii. Taką możliwość daje układ detekcyjny WASA-at-COSY.

Contents

1	Introduction	7
2	Motivation	11
3	Spectator model	19
4	Experimental tools	25
4.1	Cooler Synchrotron COSY	25
4.2	COSY-11 facility	26
4.3	Measurement method – general remarks	28
5	Calibration of the detectors	31
5.1	Time-space calibration of the drift chambers	31
5.2	Time calibration of the S1 and S3 hodoscopes	32
5.3	The neutral particle detector	34
5.3.1	Time signals from a single detection unit	36
5.3.2	Relative timing between modules	37
5.3.3	General time offset and the time walk correction	39
5.3.4	Efficiency determination	43
5.4	Veto detector	44
5.5	Spectator detector	46
5.5.1	Scheme of the spectator detector	46
5.5.2	Energy calibration and position optimization	48
6	Analysis of the experimental data	51
6.1	Event selection	51
6.1.1	Proton identification	51
6.1.2	Neutron identification	52
6.2	Determination of the excess energy	53
6.3	Identification of the $pn \rightarrow pn\eta'$ reaction	57
6.3.1	Method of background subtraction	59
6.3.2	Background subtracted missing mass distribution	62
7	Luminosity determination	65

8	Excitation function	73
8.1	Upper limit of the total cross section	73
8.2	Ratio	75
9	Comparison with model predictions	77
10	Summary and perspectives	79
A	Precision of the neutron momentum determination	81
B	Parameterisation of the $pp \rightarrow pp\eta'$ total cross section	83

1. Introduction

The main aim of the studies presented in this thesis is the determination of the excitation function of the total cross section for the quasi-free $pn \rightarrow pn\eta'$ reaction near the kinematical threshold.

Despite the fact that the η and η' mesons - which are members of the ground-state pseudoscalar nonet [1] - were discovered many decades ago, they are still subject of many theoretical and experimental investigations.

According to the quark model, η and η' mesons can be described as a mixture of the singlet and octet states of the SU(3) - flavour pseudoscalar meson nonet. Within the one mixing angle scheme, a small mixing angle ($\theta = -15.5^\circ$) implies that the masses of η and η' mesons should be almost equal. However, masses of these mesons differ by about a factor of two. Additionally, the mass of the η' meson does not fit into the SU(3) scheme and it is thought to be induced by the gluonic component in its wave function. This hypothesis is strengthened by the decay scheme of mesons like B^+ or D_s^+ since the branching ratios of the decay of these mesons into some channels involving η' are significantly higher than the analogous for η especially in processes requiring the involvement of gluons [2, 3, 4].

The properties of the η' meson should manifest itself in the production mechanism in the collisions of nucleons. At present there is not much known about the relative contribution of the possible reaction mechanisms of the η' meson production in nucleon-nucleon collisions. It is expected that the η' meson can be produced through heavy meson exchange, through the excitation of an intermediate resonance or via the fusion of virtual mesons [5, 6, 7]. However, it is not possible to judge about the mechanism responsible for the η' meson production only from the total cross section of the $pp \rightarrow pp\eta'$ reaction [8]. Therefore, one has to investigate the η' production more detailed by e.g. selecting separate channels in the relevant degrees of freedom like the isospin which means a comparison of both, proton-proton and proton-neutron scattering. This conclusion motivated our investigations, which are presented in this thesis.

A comparison of the close-to-threshold total cross section for the η' production in both $pp \rightarrow pp\eta'$ and $pn \rightarrow pn\eta'$ reactions constitutes a tool not only to investigate the production of the η' meson in channels of isospin $I = 1$ and $I = 0$ but also may provide insight into the flavour-singlet (perhaps also into gluonium) content of the η' meson and the relevance of quark-gluon or hadronic degrees of freedom in the creation process. It is also possible that the η' meson is produced from excited glue in the interaction region of the colliding nucleons, which couple to the η' meson directly via its gluonic component or through its SU(3)-flavour-singlet admixture [9, 10]. As suggested in reference [11], η' production via the colour-singlet object does not depend on the total isospin of the colliding nucleons and should lead to the same production amplitude for

the η' in the $pn \rightarrow pn\eta'$ and $pp \rightarrow pp\eta'$ reactions. In case of the η meson, the ratio of the total cross sections for the reactions $pn \rightarrow pn\eta$ and $pp \rightarrow pp\eta$ was determined to be $R_\eta = 6.5$ in the excess energy range from ≈ 15 MeV to ≈ 160 MeV [12], what suggests the dominance of isovector meson exchange in the η production in nucleon-nucleon collisions. Since the fractional amounts of different quark flavours of η and η' mesons are very similar, in case of the dominant isovector meson exchange – by the analogy to the η meson production – we can expect that the ratio $R_{\eta'}$ should also be about 6.5. If however the η' meson is produced via its flavour-blind gluonium component from the colour-singlet glue excited in the interaction region the ratio should approach unity after corrections for the initial and final state interactions. The close-to-threshold excitation function for the $pp \rightarrow pp\eta'$ reaction has been determined in previous experiments [13, 14, 15, 16, 17] and the determination of the total cross section for the η' meson production in the proton-neutron interaction constitutes the main motivation for the experiment which is subject of this thesis.

It is worth to stress that the $pn \rightarrow pn\eta'$ reaction was never investigated so far. Such studies are challenging experimentally because the total cross section is expected to be about a factor of forty to hundred less than in case of the η meson and additionally (in comparison to the η near threshold production) the cross section of the multi-pion background grows significantly. For some channels (like eg. 3π) even by more than a few orders of magnitude [18]. The measurement of the $pn \rightarrow pn\eta'$ reaction is also much more difficult in comparison to the $pp \rightarrow pp\eta'$ reaction due to the neutron in the final state and the lack of a pure neutron target.

The experiment described in this thesis has been performed by the COSY-11 collaboration by means of the COSY-11 facility at the Cooler Synchrotron COSY at the Research Centre Jülich in Germany. A quasi-free proton-neutron reaction was induced by a proton beam impinging on a deuteron target. For the data analysis the proton from the deuteron is considered as a spectator which does not interact with the bombarding proton, but escapes untouched and hits the detector carrying the Fermi momentum possessed at the time of the reaction. The experiment is based on the registration of all outgoing nucleons from the $pd \rightarrow ppnX$ reaction. Protons moving forward are measured in two drift chambers and scintillator detectors and the neutron is registered in the neutral particle detector. Protons considered as a spectator are measured by a dedicated silicon-pad detector. The total energy available for the quasi-free proton-neutron reaction can be calculated for each event from the vector of the momenta of the spectator and beam protons. The absolute momentum of the neutron is determined from the time-of-flight between the target and the neutron detector. Application of the missing mass technique allows to identify events of the creation of the meson under investigation.

The thesis is divided into ten chapters. The second chapter - following the introduction - describes briefly the motivation for investigating of the $NN \rightarrow NN\eta'$ process, in particular in view of the study of the η' production mechanism and its structure. In this chapter the most interesting issues concerning the η' physics are presented, and

different possible production mechanisms and the predictions of the total cross section for the $pn \rightarrow pn\eta'$ reaction are given.

The spectator model is introduced in chapter three, with the description of the quasi-free meson production.

An introduction of the cooler synchrotron COSY and the COSY-11 detection setup is presented in the fourth chapter.

The fifth chapter is devoted to the calibration of the detectors. A special emphasis is put on the neutral particle and spectator detectors, two new devices which enabled to measure the quasi-free $pn \rightarrow pnX$ reactions.

A detailed description of the data analysis and the result of the identification of the $pn \rightarrow pn\eta'$ reaction are presented in chapter six.

The seventh chapter is devoted to the determination of the luminosity based on the quasi-free proton-proton elastic scattering.

Upper limits of the total cross section as well as of the ratio $R_{\eta'} = \sigma(pn \rightarrow pn\eta') / \sigma(pp \rightarrow pp\eta')$ are given in chapter eight.

The results of the analysis are compared to theoretical predictions in chapter nine.

The tenth chapter comprises the summary and perspectives. In particular the possibility to study of the η' production in the pure isospin $I = 0$ channel via the $pn \rightarrow d\eta'$ is discussed.

2. Motivation

Understanding of the structure of hadrons is a long standing challenge. Quantum chromodynamics (QCD) is the well established theory of strong interactions that describes the underlying forces of coloured quarks which bind them together to form the colour neutral hadrons observed in nature. However, due to the increasing coupling constant with decreasing energy this theory does not allow at present for the exact description of the hadron structure in the low energy domain. One of the hadrons which is especially intriguing is the η' meson.

The η' meson was first observed in 1964 [19, 20] in the reaction $K^- p \rightarrow \Lambda \eta'$. Although the η and η' mesons – the members of the nonet of the lightest pseudoscalar mesons – have been discovered many decades ago, they are still subject of considerable interest of theoretical as well as experimental studies. Particularly in case of the η' meson, despite more than forty years of investigations, its structure and properties, as well as the production mechanism in collisions involving hadrons are still not well determined.

According to the quark model, the two physical states of the η and η' mesons are considered as a mixture of the SU(3) pseudoscalar octet (η_8) and singlet (η_1) states with the pseudoscalar mixing angle θ_P :

$$\begin{aligned} |\eta\rangle &= \cos\theta_P |\eta_8\rangle - \sin\theta_P |\eta_1\rangle, \\ |\eta'\rangle &= \sin\theta_P |\eta_8\rangle + \cos\theta_P |\eta_1\rangle, \end{aligned} \quad (2.1)$$

where, following the notation introduced by Gilman and Kaufman [21] and previous work by Rosner [22], the SU(3) pseudoscalar octet state η_8 and singlet state η_1 are:

$$|\eta_8\rangle = \frac{1}{\sqrt{6}} |u\bar{u} + d\bar{d} - 2s\bar{s}\rangle, \quad |\eta_1\rangle = \frac{1}{\sqrt{3}} |u\bar{u} + d\bar{d} + s\bar{s}\rangle. \quad (2.2)$$

The value of the $\eta - \eta'$ mixing angle in the pseudoscalar meson nonet has been discussed many times in the last years [23]. The most up to date value of the mixing angle θ_P , averaged over all present experimental results, amounts to $\theta_P = -15.5^\circ \pm 1.3^\circ$ [23]. Such small mixing angle implies similar amounts of strange and nonstrange quark content:

$$\begin{aligned} |\eta\rangle &= 0.77 \cdot \frac{1}{\sqrt{2}} (u\bar{u} + d\bar{d}) - 0.63 \cdot s\bar{s}, \\ |\eta'\rangle &= 0.63 \cdot \frac{1}{\sqrt{2}} (u\bar{u} + d\bar{d}) - 0.77 \cdot s\bar{s}. \end{aligned} \quad (2.3)$$

This suggests that the masses of both η and η' mesons should be almost equal. However, the values of these masses differ by about a factor of two. Concurrently, the mass of the η' meson does not fit utterly to the SU(3) scheme. More surprisingly, the masses of all the pseudoscalar mesons, vector mesons and baryons are well described in terms of the naive quark model.

There are more differences in the physical properties of both mesons. For example: excited states of nucleons exists which decay via the emission of the η meson, yet none of the baryon resonances decay via the emission of the η' meson [1]. Very high η' apperance in the decays of B and D_S mesons [24, 25, 26] are observed. The branching ratio for $B^+ \rightarrow K^+\eta' = (6.5 \pm 1.7) \cdot 10^{-5}$ is much larger than the one for the corresponding η channel $B^+ \rightarrow K^+\eta < 1.4 \cdot 10^{-5}$ [24]. Similar relations are found in the decay of the D_S meson where $\frac{\Gamma(D_S^+ \rightarrow \eta' \rho^+)}{\Gamma(D_S^+ \rightarrow \eta' e^+ \nu)} = 12.0 \pm 4.3$ exceeds $\frac{\Gamma(D_S^+ \rightarrow \eta \rho^+)}{\Gamma(D_S^+ \rightarrow \eta e^+ \nu)} = 4.4 \pm 1.2$ by a factor of about three [25, 26]. It is worth to stress that the observed branching ratios do not agree with the predictions which ignore the gluonic content of the η' [2].

There exist also essential differences between the production of η and η' meson in proton-proton collisions close-to-threshold. The total cross section for the $pp \rightarrow pp\eta'$ reaction is by a factor of fourty smaller than the cross section for the $pp \rightarrow pp\eta$ reaction at corresponding values of the excess energy. The shape of the excitation function is also different indicating that the η meson interaction with nucleons is much stronger than the η' -nucleon one [8]. Thus, it is expected that not only physical properties but also the production mechanisms of these mesons should differ from each other.

As was already discussed, the η' meson with its mass of $m_{\eta'} \sim 958 \text{ MeV}$ is far from being "light" and its mass is almost three times larger than the value expected if this meson would be a pure Goldstone boson associated with spontaneously broken chiral symmetry [27]. The much larger mass of the η' meson is thought to be induced by the non-perturbative gluon dynamics [28, 29, 30] and the axial anomaly $U_A(1)$ [31]. A gluonic component of the η' meson is introduced as a flavour singlet state additionally to the η_1 , which couples directly to the glue [32]. Thus, the η' meson can couple to gluons not only via the quark and antiquark triangle loop but also directly through its gluonic admixture as shown in figure 2.1.

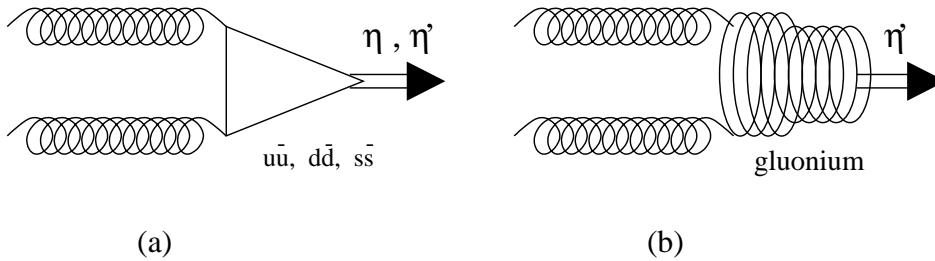


Figure 2.1: Coupling of η and η' to two gluons through quark and anti-quark triangle loop (a) and through gluonic admixture (b). Figure and caption are adapted from reference [32].

Experimental indications exist that the gluonic content of the η' meson constitutes a significant fraction of the η' meson wave function. For example, the unexpected large branching ratio measured for the decay of beauty particles, $B \rightarrow \eta' + X$ [24], has been interpreted as a possible experimental evidence in this respect [33]. Recently, the KLOE collaboration has estimated the gluonium fractional content of the η' meson to be $14\% \pm 4\%$ [34] by looking for the radiative decays $\phi \rightarrow \eta'\gamma$ and $\phi \rightarrow \eta\gamma$.

The most remarkable feature – in the frame of the quark model – distinguishing the η' meson from all other pseudoscalar and vector ground state mesons, is the fact, that the η' is predominantly a flavour-singlet combination of quark-antiquark pairs and therefore can mix with purely gluonic states. In any case, if there is a strong coupling of the η' meson to gluons, quark-gluon degrees of freedom may play a significant role in the production dynamics of this meson, especially close-to-threshold where the η' production requires a large momentum transfer between the nucleons and hence can occur only at short distances ~ 0.3 fm in the nucleon-nucleon collision. The role of gluonic degrees of freedom in the η' -nucleon system can be investigated for example through the flavour-singlet Goldberger-Treiman relation [35]:

$$2m_N G_A(0) = F g_{NN\eta'}(0) + \frac{F^2}{2N_F} m_{\eta'} g_{NNG}(0), \quad (2.4)$$

which relates the nucleon-nucleon- η' coupling constant $g_{NN\eta'}$ with the flavour-singlet axial constant $G_A(0)$. The g_{NNG} describes the coupling of the nucleon to the gluons arising from contributions violating the Okubo-Zweig-Iizuka rule [36, 37, 38]. The coupling constant g_{NNG} is in part related to the contribution of gluons to the proton spin [39]. As shown by the measurements of the EMC collaboration omission of the spin carried by gluons in polarized protons leads to the so-called "spin crisis" [40]. A small value of $G_A(0) \sim 0.20$ - 0.35 extracted from measurements of the deep inelastic muon-proton scattering [40] and a large mass of the η' meson would be explained by the positive $g_{NNG} \sim 2.45$ value. However, neither $g_{NN\eta'}$ nor g_{NNG} have been measured directly in experiments so far. There is only an estimation of the upper limit of $g_{NN\eta'} < 2.5$ derived from the close-to-threshold total cross section for the $pp \rightarrow pp\eta'$ reaction [16]. From this point of view an investigation of processes where the η' meson is produced directly off a nucleon, such as the $NN \rightarrow NN\eta'$ reaction may be considered as a tool for supplying the information about the above coupling constants and the role of the gluons in dynamical chiral symmetry breaking in low-energy QCD.

As suggested by Bass [9, 10] the η' meson can be created via a *contact interaction* from the glue which is excited in the interaction region of the colliding nucleons. A gluon-induced *contact interaction* contributing to the close-to-threshold $NN \rightarrow NN\eta'$ cross section is derived in the frame of the U(1)-anomaly extended chiral Lagrangian. The physical interpretation of the contact interaction is a very short distance (0.2 fm) interaction where created gluons could couple to the η' directly via its gluonic component or through its flavour-singlet admixture η_1 . This gluonic contribution to the total cross section of the $NN \rightarrow NN\eta'$ reaction is additional to the production mechanism associated with meson exchange [5, 41, 6, 7]. As proposed by Bass in reference [11], the η' meson production via the colour-singlet object does not depend on the total isospin of the colliding nucleons (see figure 2.2) and should lead to the same amplitudes of the production for the $pn \rightarrow pn\eta'$ and $pp \rightarrow pp\eta'$ reactions. This observation motivated the studies of the isospin dependence of the η' meson production in the nucleon-nucleon collisions and in particular a measurement of the $pn \rightarrow pn\eta'$ reaction presented in this thesis.

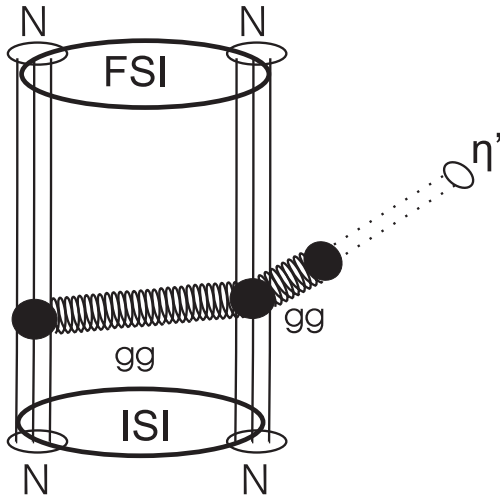


Figure 2.2: Diagram depicting possible quark-gluon dynamics of the $NN \rightarrow NN\eta'$ reaction. Production via a rescattering of a "low energy pseudoscalar pomeron like object" (gluonic current) is isospin independent.

Treating proton and neutron as different states of the nucleon distinguished only by the isospin projection, $+\frac{1}{2}$ for the proton and $-\frac{1}{2}$ for the neutron, we may classify the $NN \rightarrow NNX$ reactions according to the total isospin of the nucleon pair in the initial and final state. A total isospin of two nucleons equals 1 for proton-proton and neutron-neutron pairs, and may acquire the value 1 or 0 for the neutron-proton system. Since the η' meson is isoscalar, there are only two pertinent transitions for the $NN \rightarrow NNX$ reaction, provided that it occurs via an isospin conserving interaction. Thus, it is sufficient to measure two reaction channels for an unambiguous determination of the isospin 0 and 1 cross sections [8].

The isospin dependence has been already established in case of the η meson production, and the total cross sections in both the proton-proton as well as the proton-neutron reactions have been measured. In case of the η meson, the ratio of the total cross sections for the reactions $pn \rightarrow pn\eta$ and $pp \rightarrow pp\eta$ was determined to be $R_\eta \approx 6.5$ [12]. At the lower values of Q , close-to-threshold, the ratio falls down and amounts to $R_\eta \approx 3$ [42, 43], (see figure 2.3). As explained by Wilkin [44, 45], to a large extent this behaviour may plausibly be assigned to the difference in the strength of the proton-proton and proton-neutron final state interaction.

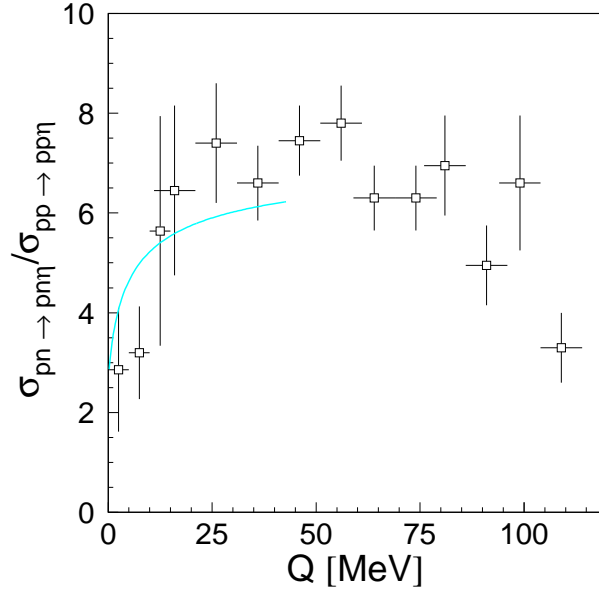


Figure 2.3: The ratio (R_η) of the total cross sections for the $pn \rightarrow pn\eta$ and $pp \rightarrow pp\eta$ reactions. The superimposed line indicates a result of the fit taking into account the final state interaction of nucleons [42].

Since,

$$\begin{aligned}\sigma(pp \rightarrow pp\eta) &= \sigma_{I=1}, \\ \sigma(pn \rightarrow pn\eta) &= \frac{\sigma_{I=0} + \sigma_{I=1}}{2}\end{aligned}$$

we have

$$\sigma_{I=0} = (2R_\eta - 1)\sigma_{I=1},$$

where I denotes the total isospin in the initial and final state of the nucleon pair. The production of the η meson in this reaction with total isospin $I = 0$ exceeds the production with isospin $I = 1$ by a factor of 12. This large difference of the total cross sections suggests the dominance of isovector mesons exchange in the creation of the η meson in collisions of nucleons. A recent experimental study of the analysing power of the $\vec{p}p \rightarrow pp\eta$ reaction [46] indicates that the π meson exchange between the colliding nucleons may be predominant.

Since the amount of different quark flavours in η and η' mesons wave function is similar, in case of the dominant isovector meson exchange – by the analogy to the η meson production – we can expect that the ratio $R_{\eta'}$ should be large. If however the η' meson is produced via its flavour-blind gluonium component from the colour-singlet glue excited in the interaction region the ratio should approach unity after corrections for the initial and final state interactions. The close-to-threshold excitation function for the $pp \rightarrow pp\eta'$ reaction has already been established [13, 14, 15, 16, 17] and the

determination of the total cross section for the η' meson production in the proton-neutron interaction motivated the work presented in this dissertation. Recently Bass and Thomas [47] argued that the strength of the interaction of η and η' mesons with nucleons is sensitive to the singlet-flavour component, and hence to the glue content in these mesons. This makes a connection in our endeavour to investigate the structure, the production dynamics, and the interaction of the η and η' mesons with nucleons [48].

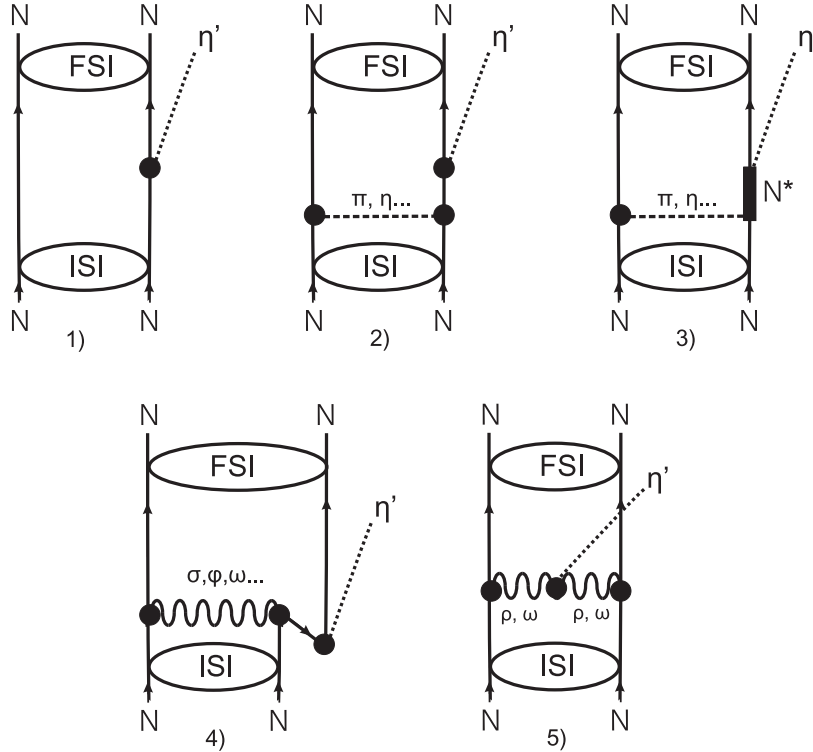


Figure 2.4: Diagrams for the $NN \rightarrow NN\eta'$ reaction close-to-threshold: 1) - η' -bremsstrahlung (nucleonic current), 2) - "rescattering" term (nucleonic current), 3) - excitation of an intermediate resonance (nucleon resonance current), 4) - production through heavy meson exchange, 5) - fusion of the virtual mesons (mesonic current).

Certainly, other production mechanisms which are shown in figure 2.4, such as meson exchange and nucleon resonance currents, must be taken into account before a role of gluons in the $NN\eta'$ vertex is explored. It is expected that the η' meson can be produced through η' -bremsstrahlung (nucleonic current), "rescattering" term (nucleonic currents), excitation of an intermediate resonance (nucleon resonance current), heavy meson exchange or through fusion of the virtual mesons (mesonic current). The two latter mechanisms, which are of short-range, are expected to contribute even more significantly due to the large four-momentum transfer needed between nucleons to create the η' meson. Theoretical studies of the η' meson production mechanism have shown that the existing data could be explained either by mesonic and nucleonic currents or by a dominance of two new resonances $S_{11}(1897)$ and $P_{11}(1986)$ [5]. Moreover an

extended study [41] motivated by the updated data of the $\gamma p \rightarrow \eta' p$ and $pp \rightarrow pp\eta'$ reactions indicated contributions from resonances $S_{11}(1650)$ and $P_{11}(1870)$. However, it is premature to identify these states, as these authors pointed out.

Recently, Cao and Lee [7] have studied the near-threshold η' production mechanism in nucleon-nucleon and π -nucleon collisions under the assumption that the resonance $S_{11}(1535)$ is predominant. In an effective Lagrangian approach which gives a reasonable description to the $pN \rightarrow pN\eta$ and $\pi p \rightarrow p\eta$ reactions, it was found that the t-channel π exchange makes the dominant contribution to the $pN \rightarrow pN\eta'$ process, and a value of 6.5 for the ratio of $\sigma(pn \rightarrow pn\eta')$ to $\sigma(pp \rightarrow pp\eta')$ was predicted.

On the contrary, other authors [6] reproduced the magnitude of the total cross section for the $pp \rightarrow pp\eta'$ reaction including meson currents and nucleon currents with the resonances $S_{11}(1650)$, $P_{11}(1710)$ and $P_{13}(1720)$. A reasonable agreement with the $pp \rightarrow pp\eta'$ data is achieved by the contribution of the meson conversion currents indicating other terms to be less significant. In the frame of this model the $R_{\eta'}$ ratio is predicted to be 1.5.

The above considerations shows that our understanding of the η' meson production mechanism is still unsatisfactory. Therefore it is important to test the discussed mechanisms by confronting them with the experimental results on the isospin dependence of the η' meson production.

3. Spectator model

The absence of pure neutron targets makes measurements of mesons production in proton-neutron interactions very difficult, especially very close-to-threshold where the total cross section changes rapidly with the excess energy [49]. Therefore, to measure the $pn \rightarrow pn\eta'$ reaction we used a deuteron target as an alternative.

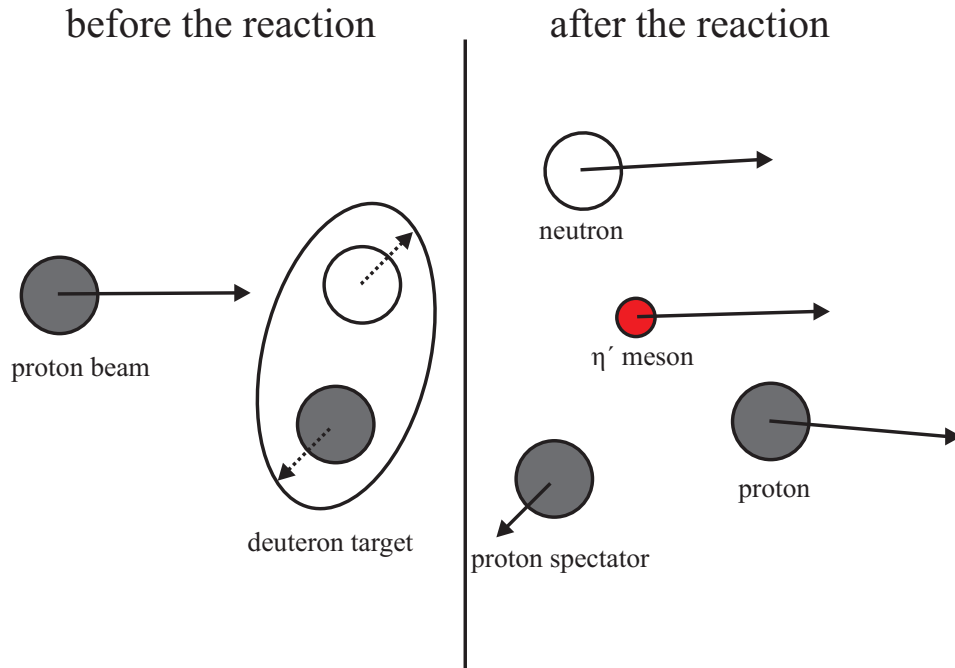


Figure 3.1: Schematic picture of the quasi-free $pn \rightarrow pn\eta'$ reaction. Grey circles represent protons, whereas neutrons are depicted as open circles. The Fermi momentum of the nucleons inside the deuteron is represented by the dotted arrows.

Figure 3.1 shows schematically the quasi-free $pn \rightarrow pn\eta'$ reaction. In the experiment described in this thesis, a cooled proton beam with a momentum of $p_{beam} = 3.35 \text{ GeV}/c$ and a deuteron cluster beam target as a source for neutrons have been used. The applied technique is similar to investigations of the π^0 and η production in proton-neutron collisions carried out by the WASA/PROMICE collaboration at the CELSIUS accelerator in Uppsala [12, 50, 51, 52].

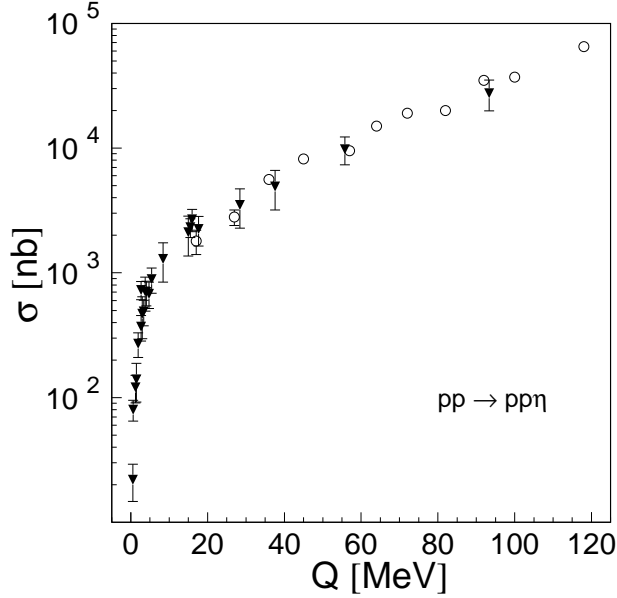


Figure 3.2: Total cross section for the $pp \rightarrow pp\eta$ reaction as a function of the excess energy measured using proton beam colliding with proton target (closed triangles) [53, 54, 55, 56, 57, 17] and proton beam scattered on deuteron target (open circles) [50].

The main difficulty, when using deuterons as a neutron target is the fact that nucleons inside the deuteron are not at rest but are moving with the Fermi momentum. Therefore, in order to achieve the required resolution for the determination of the excess energy in the proton-neutron reaction it is mandatory to determine the neutron momentum inside the deuteron for each event. The momentum of the neutron is derived indirectly based on the measurement of the proton Fermi momentum. For the analysis a *spectator model* is applied. Due to the relatively small binding energy of a deuteron ($E_B = 2.2$ MeV) which is more than three orders of magnitude smaller compared to the kinetic energy of the bombarding proton ($T_{beam} = 2540$ MeV), the neutron is considered as a free particle in the sense that the matrix element for the quasi-free meson production on a bound neutron is equal to the one in free production from an unbound neutron. The second assumption of the spectator model used for the evaluation of the $pn \rightarrow pn\eta'$ reaction is that the proton from the deuteron target does not take part in the reaction and that it is on its mass shell when the beam hits the target. The validity of these assumptions was proven by measurements performed at CELSIUS [50, 51, 52], TRIUMF [58] and COSY-TOF [59]. The comparison of the quasi-free and free production cross sections for the $pp \rightarrow pp\eta$ reaction done by the WASA/PROMICE collaboration has shown that there is no difference between the total cross section for the free and quasi-free process within the statistical errors. The excitation function for the $pp \rightarrow pp\eta$ reaction measured with free and quasi-free proton-proton scattering is presented in figure 3.2. Similarly, investigations of pion production carried out at the

TRIUMF facility have shown that the experimental spectator momentum distribution is consistent with expectations based upon the hypotheses of the spectator model. It was also shown, that the magnitude of the differential cross sections for the quasi-free $pp \rightarrow d\pi^+$ reaction agrees on the few percent level with the free differential cross sections. Recently, the validity of the spectator model was proven also by the COSY-TOF collaboration. The shape of the angular distribution for the quasi-free $np \rightarrow pp\pi^-$ and $pn \rightarrow pn$ reactions as well as the form of the momentum distribution of the spectator have been measured. The experimental data were consistent with calculations based upon the spectator model with an accuracy better than 4% [59].

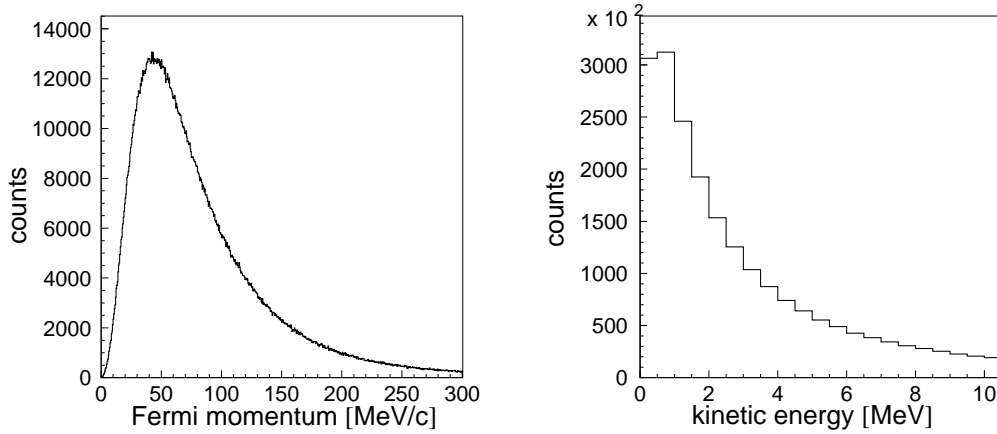


Figure 3.3: Distribution of the momentum (**left**) and the kinetic energy (**right**) of nucleons inside the deuteron generated according to the analytical parametrisation of the deuteron wave function derived from the Paris potential [60, 52].

In case of the quasi-free $pn \rightarrow pn\eta'$ reaction the difference between the on-shell and the off-shell total cross section should be even smaller than in case of the quasi-free η meson production since the total energy of colliding nucleons is much larger for near threshold η' creation than for the creation of the η meson, whereas the main difference between the on-shell and off-shell neutron mass remains the same in both cases.

The momentum and kinetic energy distribution of a spectator proton is shown in figure 3.3. The momentum distribution is peaked at a value of 40 MeV/c but due to the long tail the mean momentum is approximately equal to 100 MeV/c. Since the neutron momentum changes from event to event, both the total energy in the centre-of-mass system (\sqrt{s}) and the excess energy (Q_{cm}) vary also and have to be determined for each event.

Figure 3.4 (left) presents the distribution of the excess energy (Q_{cm}) for the $pp\eta'$ system originating from the $pd \rightarrow pn\eta'p_{spec}$ reaction calculated with a proton beam momentum of $p_{beam} = 3.35$ GeV/c and a neutron target momentum smeared out according to the Fermi distribution. Here p_{spec} denotes the spectator proton. The broad excess energy distribution enables to scan a large range of the excess energy with a single beam

momentum setting but in parallel requires the reconstruction of the centre-of-mass energy for each event. This can be done only if the four-momentum of target neutrons is known, what can be done by measuring the four-momentum vector of the spectator proton, or by measuring all four-momentum vectors of all outgoing nucleons and mesons (proton, neutron and η'). The first possibility requires the detection of the spectator proton in a suitable detection unit as it was realized in the COSY-11 experimental facility. For more details concerning the spectator detector and calibration method see chapters 4. and 5.

As already mentioned, in the frame of the spectator model the proton in the deuteron is assumed to be an untouched particle staying on-shell throughout the reaction. Thus, by measuring the spectator proton momentum (\vec{p}_{spec}) one gets the target neutron momentum (\vec{p}_n) which is equal to $-\vec{p}_{spec}$. The total energy of on-shell proton is equal to:

$$E_{spec} = \sqrt{m_p^2 + p_{spec}^2}, \quad (3.1)$$

and hence the total energy of the off-shell neutron can be calculated as:

$$E_n = m_d - E_{spec}, \quad (3.2)$$

where m_p and m_d denote the free proton and deuteron masses, respectively. Even in case when the proton is at rest ($E_{spec} = m_p$) the neutron is off mass shell due to the binding energy of the deuteron.

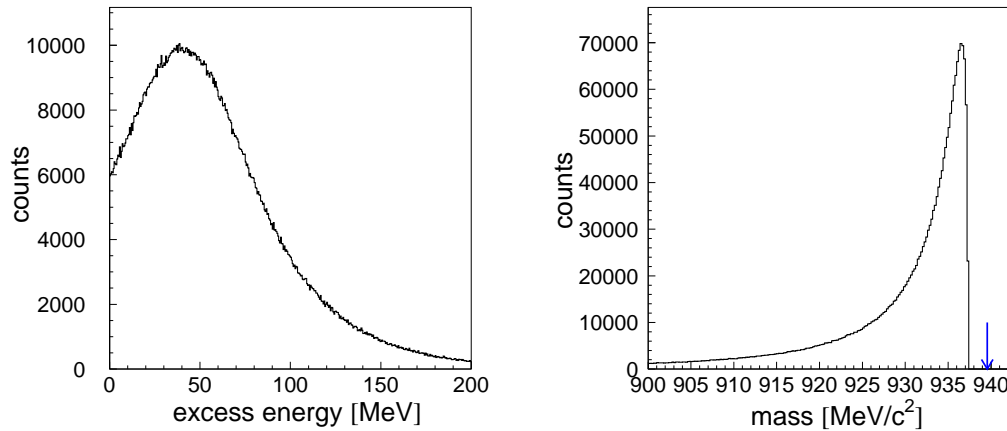


Figure 3.4: **Left:** Distribution of the excess energy (Q_{cm}) for the $pn\eta'$ system originating from the $pd \rightarrow pn\eta' p_{spec}$ reaction calculated with a proton beam momentum of $p_{beam} = 3.35$ GeV/c and a neutron target momentum smeared out according to the Fermi distribution. **Right:** Spectrum of the mass of the interacting neutron. An arrow indicates a mass of the free neutron.

Figure 3.4 (right) shows the distribution of the mass of the interacting neutron as

calculated according to the relation:

$$m_n^{real} = \sqrt{E_n^2 - p_{spec}^2}, \quad (3.3)$$

where E_n is the total energy of the off-shell neutron. As it is seen, the maximum of this distribution differs only by 2.2 MeV from the free neutron mass ($m_n = 939.565 \text{ MeV}/c^2$).

The quasi-free meson production is disturbed by some nuclear effects, namely a shadow effect and a reabsorption of the produced meson by the spectator proton but they are rather of minor importance. In the first case the reduction of the beam flux originating in neutron shielding by a spectator proton decreases the total cross section by about 4.5% in case of η meson production [61]. The same effect is expected for the η' meson production. The absorption of the η meson reduces the total cross section by 2% – 4% [61] depending on the energy of the η meson which was produced. In case of a quasi-free η' meson production this effect is much smaller since the proton- η' interaction is much weaker than the proton- η one [8].

4. Experimental tools

The experiment described in this thesis has been performed using the COSY-11 facility [62, 63, 64] an internal magnetic spectrometer installed at the cooler synchrotron and storage ring COSY [65] in Jülich, Germany.

4.1 Cooler Synchrotron COSY

The Cooler Synchrotron COSY stores and accelerates unpolarized as well as polarized proton and deuteron beams in the momentum range between 0.6 GeV/c and 3.7 GeV/c.

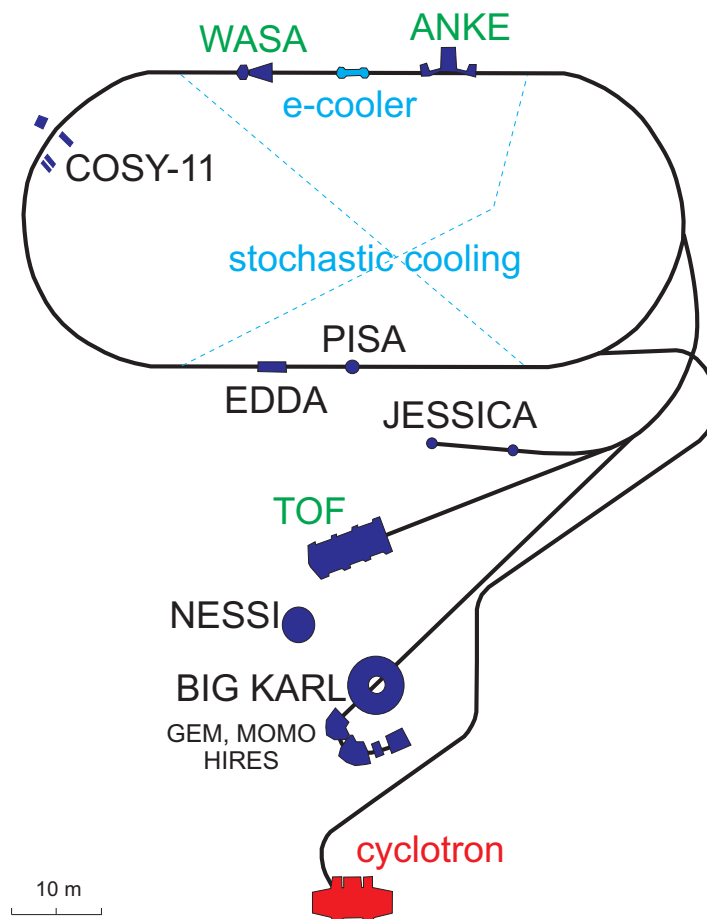


Figure 4.1: Scheme of the COoler Synchrotron COSY with indicated internal experiments: (COSY-11 [62], WASA [66, 67], ANKE [68], PISA [69], EDDA [70]) as well as external experiments (JESSICA [71], TOF [72], NESSI [73], GEM [74], BIG KARL [74], MOMO [75], HIRES [76]).

Cooling with electrons in the lower momentum range and stochastic cooling in the upper momentum regime is used to decrease the spread of the beam momentum and its emittance. Proton and deuteron beams are supplied to experiments with the circulating beam – ”internal experiments” or for experiments with the extracted beam – ”external experiments”. In case of internal experiments, at the highest beam momentum a few times 10^{10} accelerated particles pass through the target $\sim 10^6$ times per second. The COSY synchrotron – which is schematically depicted in figure 4.1 – has a 180 m circumference including two half-circle sections connected by two 40 m straight sections. The experiment presented in this thesis is the first ever attempt to measure the cross section of the $pn \rightarrow pn\eta'$ reaction. It has been carried out at the COSY-11 detection setup using a deuteron cluster target and a stochastically cooled proton beam with a momentum of 3.35 GeV/c. The experiment was performed in August 2004 and the data have been collected for 24 days. It was based on the measurement of four-momenta of the outgoing nucleons, whereas an unregistered short lived meson η' was identified via the missing mass technique.

4.2 COSY–11 facility

The COSY–11 detector system is schematically depicted in figure 4.2. The detectors used for the registration of the spectator proton and the neutron (silicon pad detector and neutral particle detector, respectively) will be described more detailed in the following sections. The details of the other detector components used in this experiment and the method of measurement can be found in references [62, 64, 77, 78]. Therefore, here the used experimental technique will be presented only briefly.

The COSY–11 cluster target, shown in figure 4.3 is installed in front of one of the COSY dipole magnets. It can provide streams of clusters of hydrogen (H_2) as well as of deuteron (D_2). The charged products of the measured reactions are bent in the magnetic field of the dipole magnet and leave the vacuum chamber through a thin exit foil, whereas the beam — due to the much larger momentum — remains on its orbit inside the ring. The charged ejectiles are detected in the drift chambers (D1, D2) [62, 64] and the scintillator hodoscopes (S1, S3) [62, 77, 78]. Neutrons and gamma quanta are registered in the neutral particle detector [79]. The veto detector is used in order to separate neutrons and gamma quanta from charged particles. An array of silicon pad detectors (*spectator detector*) [80] is used for the registration of the spectator protons.

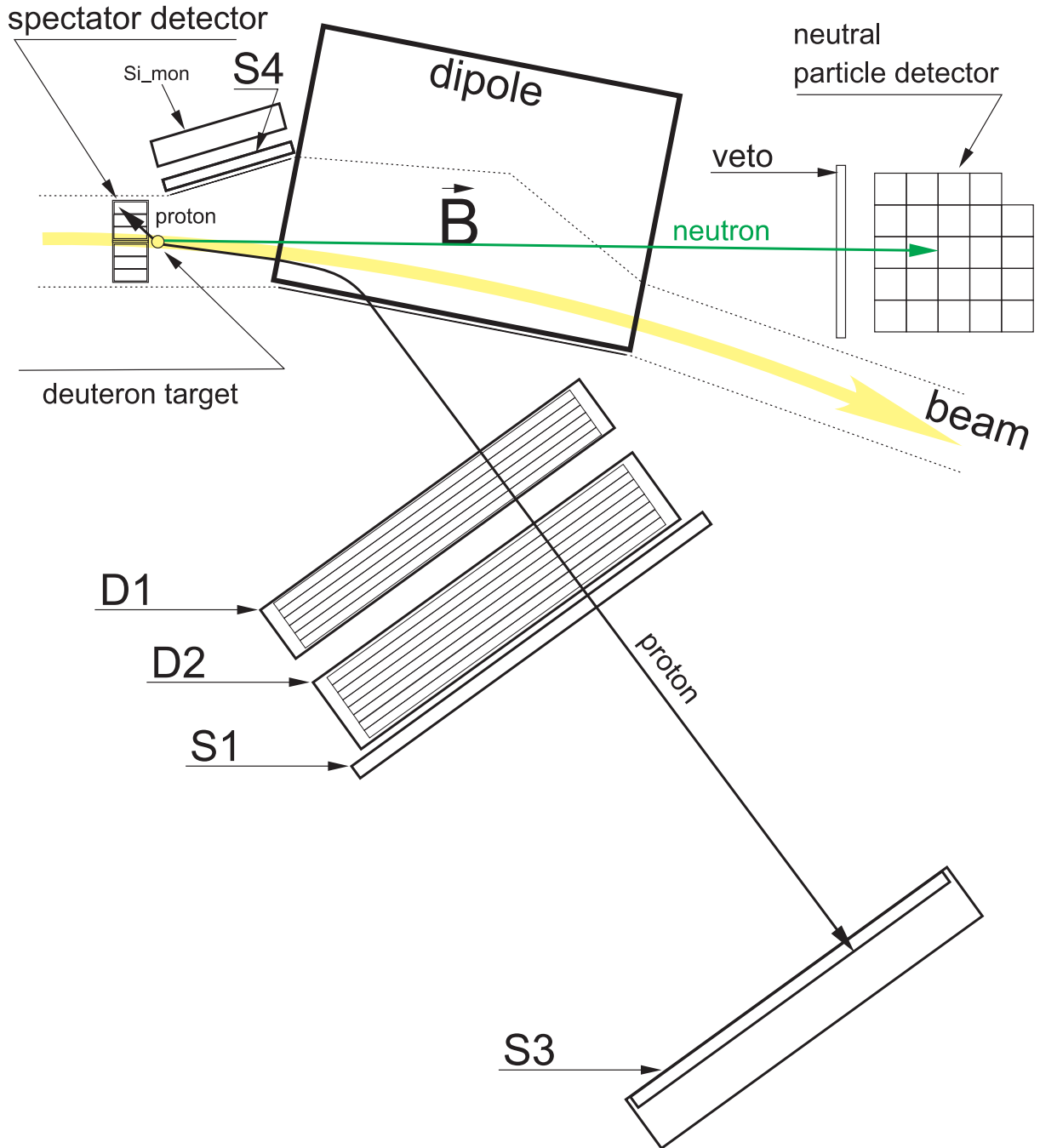


Figure 4.2: Scheme of the COSY-11 detector system with superimposed tracks from the $pd \rightarrow p_{spec}(pn\eta')$ reaction. Protons are registered in two drift chambers D1, D2 and in the scintillator hodoscopes S1 and S3. The S1 detector is built out of 16 vertically arranged modules, whereas the S3 hodoscope is a non-segmented scintillator wall viewed by a matrix of 217 photomultipliers. An array of silicon pad detectors (*spectator detector*) is used for the registration of the spectator protons. Neutrons are registered in the neutral particle detector consisting of 24 independent detection units. In order to distinguish neutrons from charged particles a veto detector is used. Elastically scattered protons are measured in the scintillator detector S4 and position sensitive silicon detector Si_{mon} . Detectors' size and their relative distances are not to scale.

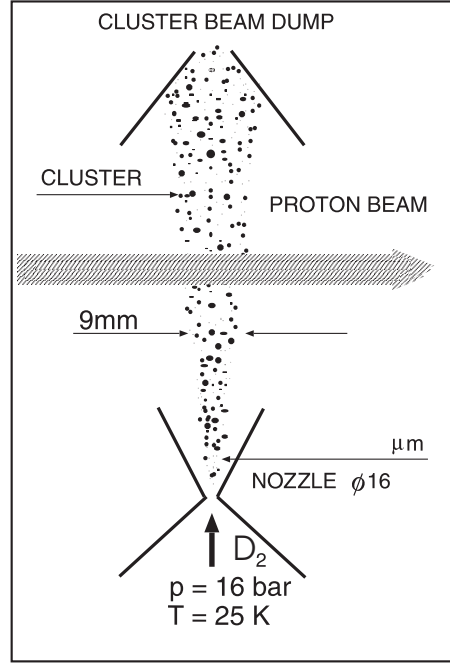


Figure 4.3: Schematic view of the cluster target. The figure is adapted from reference [77].

Protons scattered elastically under large angles are measured in the scintillator detector S4 and in another position sensitive silicon pad detector (Si_{mon}) positioned closely behind the S4 counter.

4.3 Measurement method – general remarks

The main goal of this experiment is the determination of the total cross section for the $pn \rightarrow pn\eta'$ reaction in the excess energy range between 0 and 24 MeV. In order to calculate the total cross section, given in general by the formula:

$$\sigma(Q_{cm}) = \frac{N(Q_{cm})}{L \times E_{eff}(Q_{cm})}, \quad (4.1)$$

one needs to determine: *i*) the efficiency E_{eff} of the COSY-11 detection system, *ii*) the luminosity L integrated over the time of the experiment, *iii*) the excess energy Q_{cm} and *iv*) the number of η' meson events N registered for a given excess energy. In the following the experimental conditions, technique of measurement and method of the E_{eff} , L , Q_{cm} , N determination will be presented.

Events corresponding to the production of at least one charged particle in coincidence with a neutron (or gamma quantum) were stored on the tape for later analysis. Conditions of the main trigger can be written symbolically as:

$$T_{\eta'} = \{N_{up}^{\mu \geq 1} \wedge N_{dw}^{\mu \geq 1}\} \wedge S1_{2..6}^{\mu \geq 1} \wedge S3,$$

which requires that at least a coincidence of one hit (multiplicity $\mu \geq 1$) in the neutral particle detector (in upper and lower photomultiplier), in the S1 detector, and in the scintillator wall S3 was demanded. The S1 region was restricted to 5 modules (from 2nd to 6th) in which the proton signal from the $pn \rightarrow pn\eta'$ reaction was expected.

During the experiment an additional trigger referred to as T_{elas} was set up for the registration of the quasi-free p-p elastic scattering. Events which gave a signal in the S1 detector in coincidence with the S4 detector (see figure 4.2) were accepted as a quasi-free proton-proton scattering or elastic proton-deuteron scattering.

For each charged particle, which gave signals in the drift chambers, the momentum vector at the reaction point can be determined. For the analysis of the $pn \rightarrow pn\eta'$ reaction, first the trajectories of the outgoing protons are reconstructed [81] based on signals in the drift chambers D1 and D2 – and then knowing the magnetic field of the dipole magnet – its momentum vector is determined. Independently, the velocity of the particle is derived based on the time-of-flight measured between the S1 and the S3 detectors. Knowing the velocity and the momentum of the particle, its mass can be calculated, and hence the particle can be identified. After the particle identification the time of the reaction at the target is obtained from the known trajectory, velocity, and the time measured by the S1 detector.

The neutral particle detector delivers the information about the time at which the registered neutron or gamma quantum induced a hadronic or electromagnetic reaction in the detector volume, respectively. The time of the reaction combined with this information allows to calculate the time-of-flight (TOF^N) of the neutron (or gamma) between the target and the neutral particle detector, and — in case of neutrons — to determine the absolute value of the momentum (p), expressed as:

$$p = m_n \cdot \frac{l}{TOF^N} \cdot \frac{1}{\sqrt{1 - \left(\frac{l}{TOF^N}\right)^2/c^2}}, \quad (4.2)$$

where m_n denotes the mass of the neutron, and l stands for the distance between the target and the neutral particle detector. The direction of the neutron momentum vector is deduced from the angle defined by the centre of the hit module inside the neutral particle detector.

Similarly, to determine the direction of the momentum vector of the spectator proton, the angle defined by the centre of the hit segment inside the spectator detector is used. In order to calculate the four-momentum of the spectator proton its kinetic energy (T_{spec}) is directly measured as the energy loss in the silicon detector. Knowing the proton kinetic energy (T_{spec}) one can calculate its momentum using the relationship:

$$p = \sqrt{(T_{spec} + m_p)^2 - m_p^2}, \quad (4.3)$$

where m_p denotes the proton mass.

To evaluate the luminosity, the quasi-elastic proton-proton scattering is measured during the data taking of the $pn \rightarrow pn\eta'$ reaction, with one proton detected in the drift chambers and the scintillator hodoscopes and the other proton registered in the silicon

detector $S_{i_{mon}}$. The elastically scattered protons can be well separated from the multi-particle reactions, due to the two body kinematics.

Based on Monte Carlo studies, the beam momentum value, the position of the spectator detector and the configuration of the neutral particle detector have been optimized before the experiment in order to maximize the detection efficiency, the resolution of the excess energy determination and in order to achieve a relatively high missing mass resolution [82].

In the next two chapters the method of the detector calibration and evaluation of the data, namely determination of the excess energy Q_{cm} , number of η' mesons created in proton–neutron collisions, the luminosity L and the detection efficiency will be presented.

5. Calibration of the detectors

5.1 Time-space calibration of the drift chambers

In this section we give an account on the time-space calibration of the drift chambers. The drift chamber D1 (see figure 4.2) contains six detection planes, two planes have vertical wires and four have inclined wires. The second drift chamber (D2) contains two more planes with vertical wires (altogether eight). The wires in consecutive pairs of planes are shifted by half of the cell width in order to resolve the left-right position ambiguity with respect to the sense wire. Both chambers were operating with 50%–50% argon–ethane gas mixture at atmospheric pressure.

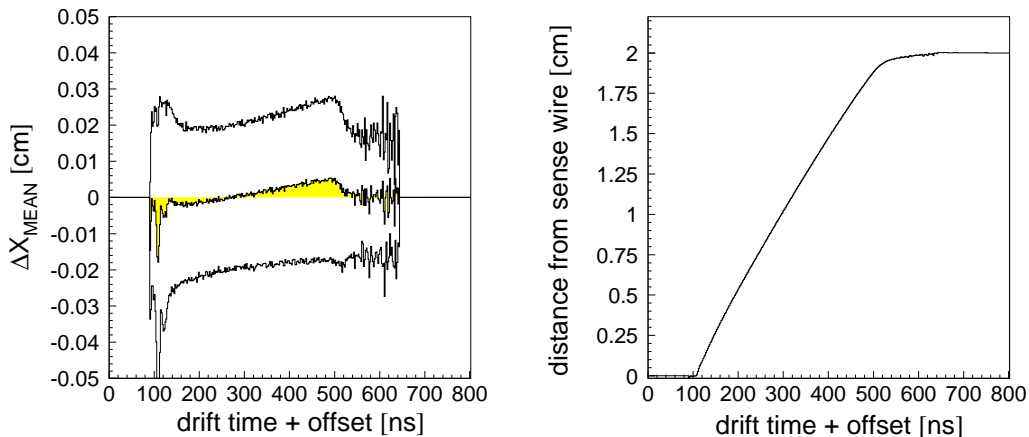


Figure 5.1: **Left:** Example of the spectrum used for the drift chamber calibration. The shaded area presents mean values of ΔX as a function of the drift time. Upper and lower histograms indicate a band of one standard deviation of the ΔX distribution. The meaning of ΔX is explained in the text. **Right:** Distance from the sense wire as a function of the drift time for an arbitrarily chosen plane of the D1 chamber.

When a charged particle passes through the drift cell it invokes an ionization of the gas mixture. The positively charged ions drift to the cathode wires with negative potential, whereas the free electrons drift towards the sense wire with positive potential. The drift time of electrons is measured and hence the distance between the particles trajectory and the sense wire can be determined. A relation between the drift time and the distance from a sense wire is established from experimental data. Due to variations of the drift velocity caused by changes of the pressure, temperature and humidity of the air inside the COSY tunnel, the drift chamber calibration has to be performed for time intervals not longer than few hours. The calibration is derived in an iterative way. First,

having an approximate time-space function $x(t)$ for a given sample of measured events¹, a distance of particle trajectory from a sense wire is calculated, and a straight line is fitted to the obtained points. Next, the deviation ΔX between the fitted and measured distances of the particle's trajectory to the wire is calculated. An example of a mean value of ΔX as a function of the drift time is shown in figure 5.1 (left). The shaded area represents the mean values of ΔX . Upper and lower histograms indicate a band of one standard deviation of the ΔX distribution. Afterwards the relation between the drift time and distance from the wire is corrected by the determined mean value of ΔX . The procedure is repeated until corrections become negligible compared with expected position resolution of the chambers.

Figure 5.1 (right) shows the time-space calibration of an arbitrarily chosen plane of the D1 chamber. The nearly linear dependence is seen for the drift time range from 100 ns up to 500 ns.

5.2 Time calibration of the S1 and S3 hodoscopes

In this section a method of the time-of-flight calibration is presented.

The time-of-flight measurement on the known distance between the S1 and the S3 hodoscopes enables to calculate the velocity of the particle which crosses both detectors. In order to calculate the time-of-flight, relative time offsets between each detection unit of the S1 and S3 detectors have to be established.

The S1 detector (see figure 4.2) is built out of sixteen scintillation modules with dimensions $45 \text{ cm} \times 10 \text{ cm} \times 0.4 \text{ cm}$. The modules are arranged vertically with a 1 mm overlap and are read out at both ends by pairs of photomultipliers. The start time for the time-of-flight measurement is calculated as the mean value of times measured by the upper and lower photomultiplier of the S1 detector module. The measured TDC values for a single S1 module may be expressed as:

$$\begin{aligned} TDC_{S1}^{up} &= t_{S1} + \frac{y}{\beta_L} + t_{up}^{walk} + offset_{up} - T_{trigger}, \\ TDC_{S1}^{dw} &= t_{S1} + \frac{L-y}{\beta_L} + t_{dw}^{walk} + offset_{dw} - T_{trigger}. \end{aligned} \quad (5.1)$$

The t_{S1} is the real time when a particle crosses the detector, y denotes the distance between the upper edge of the active part of the detector and the hit position, t_{up}^{walk} and t_{dw}^{walk} stand for the time walk effect, and $offset_{up}$, $offset_{dw}$ comprise all delays due to the utilized electronic circuits. The common start signal for all TDC modules is denoted by the $T_{trigger}$ and it is the same for S1 and for S3 detector. Thus the mean value of the

¹In case of this experiment the first approximation was taken from the previous COSY-11 runs. It is worth noting that in general an approximate drift time to drift distance relation can be determined by integration of the drift time spectra as provided by the uniform irradiation method [83].

time measured by the S1 module is given by:

$$t_{S1} = \frac{TDC_{S1}^{up} + TDC_{S1}^{dw}}{2} - offset_{S1} - t_{S1}^{walk} + T_{trigger}, \quad (5.2)$$

where $offset_{S1}$ comprises all constant terms from eq. 5.1.

The S3 hodoscope is built out of a non-segmented scintillator wall with the dimensions $220 \text{ cm} \times 100 \text{ cm} \times 5 \text{ cm}$ viewed by a matrix of 217 photomultipliers. The stop signal for the time-of-flight measurement is calculated as the average of times obtained from all the photomultipliers that produced a signal. The TDC value for a single photomultiplier is expressed similarly as in the case of the S1 detector:

$$TDC_{S3} = t_{S3} + t_{S3}^{pos} + t_{S3}^{walk} + offset_{S3} - T_{trigger}, \quad (5.3)$$

where t_{S3} denotes the real time when a particle crosses the detector and the t_{S3}^{pos} is the time needed by the light signal to pass from the scintillation origin down to the photomultiplier photocathodes. Applying equations 5.1 and 5.3 one can calculate the time-of-flight between the S1 and S3 hodoscopes as:

$$TOF^{S3-S1} = t_{S3} - t_{S1},$$

$$TOF^{S3-S1} = TDC_{S3} - t_{S3}^{pos} - t_{S3}^{walk} - offset_{S3} - \frac{TDC_{S1}^{up} + TDC_{S1}^{dw}}{2} + t_{S1}^{walk} + offset_{S1}. \quad (5.4)$$

Since in both equations (5.1, 5.3) the $T_{trigger}$ time is the same, the TOF^{S3-S1} is independent of the triggering time. The t_{S3}^{pos} as well as t_{S1}^{walk} and t_{S3}^{walk} may be calculated based on the known calibration parameters and amplitude of the signals [77]. Thus the only unknown quantities in equation 5.4 for TOF^{S3-S1} are the time offsets for the individual photomultipliers of S3 detector ($offset_{S3}$) and time offsets for a single module of S1 detector ($offset_{S1}$).

In order to establish these effects we have selected events with only one track reconstructed in the drift chambers, with signals in only one S1 module and signals in the S3 hodoscope for those photomultipliers which are at the position expected from the extrapolation of the particle trajectory determined in the drift chambers.

In the first approximation the relative offsets of the S1 modules were established comparing the time between neighbouring modules for signals from particles which crossed the detector through the overlapping regions. Assuming, that the time offsets for the S1 detector are approximately correct, we have established the time offsets for each photomultiplier of S3 detector, by comparing the time-of-flight values calculated from the time signals in the S1 and S3 detectors (see eq. 5.4) with the time-of-flight determined from the reconstructed momenta of the particles in the magnetic field. Having the time offsets for the S3 hodoscope adjusted, we have again re-calculated the offsets for the S1 detector in the same way as it was done for the S3 detector. This procedure was repeated a few times until the corrections of the offsets became negligible.

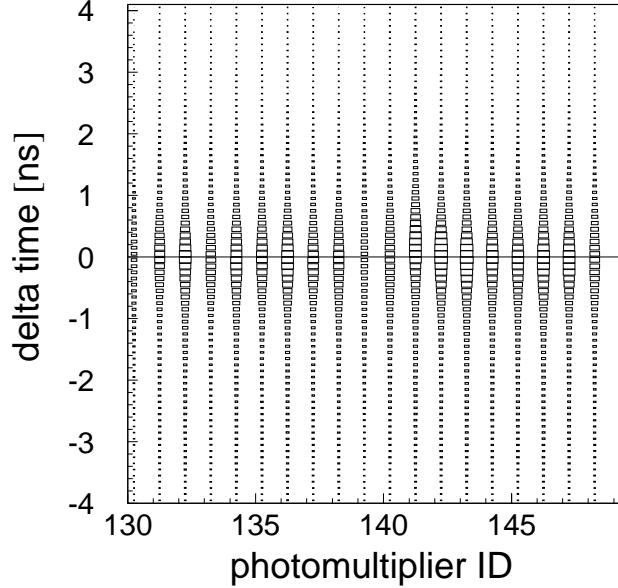


Figure 5.2: The difference between the time-of-flight (TOF_{S3-S1}) determined from signals registered in the S1 and S3 scintillators and the time-of-flight calculated from the reconstructed momenta of particles versus the photomultiplier ID of S3. The figure shows result after the S3 hodoscope calibration. Photomultipliers which are positioned at the lower and upper edge of the scintillation wall have registered essentially less events (ID = 130 and 139).

Figure 5.2 presents the distribution of difference between the time-of-flight (TOF_{S3-S1}) on the S1-S3 distance determined from signals registered in S1 and S3 scintillators and the time-of-flight calculated from the reconstructed momenta of particles for photomultipliers no. 130–149 as obtained after the third iteration.

5.3 The neutral particle detector

The installation of the neutral particle detector at the COSY-11 facility enabled to study reactions with neutrons in the exit channel. It allows, for example to investigate quasi-free meson production in proton-neutron interactions or charged hyperon production like Σ^+ via the $pp \rightarrow nK^+\Sigma^+$ reaction [84, 85]. This detector [86] delivers the time at which neutron or gamma quantum induces a hadronic or electromagnetic reaction inside the detector volume, respectively. This information combined with the time of the reaction at target place — deduced using other detectors — enables to calculate the time-of-flight between the target and the neutral particle detector and to determine the absolute momentum of the registered neutrons.

In this section a method of time calibration will be demonstrated and results achieved by its application will be presented and discussed.

Information about the deposited energy is not used in the data analysis because the smearing of the neutron energy determined by this manner is by more than an order of magnitude larger than established from the time-of-flight method. The experimental precision of the missing mass determination of the $pn \rightarrow pn\eta'$ reaction [87, 88] strongly relies on the accuracy of the reconstruction of the momentum of neutrons, therefore the time calibration of the neutral particle detector has to be done with high precision.

Previously, the neutron detector consisted of 12 detection units [89], with light guides and photomultipliers mounted on one side of the module. In order to improve the time resolution of the detector additional light guides and photomultipliers were installed, such that the light signals from the scintillation layers are read out at both sides of the module. The neutral particle detector used for the experiment described in this thesis consists of 24 modules, as shown in figure 5.3. Each module is built out of eleven plates of scintillator material with dimensions $240 \text{ mm} \times 90 \text{ mm} \times 4 \text{ mm}$ interlaced with eleven plates of lead with the same dimensions. The scintillators are connected at both ends of a module to light guides — made of plexiglass — whose shape changes from rectangular to cylindrical, in order to accumulate the produced light on the circular photocathode of a photomultiplier. There the light pulse is converted into an electrical signal, which is provided to the ADC and to the TDC converters.

The neutron detector is positioned at a distance of 7.36 m from the target in the configuration schematically depicted in figure 5.3. The detector covers the laboratory angular range of $\pm 1.84^\circ$ in x and $\pm 1.1^\circ$ in y direction.

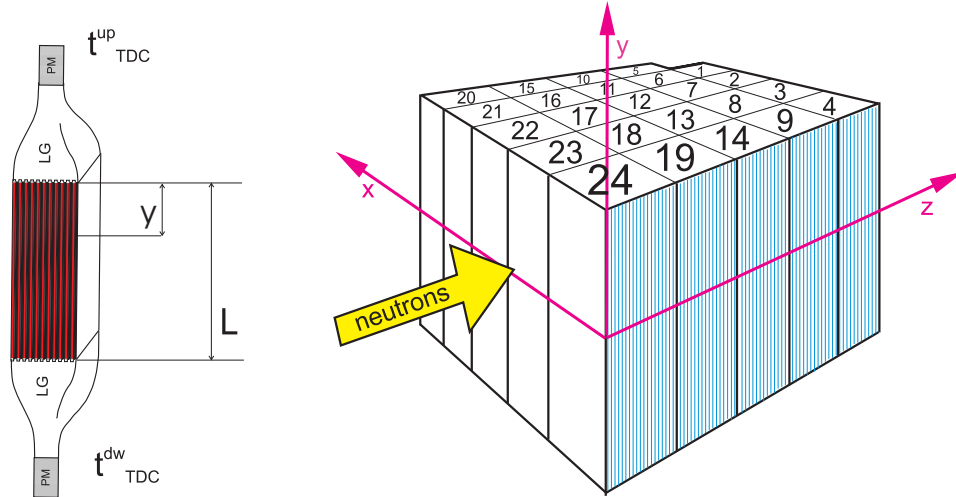


Figure 5.3: **Left:** Scheme of the single detection unit of the COSY-11 neutral particle detector. LG and PM denotes light guide and photomultiplier, respectively. The figure shows also the definition of variables y and L used in the text. **Right:** Configuration of the detection units of the neutral particle detector.

This configuration and the distance to the target has been chosen to optimize the efficiency for the reconstruction of the $pn \rightarrow pn\eta'$ reaction [82]. The choice was based on results from Monte Carlo studies of the acceptance and efficiency as a function of the

distance and configuration [82]. The choice for the thickness of the scintillator plates was also based on the simulation studies [90].

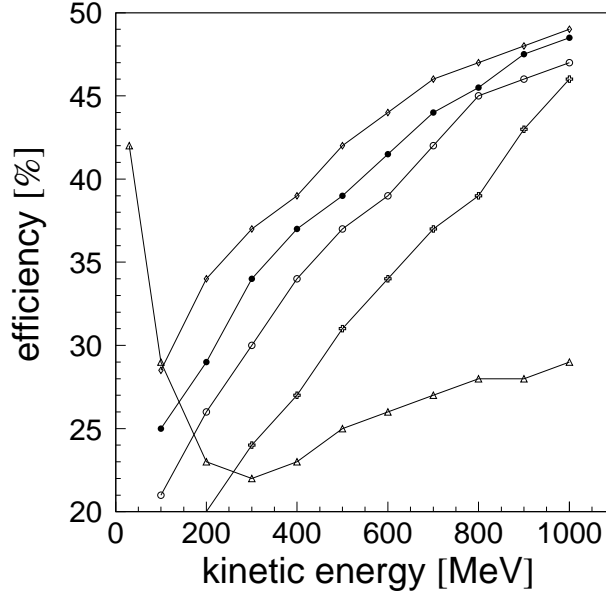


Figure 5.4: Efficiency of the 20 cm thick neutron detector as a function of neutron kinetic energy simulated for various layer thicknesses of the scintillator and iron plates. The solid line with triangles is for pure scintillator material. Diamonds denote a layer thickness of 0.5 mm, closed circles of 2 mm, open circles of 5 mm, and crosses of 25 mm. The figure has been adapted from ref. [90]. Note that for better visualisation the vertical axis starts at 20%.

As can be deduced from figure 5.4 the maximum efficiency, for a given total thickness, for the registration of neutrons — in the kinetic energy range of interest for the $pd \rightarrow pn\eta' p_{sp}$ reaction (~ 300 MeV – ~ 700 MeV) — would be achieved for a homogeneous mixture of lead and scintillator. However, in order to optimize the efficiency and the cost of the detector the plate thickness has been chosen to be 4 mm. This results in an efficiency which is only of few per cent smaller than the maximum possible. The functioning of the detector was already tested in previous experiments [42, 79, 85].

5.3.1 Time signals from a single detection unit

A schematic view of a single detection module of the COSY-11 neutral particle detector is shown in figure 5.3 (left). The time (T^{exp}) from a single module is calculated as an average time measured by the upper and lower photomultiplier. Namely:

$$T^{exp} = \frac{TDC^{up} + TDC^{dw}}{2}, \quad (5.5)$$

where $TDC^{up,dw}$ denotes the difference between the time of signals arrival from the photomultiplier and from the trigger unit to the Time-to-Digital-Converter (TDC). This can be expressed as²:

$$TDC^{up} = t^{real} + \text{offset}^{up} + \frac{y}{c_L} - T_{trigger}, \quad (5.6)$$

$$TDC^{dw} = t^{real} + \text{offset}^{dw} + \frac{L-y}{c_L} - T_{trigger}, \quad (5.7)$$

where L stands for the length of a single module, y denotes the distance between the upper edge of the active part of the detector and the point at which a neutron induced the hadronic reaction, t^{real} is the time at which the scintillator light was produced, $T_{trigger}$ represents the time at which the trigger signal arrives at the TDC converter, and c_L denotes the velocity of the light signal propagation inside the scintillator plates. The parameters offset^{up} and offset^{dw} denote the time of propagation of signals from the upper and lower edge of the scintillator to the TDC unit.

Applying equations 5.5, 5.6 and 5.7 one can calculate a relation between T^{exp} and t^{real} :

$$T^{exp} = t^{real} + \frac{\text{offset}^{up} + \text{offset}^{dw} + \frac{L}{c_L}}{2} - T_{trigger} = t^{real} + \text{offset} - T_{trigger}, \quad (5.8)$$

where the value of "offset" comprises all delays due to the utilized electronic circuits, and it needs to be established separately for each segment. It is worth noting, that due to the readout at both ends of the detector the T^{exp} is independent of the hit position along the module, as it can be deduced from equation 5.8.

5.3.2 Relative timing between modules

Instead of determining the values of "offsets" from equation 5.8 for each detection unit separately, the relative timing between modules will be first established and then the general time offset connecting the timing of all segments with the S1 detector will be found.

In order to establish relative time offsets for all single detection units, distributions of time differences between neighbouring modules were derived from experimental data and compared with simulated distributions. A time difference measured between two modules can be expressed as:

$$\Delta_{ij} = T_i^{exp} - T_j^{exp} = t_i^{real} - t_j^{real} + (\text{offset}_i - \text{offset}_j), \quad (5.9)$$

where T_i^{exp} and T_j^{exp} stand for the time registered by the i^{th} and j^{th} module, respectively. Examples of Δ_{ij} spectra determined before the calibration are presented in figure 5.5.

²Here we omit the time walk effect which will be discussed later in section 5.3.3

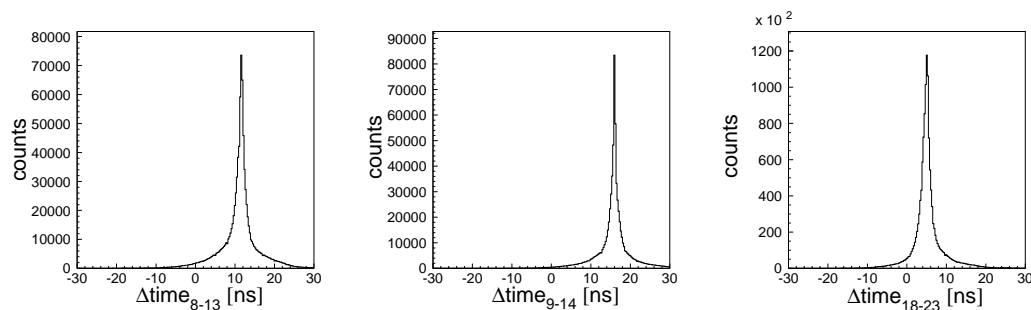


Figure 5.5: Distributions of the time difference between the 8th and the 13th, the 9th and the 14th, and the 18th and the 23th module of the neutron detector, as determined before the calibration assuming that offsets are equal to zero.

One can note that the peaks are shifted from the zero value and additionally the distributions contain tails. The tails reflect the velocity distribution of the secondary particles. In order to determine reference spectra corresponding time differences between the modules were simulated using the GEANT-3 code. The result of the simulation is shown in figure 5.6. To produce these spectra the quasi-free $pn \rightarrow pn\eta'$ reaction has been simulated.

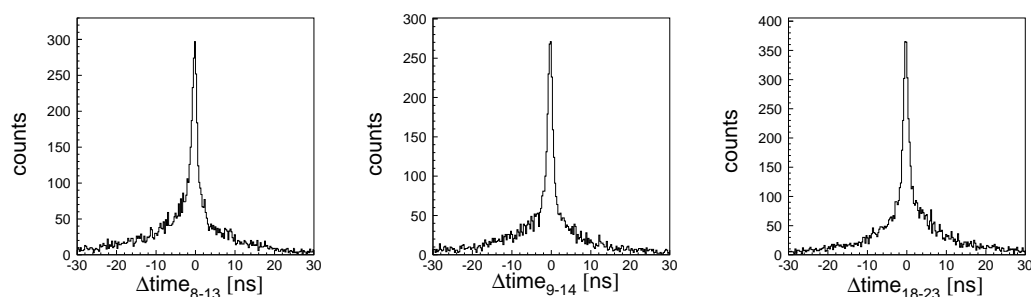


Figure 5.6: Simulated distributions of the time difference between the 8th and the 13th, the 9th and the 14th, and the 18th and the 13th module of the neutron detector.

The values of the relative time offsets were determined using a dedicated program written in Fortran 90 [91, 92]. It adjusts values of offsets such that the time difference obtained from the experimental data and from simulations equals to each other for each pair of detection units. Furthermore, from the width of the spectra one can obtain the information about the time resolution of a single module, which was extracted to be 0.4 ns [91].

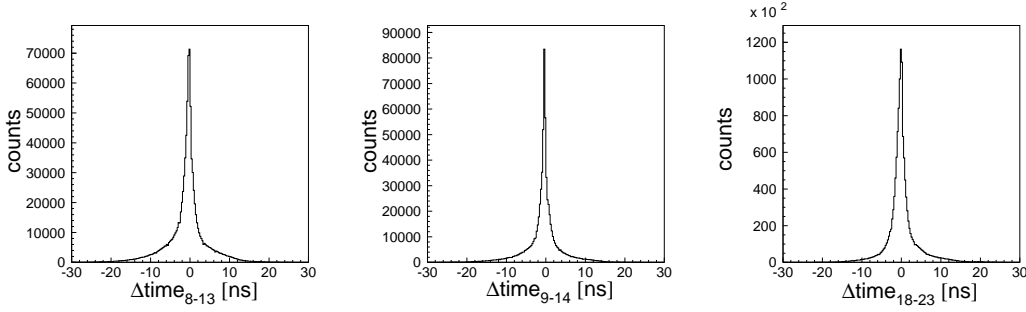


Figure 5.7: Distributions of the time difference between the 8th and the 13th, the 9th and the 14th, and the 18th and the 23th module of the neutron detector, as obtained after the calibration.

Figure 5.7 presents experimental distributions of time differences between neighbouring modules as determined after the calibration. Examining figures 5.7 and 5.6 it is evident that now the peaks are positioned as expected from simulation.

5.3.3 General time offset and the time walk correction

The momenta of neutrons are determined on the basis of the time between the reaction and the hit time in the neutral particle detector. The time of the reaction can be deduced from the time when the exit proton from the $pn \rightarrow pn\eta'$ reaction crosses the S1 detector (see fig. 4.2) because the trajectory and the velocity of this proton can be reconstructed. Therefore, to perform the calculation of the time-of-flight between the target and the neutral particle detector, a general time offset of this detector with respect to the S1 counter has to be established. This can be done by measuring the gamma quanta for which the velocity is constant.

The time-of-flight between the target and the neutral particle detector (TOF^N) is calculated as the difference between the time of the module in the neutral particle detector which fired as the first one (t_N^{real}) and the time of the reaction in the target (t_r^{real}):

$$TOF^N = t_N^{real} - t_r^{real} \quad (5.10)$$

The time of the reaction is obtained from backtracking the protons through the known magnetic field and the time measured by the S1 detector (t_{S1}). Thus t_r^{real} can be expressed as:

$$t_r^{real} = t_{S1} - TOF^{S1} = T_{S1}^{exp} - offset^{S1} + T_{trigger} - TOF^{S1}, \quad (5.11)$$

where TOF^{S1} denotes the time-of-flight between the target and the S1 counter, $offset^{S1}$ denotes all delays of signals from the S1 detector, and analogically as for equation 5.8 the t_{S1} and T_{S1}^{exp} denote the time at which the scintillator light in the S1 detector was produced and the averaged time registered by the TDC unit (see eq. 5.5), respectively. Since the time in the neutron detector reads:

$$t_N^{real} = T_N^{exp} - offset^N + T_{trigger} \quad (5.12)$$

we have:

$$TOF^N = T_N^{exp} + TOF^{S1} - T_{S1}^{exp} - offset^N + offset^{S1} = T_N^{exp} + TOF^{S1} - T_{S1}^{exp} + offset^G \quad (5.13)$$

By $offset^G$ the general time offset of the neutron detector with respect to S1 is denoted. In order to determine the value of $offset^G$ the $pd \rightarrow A^+B^+\gamma X$ reaction is used, where γ is measured by the neutral particle detector and for which the TOF^N between the target and the neutral particle detector is known. A^+ and B^+ represent any two positively charged particles ($\pi^+\pi^+$, $p\pi^+$, pd , $d\pi^+$). Events corresponding to the $pd \rightarrow A^+B^+\gamma X$ reaction have been identified by measuring the outgoing charged as well as neutral ejectiles. Positively charged particles (pions, protons and deuterons) were detected by means of the drift chambers (D1, D2) and scintillator hodoscopes (S1, S3). Gamma quanta originated predominately from the π^0 meson decay are registered in the neutral particle detector. Knowing the time-of-flight for gamma quanta T_γ on the distance between the target and the neutral particle detector the general time offset was determined by comparing the measured time with the nominal value of T_γ . The measured time-of-flight spectrum is shown in figure 5.8. T_γ should be equal to 24.5 ns. As can be inspected from the figure 5.8, the time depends on the amplitude. This phenomenon is occurring for measurements using a leading-edge discriminator and is referred to as the time-walk effect [93]. In the case of a constant threshold value, two signals of different pulse heights but exactly coincident in time may trigger the discriminator at different times. An offline correction can be applied to minimize this effect assuming a linear dependence between the time walk and the inverse of the square root of the signal charge [94]. The function used for offline time-walk correction was

$$t_c = t_m - \alpha + \beta \left(\frac{1}{\sqrt{ADC^{up}}} + \frac{1}{\sqrt{ADC^{dw}}} \right), \quad (5.14)$$

where t_c and t_m are corrected and measured times, and α and β are coefficients determined from the data, and ADC^{up} and ADC^{dw} denote the charge of the signal measured at the upper and the lower end of the detection module.

Figure 5.8 shows the dependence of the time-of-flight for neutral particles as a function of values of ADC signals in the neutral particle detector. The time-of-flight shown in the figure was measured between the target and the neutral particle detector before (left) and after (right) the time walk correction. The spectrum was obtained under the condition that in coincidence with a signal in the neutral particle two charged particles were registered in the drift chambers. The time in the neutral particle detector was corrected in such a way as if the interaction point of particles was in the first row of the detector modules only. A clear signal originating from the gamma rays is seen over a broad enhancement from neutrons. This histogram shows that a discrimination between the signals originating from neutrons and gamma quanta can be done by a cut on the time of flight. For the gamma quanta the time-of-flight value is independent of their energy. This fact was used to determine the α and β coefficients. The right panel of figure 5.8 presents the analogous distribution for which a corrected time t_c was used for the time-of-flight calculation instead of the t_m .

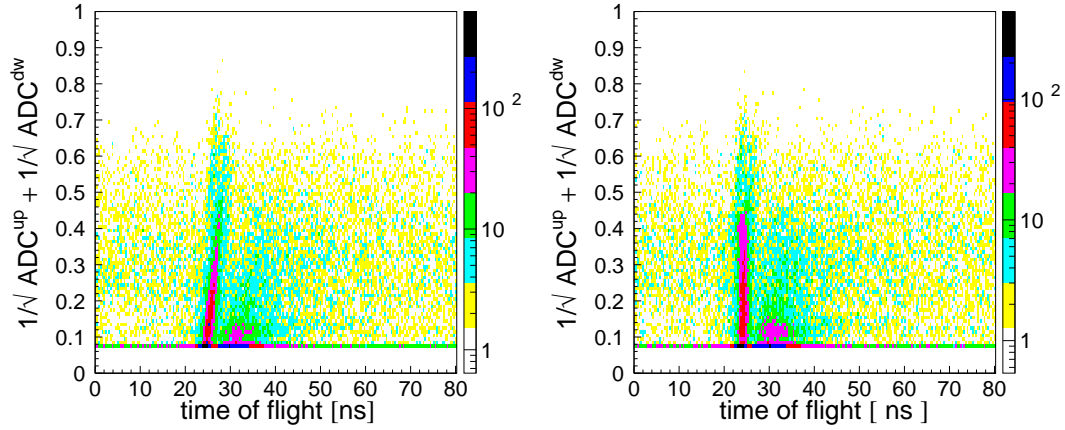


Figure 5.8: Time walk effect. A value of $\frac{1}{\sqrt{ADC^{up}}} + \frac{1}{\sqrt{ADC^{dw}}}$ measured in the neutral particle detector as a function of the time-of-flight (TOF^N) between the target and the neutral particle detector as obtained before (**left**) and after (**right**) time walk correction.

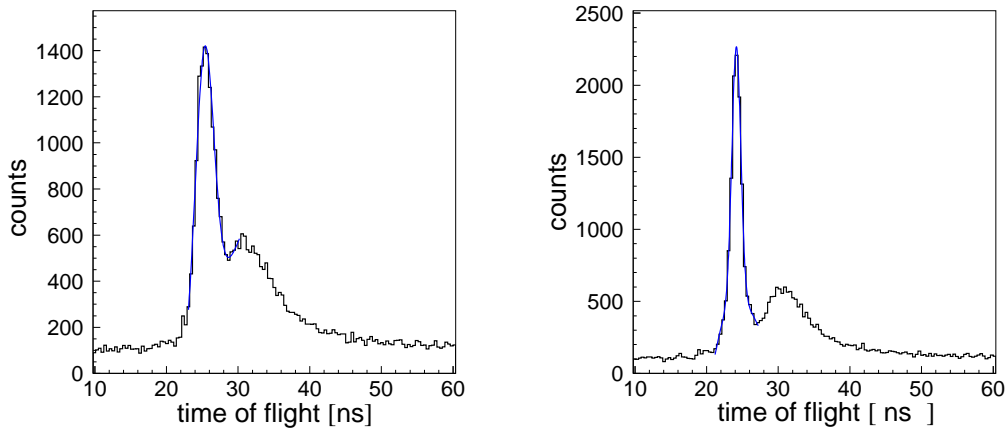


Figure 5.9: Distribution of the time-of-flight between the target and the neutral particle detector before (**left**) and after (**right**) time walk correction.

Figure 5.9 presents the projection of the distributions from figure 5.8 on the time-of-flight axis. Both distributions of the time-of-flight were fitted by a Gaussian function in the range where the clear peak originating from gamma quanta appears. The area around the peak was fitted by a second order polynomial. The left panel of figure 5.9 presents the distribution of the time-of-flight before the time walk correction, and the fit was resulting in a time-of-flight resolution of $\sigma = 1.2$ ns. The time-of-flight for which the corrected time in the neutral particle detector was used is shown in the right

panel of figure 5.9. The application of the time walk correction improved the time resolution to $\sigma = 0.6$ ns. It is worth noting that this is an overall time-of-flight resolution resulting from the time resolution of the neutron and S1 detectors and the accuracy of the momentum reconstruction of charged particles, needed for the determination of the time of the reaction in the target.

Figure 5.10 (left) shows the TOF distribution as a function of modules number. As expected from the known absorption coefficients [95], the gamma quanta are predominantly registered in the first row of the detector (see fig. 5.3) whereas the interaction points of the neutrons are distributed more homogeneously. Indeed, a clear signal originating from the gamma quanta is seen on the time-of-flight distribution, when taking into account signals from the first row of the neutron detector only, as it is shown in figure 5.10 (right).

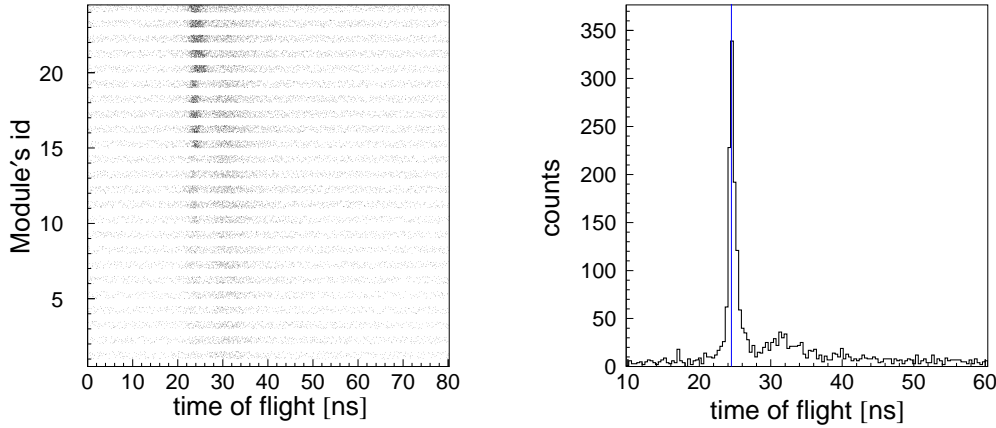


Figure 5.10: **Left:** Time-of-flight determined between the target and the neutron detector as a function of modules's number. **Right:** TOF^N distribution determined taking signals from first row of the neutral particle detector only.

Therefore, in order to raise the confidence to the determination of the general offset we have taken signals in the first row of the neutral particle detector. The data have been restricted only for the $pd \rightarrow pd\gamma X$ channel. In this case due to the baryon number conservation there is only one possible source of a signal in the neutral particle detector, namely a gamma quantum, which originates predominantly from the decay of π^0 mesons in the target.

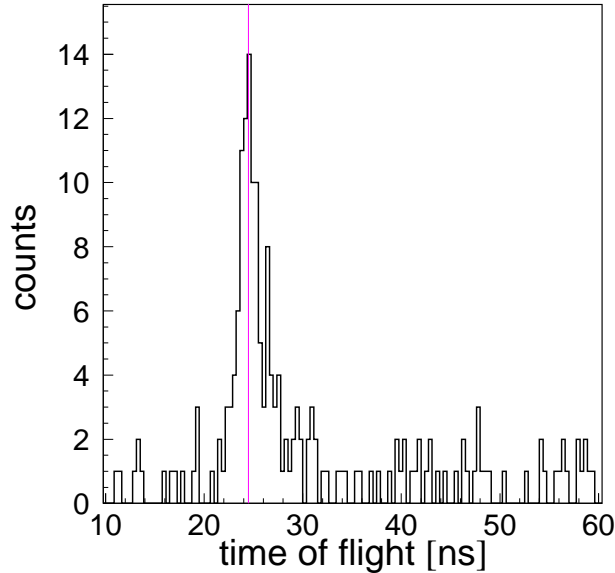


Figure 5.11: Time-of-flight distribution determined between the target and the neutron detector obtained under the assumption that additionally to a signal in the neutron detector one proton and one deuteron were identified from the signals in the drift chambers.

Figure 5.11 presents the experimental distribution of the time-of-flight between the target and the neutron detector for neutral particles, with the requirement that additionally to a signal in the neutron detector two charged particles were registered and that one of them was identified as a proton and the other as a deuteron³. As expected, in this spectrum only a signal from the gamma quanta is seen. The clear peak is positioned at the value equal to 24.5 ns, which corresponds to the time-of-flight for the light on the target-neutral particle detector distance.

5.3.4 Efficiency determination

The efficiency of the COSY-11 neutral particle detector – which is an important factor for determining the absolute values of cross sections – was determined using two independent simulation programs. For the first case, a procedure based on the GEANT-3 (**GE**ometry **ANd** **T**racking) code [96] was used for the simulation of the hadronic cascades induced in matter by neutrons. The same procedure was repeated using the FLUKA⁴ (**FLU**ktuierende **KA**skade) [97, 98] simulation program.

The efficiency of the neutron detector is given by the ratio of the number of events, for which an energy deposited in the scintillator material was larger than the threshold

³The method of identifying the particles registered by the drift chambers and scintillator hodoscopes is described in Chapter 6.

⁴The simulations were performed with the 2008 version.

value at least in one of 24 detection units to the number of generated neutrons. The value of the calculated efficiency as a function of the kinetic energy of the neutrons is shown in fig. 5.12 (left). Open squares denote result obtained using the GEANT-3 package and the outcome of the simulation using FLUKA-2008 is presented as black circles [99].

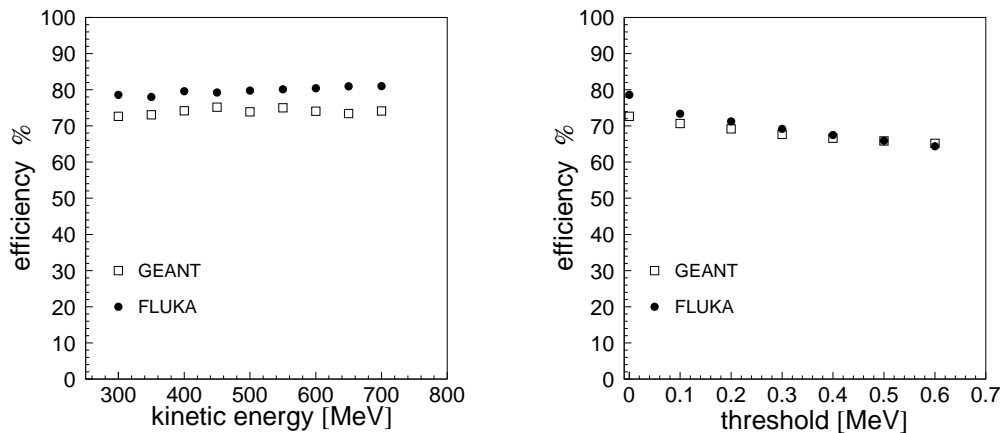


Figure 5.12: Left: The efficiency distribution as a function of the kinetic energy of the neutrons determined assuming that the threshold is equal to 0 MeV. **Right:** The relation between the threshold value and the efficiency for neutrons with an energy of 300 MeV.

The kinetic energy of the neutrons from the $pn \rightarrow pn\eta'$ reaction varies from 300 MeV up to 700 MeV for the 3.35 GeV/c beam momentum, and as can be inspected from fig. 5.12 (left) the efficiency is fairly constant in this range. It is important to mention that the results determined with the different programs are in agreement within $\pm 3\%$, independently of the threshold value.

Also studies of the variation of the efficiency depending on the threshold have been conducted. In the experiment the threshold was set to about 0.1 MeV and therefore the values from 0 up to 0.6 MeV were scanned. The result is presented in fig. 5.12 (right). For both, the GEANT and FLUKA-2008 simulation the efficiency changes by about 10% over the 0.6 MeV range of the threshold.

5.4 Veto detector

In order to distinguish between charged and neutral particles, in front of the first layer of the neutral particle detector an additional scintillator detector was installed as it is shown in figure 5.13. This detector – referred to as veto detector – is built out of four overlapping modules with dimensions of 400 mm \times 200 mm \times 4 mm. The lightguides and photomultipliers are mounted at the upper and lower edge of the modules such that the light signals are read out at both sides of the module.

It permits to reject the background originating from charged particles hitting the neutral particle detector. The discrimination between signals arising from the only possible remaining neutrons and gamma quanta is done by a cut on the time-of-flight (see chapter 6.).

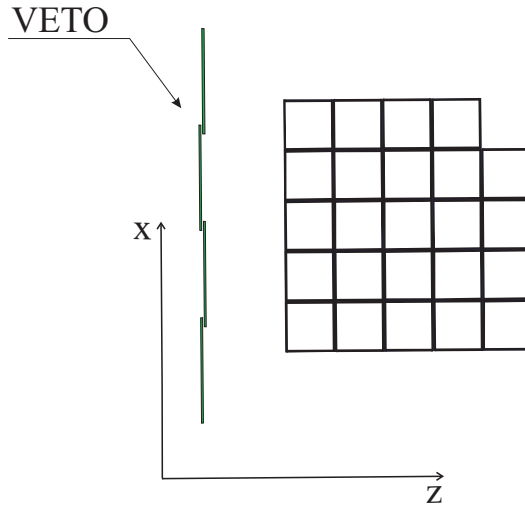


Figure 5.13: Layout of veto detector and neutral particle detector.

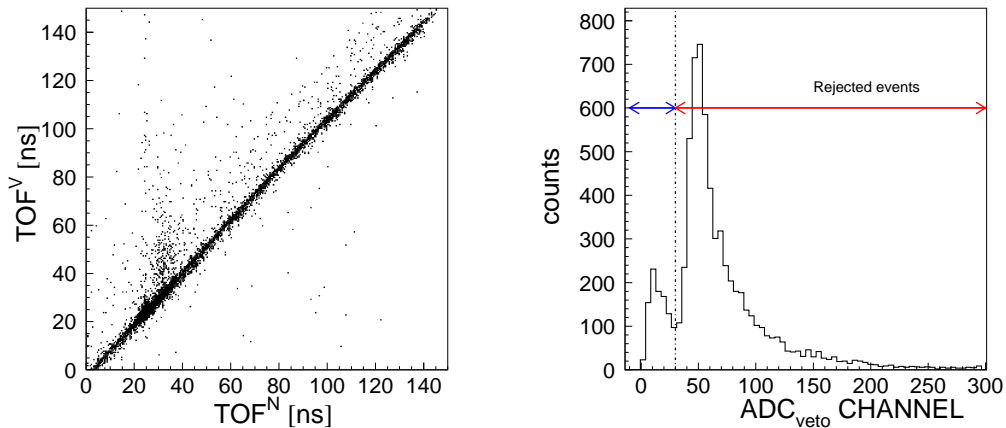


Figure 5.14: Left: The relation between the time-of-flight between the target and the neutral particle detector (TOF^N) and the time-of-flight between the target and veto detector (TOF^V). **Right:** ADC signals in the scintillator veto detector. The red arrow shows the ADC range for charged particles, which are rejected in the further analysis, whereas the blue arrow point to the ADC range for which events are interpreted as neutral particles. Noise signals are extinguished by the coincidence between the upper and lower photomultiplier.

As a first step of the time calibration of the veto detector the time-of-flight between the target and the veto detector has been calculated for each module separately assum-

ing that all time offsets are equal to zero. Next, the values of the calibration constants (offsets) were adjusted such that the time-of-flight value is equal for each module. Figure 5.14 (left) shows the relation of the time-of-flight between the target and the neutral particle detector (TOF^N) and the time-of-flight between the target and the veto detector (TOF^V). In principle this relation should be linear, however we observe events beyond the correlation line with time signals in the veto detector larger than in the neutral particle detector. This may happen when a neutral particle (which does not give a signal in the veto detector) induces electromagnetic or hadronic reactions in the neutral particle detector, and charged products of these reactions scattered backwards resulting in signals in the veto detector. This effect is reflected in figure 5.14 (right) which shows the ADC signals in one of the veto detector module. Two well separated peaks are observed. The peak in the range from 30 to 300 channels originates from events with charged particles which crossed the veto detector and then entered the neutral particle detector. When taking into account events which are above the correlation line only, the peak in the range between channel numbers 30 and 300 vanishes and only events with small ADC value up to 30 remain. Therefore, to discriminate between charged and neutral particles a cut on the veto detector ADC was applied, which is denoted in the figure 5.14 (right) by a dotted line.

5.5 Spectator detector

In order to identify the unobserved η' meson in the quasi-free $pn \rightarrow pnX$ process by means of the missing mass technique, one has to measure not only the momenta of outgoing proton and neutron, but also a determination of the pn reaction energy (\sqrt{s}) for all measured events is needed. The latter was realised by measuring the four-momentum vector of the spectator proton.

5.5.1 Scheme of the spectator detector

Before installation at the COSY-11 detection setup, the spectator detector has been used by the PROMICE/WASA collaboration at the CELCIUS storage ring of The Svedberg Laboratory [80]. Detectors which are located inside the scattering chamber, close to the interaction point, must be compatible with high vacuum and resistant to radiation environment. Moreover, a very good energy resolution is highly required in order to determine the four-momentum of the spectator protons. These factors exclude the use of plastic scintillator. Solid state devices are well suited for this purpose, therefore silicon was chosen as an active material in the spectator detector.

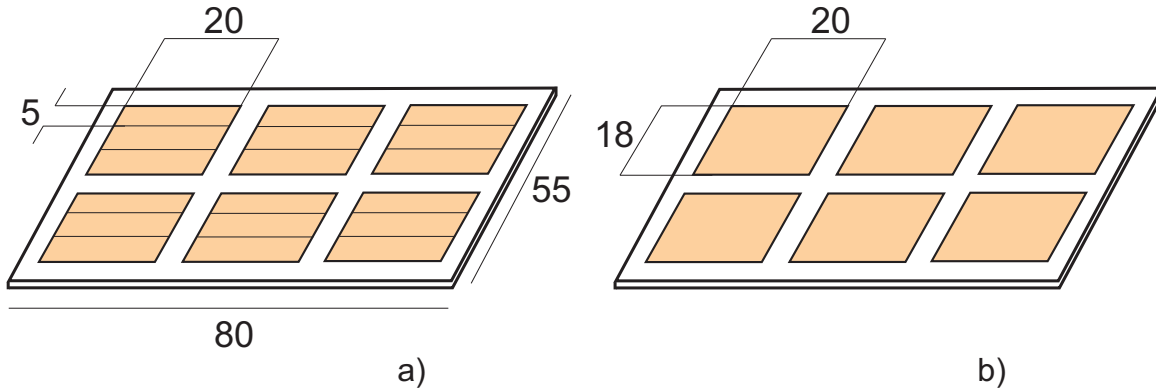


Figure 5.15: Schematic view of the spectator detector's single modules. **Left:** front layer (dE). **Right:** back layer (E). Indicated dimensions are given in mm.

The spectator detector consists of four double-layered modules. The layers are produced of $300\ \mu\text{m}$ thick silicon. Each of the front layers, which are the planes closer to the beam, contain eighteen silicon pads. The active area of a single pad amounts to $20\ \text{mm} \times 5\ \text{mm}$. The back layer contains six silicon pads, with an active area of $20\ \text{mm} \times 18\ \text{mm}$. The schematic picture of the front (dE) and the back (E) layers is shown in figure 5.15.

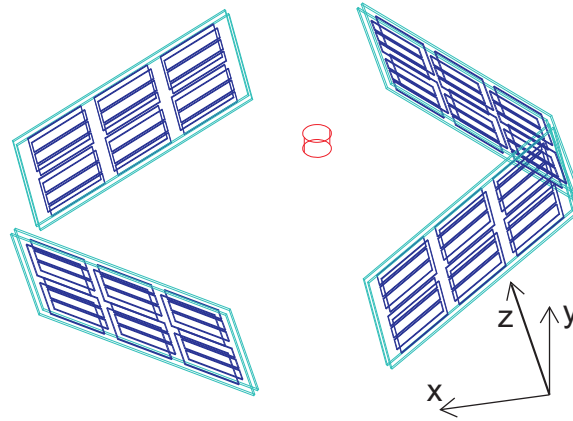


Figure 5.16: Schematic view of the spectator detector as installed at the COSY-11 facility. The z-axis corresponds to the direction of the beam, x is chosen parallel to the acceleration plane and y is vertical.

The silicon detector system is placed in the high vacuum at the COSY storage ring at a distance of about 5 cm upstream from the interaction point as it is schematically shown in figure 5.16. The active area covers about 22% of the full solid angle. The arrangement was a compromise between the technical needs for the installation and the angular resolution.

5.5.2 Energy calibration and position optimization

During the experiment, the charge of the signal induced in the detector by the particles, which is proportional to the energy deposited in the detection unit, has been measured. Denoting by ADC_1 and ADC_2 the measured charge in the first and second layer, respectively, the real energy loss can be expressed as: $\Delta E_1 = \alpha_1 ADC_1$ and $\Delta E_2 = \alpha_2 ADC_2$, where α_1 and α_2 are the calibration constants for two layers. The aim of the spectator detector calibration was to find the exact position of the detector and then to establish the calibration constants for each of the 96 silicon pads. The position of the spectator detector inside the beam pipe is described by only three parameters [82]. Variable dz denotes the translation along the z-axis in the main reference system (MARS). Parameters dl and $alpha$ account for translation and rotation of the flange used for supporting the spectator detector.

Differences in shapes of the $dE_1(dE_2)$ distributions are due to the fact that the effective thickness of the silicon modules of the detector "seen" by particles outgoing from the interaction point depends on the particles' incident angle on the detector surface. These variations allowed to find the exact position and orientation of the spectator detector inside the COSY-ring. Figure 5.17 presents an example of the calculated $dE_1(dE_2)$ distributions for a few arbitrarily chosen sets of parameters dz , dl , and $alpha$.

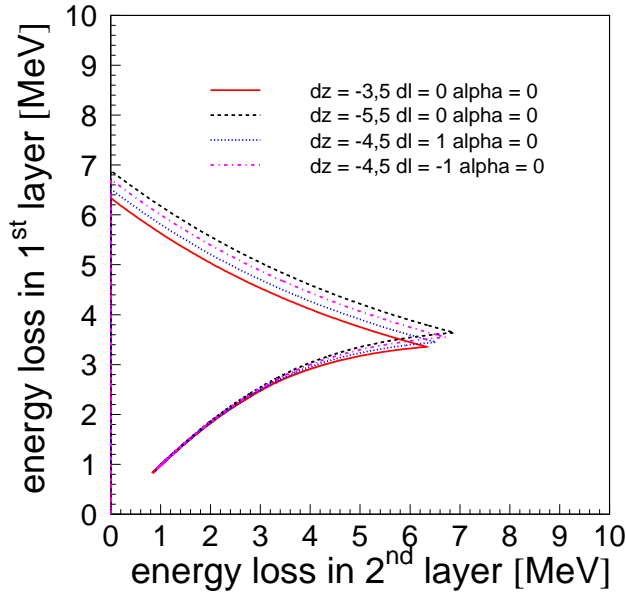


Figure 5.17: Energy losses in the first layer versus energy losses in the second layer as calculated for different positions of the spectator detector. The values of dz , dl are given in cm and $alpha$ is given in rad.

Assuming that the set of calibration constants (α_1 , α_2) are correct, experimental distributions of the $dE_1(dE_2)$ have been fitted to the calculated energy losses, and ex-

amined by varying the parameters describing the position of the spectator detector. After the determination of the new position of the detector the experimental data points on the $dE_1(dE_2)$ plot were fitted to the expected $dE_1(dE_2)$ function, with calibration constants α_1 and α_2 as free parameters for each detection pair. The procedure was repeated until the changes become negligible.

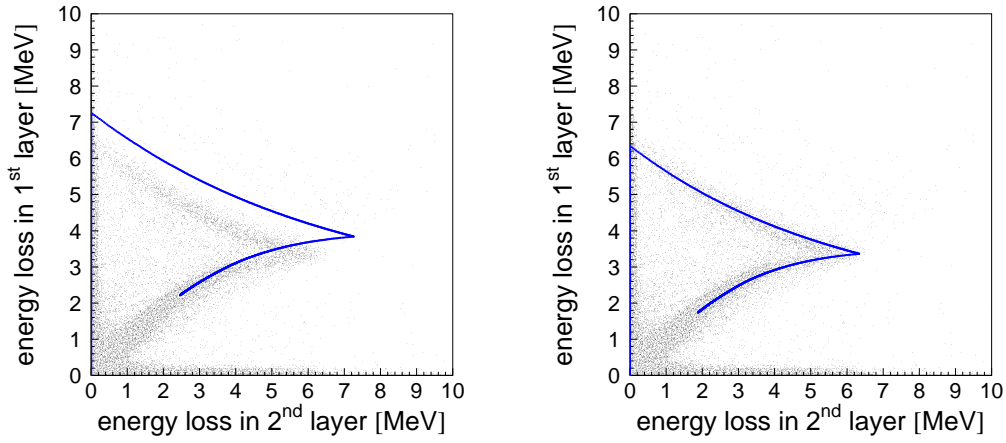


Figure 5.18: Energy losses in the first layer versus the second layer as measured at COSY-11 with a deuteron target and a proton beam with a momentum of 3.35 GeV/c before (**left**) and after (**right**) the calibration. Points represent the experimental data, whereas the theoretical calculations are indicated by the solid curve.

Figure 5.18 (left) shows the energy losses in the first layer versus the second layer before the calibration constants α_1 and α_2 were determined. The theoretical calculations are indicated by the solid curve. Fig. 5.18 (right) shows the corresponding plot after the calibration. The position of the spectator detector has been determined with an accuracy of ± 1 mm, consistent with the nominal values based on the geometrical designs of the setup and with the values obtained for the analysis of the $pn \rightarrow pn\eta$ test reaction [42]. Taking into account the size of the stream of the deuteron target with a diameter of 9 mm [100] the accuracy of the position determination within ± 1 mm is satisfactory.

Figure 5.19 shows the distribution of the excess energy with respect to the $pn\eta'$ system determined for the pn reaction. The solid histogram was obtained with the position of the spectator detector determined in the above described procedure.

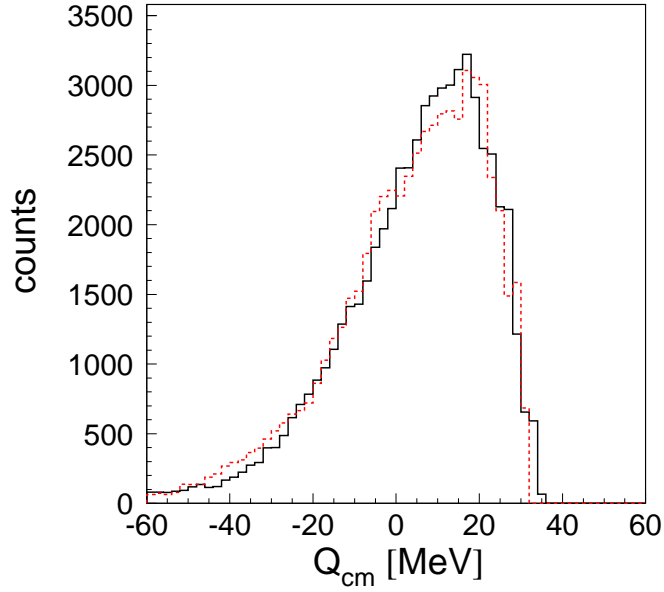


Figure 5.19: The distribution of the excess energy Q_{cm} determined with respect to the η' meson production threshold for the pn reaction as obtained with sets of parameters given by the present calibration (solid histogram) and with the orientation of the spectator detector determined previously from the analysis of the $pn \rightarrow pn\eta$ reaction [42] (dashed histogram).

As a cross check, the same data were analysed with the set of parameters describing the orientation of the spectator detector used previously in the analysis of the $pn \rightarrow pn\eta$ reaction. The result is presented as a dashed histogram.

6. Analysis of the experimental data

In this chapter the determination of the four-momentum vectors of the outgoing nucleons will be presented, and the missing mass technique as well as the method of background subtraction will be described.

6.1 Event selection

The first step of the off-line analysis of the experimental data was the software selection of events with one track reconstructed in the drift chambers and a signal in the neutral particle detector. As a next step particles registered in drift chambers were identified.

6.1.1 Proton identification

All charged particles originating from the proton-neutron reaction are separated from the proton beam in the magnetic field of the dipole magnet due to the smaller momenta and some of them are registered in the drift chambers and scintillator detectors (S1, S3). For each event the time-of-flight of particle between the S1 and S3 hodoscopes ($\Delta t = t_{S3} - t_{S1}$) is measured.

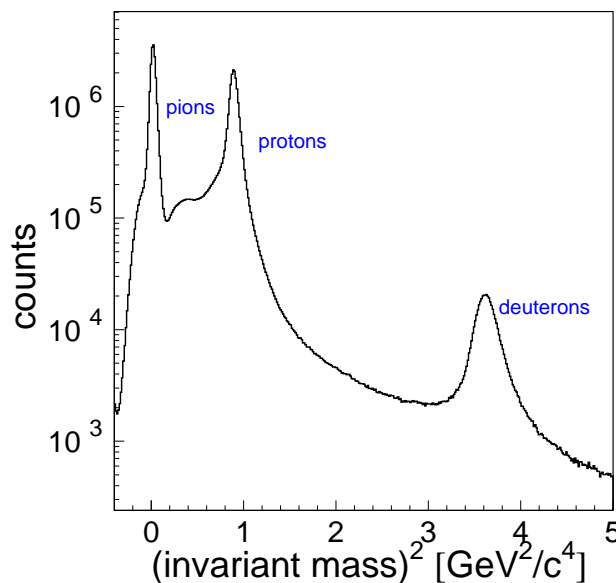


Figure 6.1: Distribution of the squared mass of charged particles originating from the proton-deuteron reaction performed at a beam momentum of 3.35 GeV/c.

Knowing the relative distances between these detectors, the velocity of the particles is calculated. Based on the signals in the drift chambers D1 and D2 the trajectories of particles are reconstructed. Furthermore the particles momenta are reconstructed by tracking the trajectories back through the known magnetic field of the dipole to the centre of the interaction region (the overlap between the target and the beam). The precision of the momentum reconstruction is equal to 6 MeV/c [54]. Having the velocity of the particle and its total momentum the squared invariant mass is determined.

Charged ejectiles can well be identified as shown in figure 6.1, where the distribution of the squared mass of charged particles originating from the proton-deuteron reaction performed at a beam momentum of 3.35 GeV/c is presented. Three clear peaks are evidently visible and correspond to the squared mass of pions, protons and deuterons. For the further analysis events with invariant mass corresponding to the proton mass are selected ($0.2 \text{ GeV}^2/c^4 \leq m^2 \leq 1.6 \text{ GeV}^2/c^4$).

After the particle identification, the time of the reaction (t_r^{real}) at the target point is obtained from the known velocity, trajectory and the time measured by the S1 detector.

6.1.2 Neutron identification

The determination of the four-momentum of the neutron is based on the time-of-flight measurement. The absolute value of the neutron momentum can be expressed as:

$$p = m_n \cdot \frac{l}{TOF^N} \cdot \frac{1}{\sqrt{1 - (\frac{l}{TOF^N})^2/c^2}}. \quad (6.1)$$

The m_n denotes the mass of the neutron, l is a distance from the centre of the interaction region to the central part of the module which fired as the first one. Thus the time-of-flight TOF^N is taken as a difference between the time of the reaction t_r^{reac} (known from the backtracking protons to the interaction point) and the shortest time of the neutral particle detector. The individual momentum components are determined from the angle defined by the centre of the hit segment. The momentum component along the y-axis is assumed to be zero since the sensitivity of the neutral particle detector is insufficient in the up-down direction. The granularity of the detector allows to determine the horizontal hit position with an accuracy of ± 4.5 cm.

Figure 6.2 presents the time-of-flight distribution between the target and the neutral particle detector as measured for neutral particles. The veto detector installed in front of the neutral particle detector discriminates signals originating from charged particles, however, it does not discern gamma quanta, which are detected in the neutral particle detector as well. Therefore, a clear signal originating from the gamma rays is seen at 24.5 ns over a broad yield from neutrons. This histogram shows that a discrimination between signals originating from neutrons and gamma quanta can be done by a cut on the time-of-flight. From the Monte Carlo simulations of the $pn \rightarrow pn\eta'$ reaction the largest expected momentum value of the neutron is equal to 1.4 GeV/c which corresponds to the time-of-flight value of 28 ns (see dashed histogram in fig. 6.2). This

allows to select events for which the time-of-flight is higher than 26 ns as it is indicated by an arrow in fig. 6.2. This condition excludes background of gamma quanta.

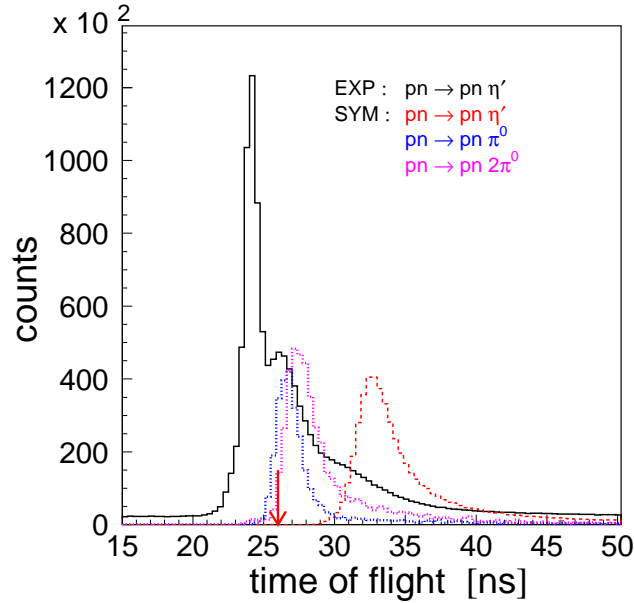


Figure 6.2: Distributions of the time-of-flight between the target and the neutral particle detector (T^N) for neutral particles. The experimental distribution depicted as a black solid histogram is compared with *i*) a simulated spectrum of the $pn \rightarrow pn\eta'$ reaction (dashed histogram) and *ii*) simulated exemplary background contributions (dotted histograms).

Background reactions with neutrons in the exit channel and their contribution to the time-of-flight distribution have been investigated also. The simulated reactions were analysed in the same way as the experimental data. The distributions of the time-of-flight for neutrons originating from quasi-free $pn \rightarrow pn$ pions reactions are shown in figure 6.2 with dotted histograms. The *time-of-flight cut* does not exclude neutrons from different quasi-free reactions, and this will constitute the main background which must be subtracted (see section 6.3.1).

6.2 Determination of the excess energy

Having proton and neutron identified, the consecutive software selection of the experimental data was applied. In addition to one proton registered in the drift chambers and a neutron in the neutral particle detector, at least a signal in one layer of the spectator detector was demanded.

As it was discussed in chapter 3, to establish the excess energy Q_{cm} with respect to the $pn \rightarrow pn\eta'$ reaction, the measurement of the proton spectator momentum, and the determination of the total energy \sqrt{s} is indispensable.

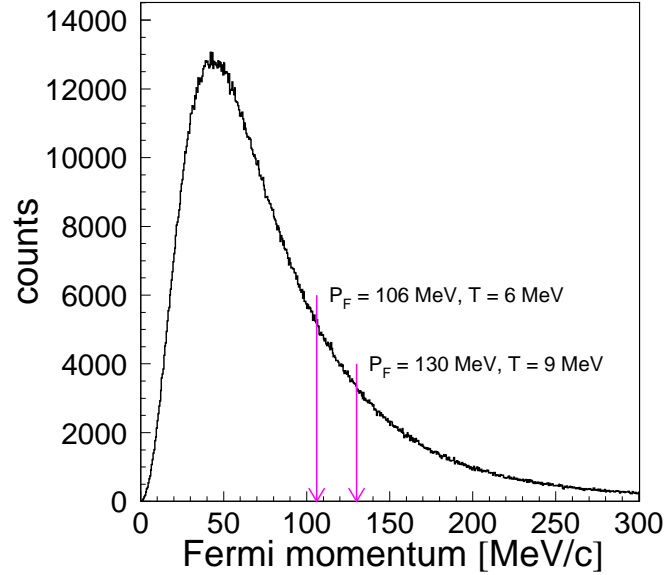


Figure 6.3: Simulated distribution of the Fermi momentum of nucleons inside the deuteron based on the Paris potential [60]. Arrows depict values of momenta for which the spectator protons are stopped in the first or in the second layer of the spectator detector.

The spectator detector is designed such, that protons impinging perpendicular to the detector surface and having a kinetic energy of less than 6 MeV are stopped in the first layer (dE). Protons with kinetic energy in the range between 6 MeV and 9 MeV are stopped in the second layer (E). All protons with $T_{spec} > 9$ MeV are passing through both layers of the spectator detector. As it is seen in figure 6.3 a large number of spectator protons (with maximum Fermi momentum of 130 MeV) will be stopped in the detector. In the experiment we registered the spectator protons with momenta larger than 35 MeV/c since it is not possible to separate the energy losses for protons with lower momenta from the noise level. The *spectator noise cut* has been performed for each pad of the detector separately, using the spectra of energy loss triggered by a pulser with a frequency of 1 Hz additionally to other experimental triggers. Figure 6.4 (left) shows the energy losses in the 1st layer of the spectator detector versus the 2nd layer. Slow spectator protons are stopped in the first or second layer of the detector whereas fast particles (mainly charged pions) cross both detection layers. Signals from deuterons are not observed since deuterons cannot be emitted backward due to the kinematics. Having the deposited energy (T_{spec}) and the emission angles ($\theta_{spec}, \phi_{spec}$) we calculate the energy of the spectator proton ($E_{spec} = T_{spec} + m_p$) and its momentum (\vec{p}_{spec}). Figure 6.4 (right) presents the momentum distribution of protons considered as spectator (points) compared with simulations taking into account a Fermi motion of nucleons inside the deuteron (solid line).

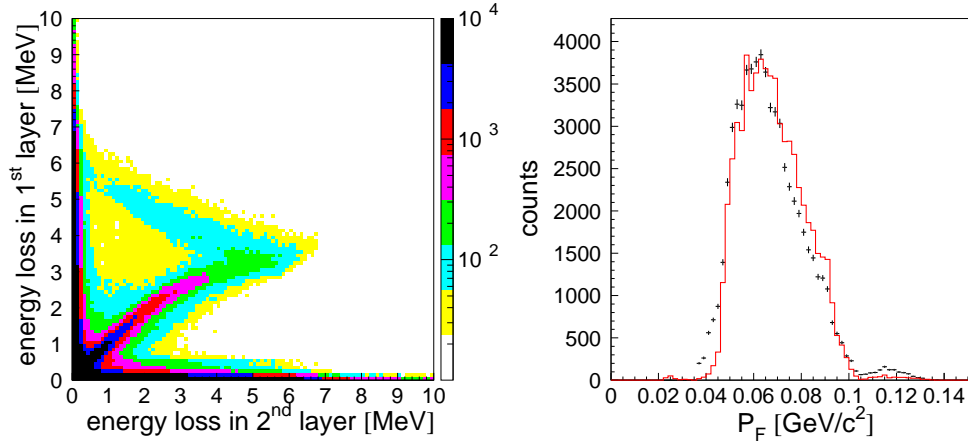


Figure 6.4: **Left:** Energy losses in the first layer versus the second layer as measured with a deuteron target and a proton beam with a momentum of 3.35 GeV/c. **Right:** Momentum distribution of the spectator proton as reconstructed in the experiment (points) in comparison with simulation calculations taking into account Fermi momentum distribution of nucleons inside the deuteron according to the Paris potential [60] (solid histogram). The simulated events were analysed in the same way as the experimental data.

The total energy (\sqrt{s}) available for the quasi-free proton-neutron reaction can be calculated for each event from the vectors of the spectator momentum and beam momentum.

$$\begin{aligned}
 s &= (E_b + E_t)^2 - (\vec{p}_b + \vec{p}_t)^2, \\
 E_t &= m_d - E_{spec}, \\
 \vec{p}_t &= -\vec{p}_{spec}
 \end{aligned}
 \tag{6.2}$$

E_b and \vec{p}_b are the energy and momentum vector of the proton beam. E_t and \vec{p}_t are the energy and momentum vector of the neutron target, calculated from the energy and the momentum of spectator proton (E_{spec} , \vec{p}_{spec}); m_d and m_p denote the deuteron and proton masses, respectively. The excess energy with respect to the $pn \rightarrow pn\eta'$ process is equal to:

$$Q_{cm} = \sqrt{s} - (m_p + m_n + m_{\eta'}),
 \tag{6.3}$$

where m_p , m_n and $m_{\eta'}$ are the mass of proton, neutron and the η' meson, respectively. The experimental distribution of the excess energy is shown in the left panel of figure 6.5. As was previously discussed, with one fixed value of the beam momentum – due to the Fermi motion of nucleons inside the deuteron – one can scan a broad range of the excess energy, from 0 up to 32 MeV for $p_{beam} = 3.35$ GeV/c. Negative values of the excess energy correspond to events, when the total energy in the centre-of-mass frame (\sqrt{s}) was insufficient for the production of a η' meson and only the production of multi-pion background events could occur. For excess energies larger than zero, additionally to the pion production also the η' meson is created. A simulated distribution

of the excess energy for quasi-free $pn \rightarrow pn\eta'$ reaction, calculated with respect to the $pn\eta'$ system is depicted in figure 6.5 (right).

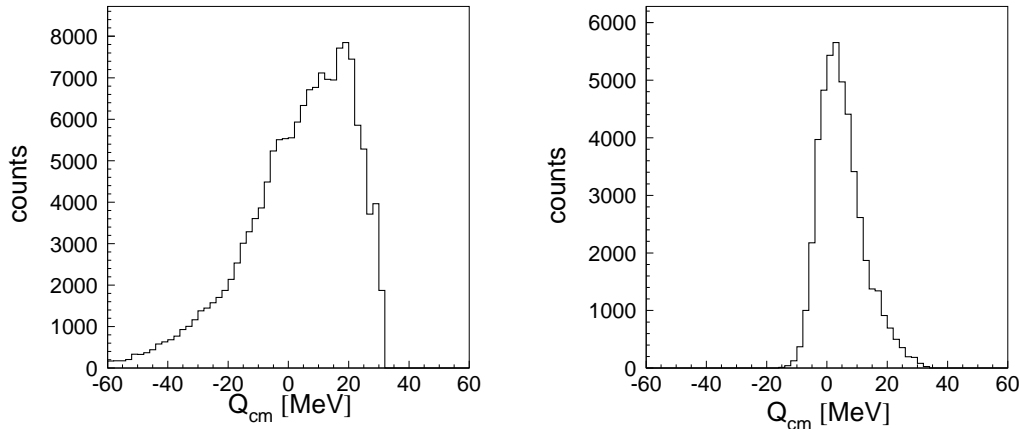


Figure 6.5: Distributions of the excess energy Q_{cm} for the quasi-free $pn \rightarrow pnX$ reaction determined with respect to the $pn\eta'$ threshold as obtained experimentally (**left**) and for Monte Carlo simulation (**right**). In the simulation all known detector features were taken into account (for details see text).

A number of factors influence the registered yield of the $pn \rightarrow pn\eta'$ reaction as a function of the excess energy: *i*) the Fermi momentum distribution of nucleons in the deuteron target, *ii*) the relative settings of the spectator detector and the target, *iii*) the absolute momentum of the proton beam and *iv*) the acceptance of the COSY-11 detection setup. Due to the rapid growth of the total cross section close to the production threshold the accuracy of the excess energy determination is one of the most important parameters and it is mandatory to estimate correctly its uncertainty. The accuracy of the excess energy determination was estimated based on Monte Carlo simulations. For this purpose we have simulated $N_0 = 10^9$ events of the $pn \rightarrow pn\eta'$ reaction taking into account the Fermi motion of the nucleons inside the deuteron, the size of the target (diameter ~ 9 mm), the spread of the beam momentum ($\sigma p_b = 1.5$ MeV/c) and the horizontal ($\sigma(x) \sim 2$ mm) and vertical ($\sigma(y) \sim 4$ mm) beam size [101]. Simulated data have been analysed in the same way as the experimental data, taking into consideration the energy- and time-resolution of the detectors.

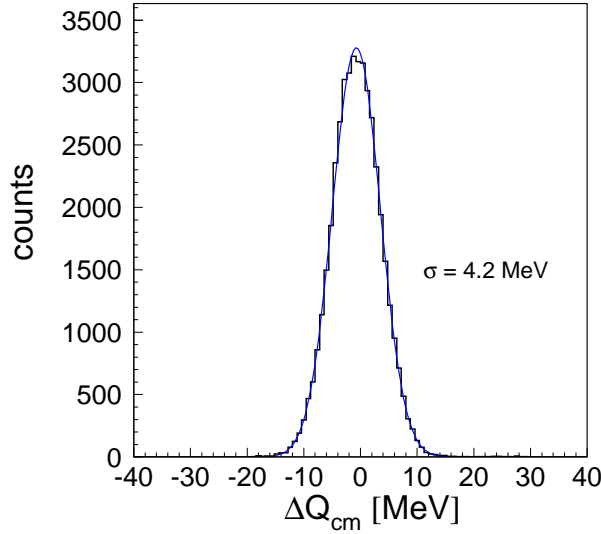


Figure 6.6: Difference between the generated (Q_{cm}^{gen}) and reconstructed (Q_{cm}^{rec}) excess energy for the $pn \rightarrow pn\eta'$ reaction simulated for a proton beam momentum of 3.35 GeV/c and a deuteron target.

Figure 6.6 presents the distribution of differences between the generated excess energy (Q_{cm}^{gen}) and the reconstructed excess energy from signals simulated in the detectors (Q_{cm}^{rec}). The distribution of $\Delta Q_{cm} = Q_{cm}^{gen} - Q_{cm}^{rec}$ was fitted by a Gaussian function resulting in an excess energy resolution of $\sigma(Q_{cm}) = 4.2$ MeV. For the $pn \rightarrow pn\eta$ reaction near threshold a standard deviation of the excess energy was derived to be $\sigma(Q_{cm}) = 2.2$ MeV [42], which is comparable with $\sigma(Q_{cm}) = 1.8$ MeV obtained at similar conditions at the PROMICE/WASA setup [80].

6.3 Identification of the $pn \rightarrow pn\eta'$ reaction

The η' mesons produced in the $pn \rightarrow pn\eta'$ reaction are identified using the missing mass technique.

Knowing the four-momentum vectors of a proton and a neutron in the initial and final state, and employing the principle of momentum and energy conservation one can calculate the squared mass of the unmeasured particle or group of particles:

$$m_x^2 = E_x^2 - \vec{p}_x^2 = (E_b + E_t - E_p - E_n)^2 - (\vec{p}_b + \vec{p}_t - \vec{p}_p - \vec{p}_n)^2 \quad (6.4)$$

where,

E_b, \vec{p}_b is the energy and momentum of proton beam,

E_t, \vec{p}_t is the energy and momentum of neutron target,

E_p, \vec{p}_p is the energy and momentum of outgoing proton, and

E_n, \vec{p}_n is the energy and momentum of outgoing neutron.

The method of the proton identification and of the neutron selection was described in sections 6.1 and 6.2.

Before the missing mass was calculated, the collected data were grouped according to the excess energy. The available range of the excess energy Q_{cm} above the η' meson production threshold (from 0 to 32 MeV) has been divided into four bins, each 8 MeV wide. The choice of the interval width is a compromise between the statistic and the resolution and reflects the accuracy (FWHM) of the determination of the excess energy. Due to the very low statistic and small acceptance, events corresponding to the excess energy interval between 24 and 32 MeV are not taken for further analysis. Moreover, in this range the excess energy distribution is very sensitive to changes of the position of the spectator detector, what can be seen from figure 6.7 showing the distribution of the excess energy Q_{cm} determined for the $pn \rightarrow pn\eta'$ reaction as obtained with the position of the spectator detector fixed based on the data (solid histogram) and with the detector shifted from this position in the z-axis direction by 3 mm (dashed histogram). A significant reduction of number of counts in the interval between 24 and 32 MeV is clearly observed.

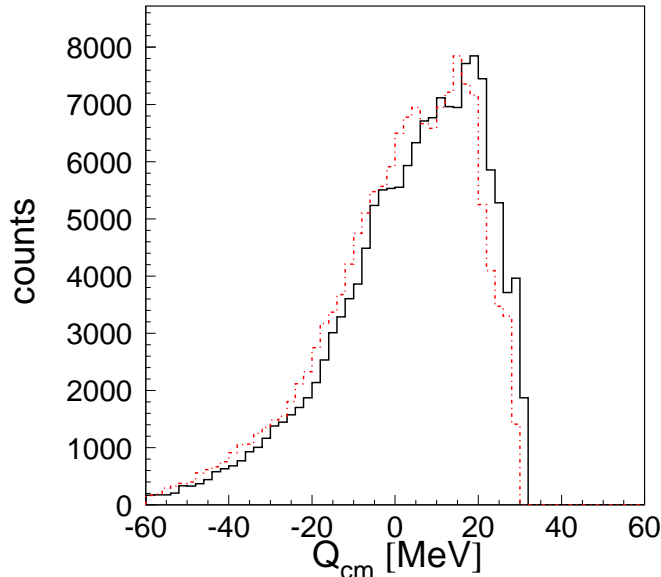


Figure 6.7: The distribution of the excess energy Q_{cm} determined for the $pn \rightarrow pn\eta'$ reaction as obtained with the position of the spectator detector fixed based on the data (solid histogram) and with the detector shifted from this position in z-axis direction by 3 mm (dashed histogram). The shift of 3 mm is done for demonstration purpose. Note that in chapter 5.5.2 the accuracy of the position determination of the spectator detector was established to be ± 1 mm.

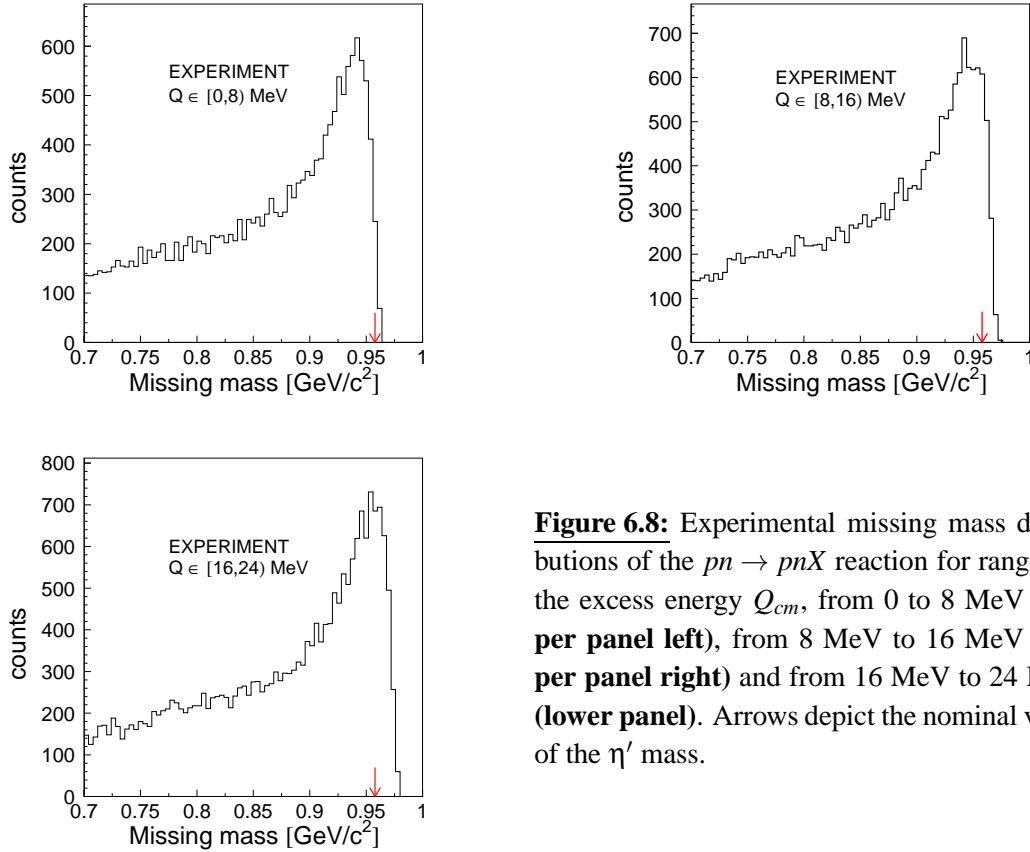


Figure 6.8: Experimental missing mass distributions of the $pn \rightarrow pnX$ reaction for ranges of the excess energy Q_{cm} , from 0 to 8 MeV (**upper panel left**), from 8 MeV to 16 MeV (**upper panel right**) and from 16 MeV to 24 MeV (**lower panel**). Arrows depict the nominal value of the η' mass.

Figure 6.8 presents the experimental missing mass spectra of the $pn \rightarrow pnX$ process calculated for the excess energy ranges $Q_{cm} = [0, 8)$ MeV, $Q_{cm} = [8, 16)$ MeV and $Q_{cm} = [16, 24)$ MeV. For all missing mass distributions we observe an increase of counting rate towards the higher masses ending at the kinematical limit. The shape is mostly due to the detector acceptance. A signal from η' meson production is expected on top of the multi-pion mass distribution at the position corresponding to the η' mass – denoted by the arrow – however no enhancement around this region is seen. Therefore, to extract number of η' events, the multi-pion background must be disentangled from the missing mass distributions.

6.3.1 Method of background subtraction

The background investigation in the missing mass spectrum of the quasi-free $pn \rightarrow pnX$ reaction is a challenging task, especially close to threshold. This is even more difficult when the resolution of the mass determination is comparable with the excess energy. The method of separating contributions from the multi-pion production in the missing mass spectrum of the quasi-free $pn \rightarrow pnX$ reaction is described in details in a dedicated article [102]. Therefore, here only the general principle will be pointed out.

One can disentangle the number of $pn \rightarrow pn\eta'$ events from single- and multi-pion background without conducting model-dependent simulations by comparison of the missing mass distributions for the negative values of Q_{cm} , when only pions can be created and for Q_{cm} larger than zero.

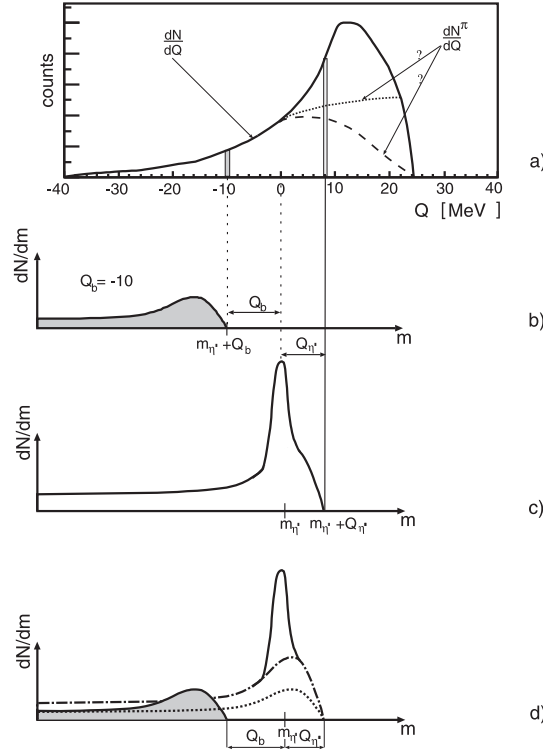


Figure 6.9: Schematic presentation of the background construction and subtraction. *a)* Distribution of the excess energy with respect to the $pn \rightarrow pn\eta'$ reaction. *b)* and *c)* Form of the missing mass spectra as derived for negative (Q_b) and positive ($Q_{\eta'}$) values of Q . *d)* The shape of the background constructed from the shape of the multi-pion mass distribution (shaded histogram), shifted to the kinematical limit (dotted line) and normalised at low masses (dash-dotted line). The picture has been adapted from reference [102]

Let us assume that the number of registered events is very large and that the shape of the reconstructed invariant mass of the multi-pion background is independent of the excess energy Q . The form of the background could then be determined from the missing mass spectrum dN^π/dm from an infinitesimal range at any negative value of Q . The shape of the background can be expressed in terms of a normalised function $B(m_{\eta'} + Q - m)$ of the difference between the kinematical limit ($m_{\eta'} + Q$) and the given mass m . Assuming infinite statistics, one could divide the positive Q range into very narrow subranges within which the resultant missing mass spectrum would be a sum of a signal from the meson (η') and the form B . This situation is schematically depicted in figure 6.9. In order to derive a signal of the meson from the missing mass spectrum for positive Q it would be sufficient to subtract from this spectrum a missing

mass distribution determined for negative Q values after the shift of the latter to the kinematical limit (dotted line) and normalisation at the very low mass values where no events from the η' meson are expected (dashed-dotted line) [102]. At real experimental conditions, due to the finite statistics, the missing mass spectrum is studied in finite intervals of Q , what alters the form of the multi-pion background. Therefore one has to take as narrow intervals of Q as reasonable, taking into account the experimental resolution in Q and assuming that within this range the multi-pion background is constant. An natural choice is to take the width of the Q subranges equal to the FWHM of the resolution of the Q determination.

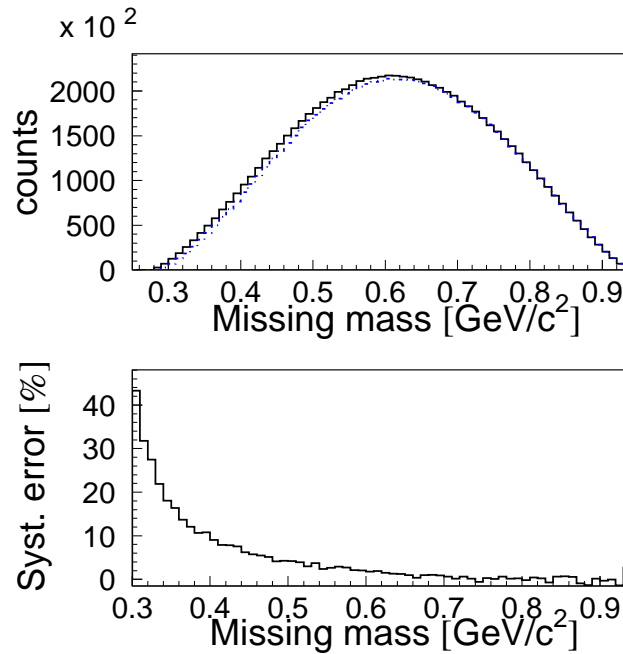


Figure 6.10: Upper: Missing mass distribution determined for the $pn \rightarrow pn\pi\pi$ reaction at the excess energy range $Q_{cm} = (-30,-20)$ MeV (dotted line) and for the excess energy range $Q_{cm} = (-20,-10)$ MeV (solid line). The excess energy was calculated with respect to the $pn\eta'$ threshold. The dotted histogram was shifted to the kinematical limit of the solid histogram. **Lower:** Difference between the spectra of the upper panel normalised to the solid line.

In order to gain more certainty that the measured shape of the multi-pion background does not alter significantly with changes of the excess energy, we have performed simulations of the background originating from two pion creation in proton-neutron collisions. Figure 6.10 presents the missing mass distribution of the two pion system produced via the $pn \rightarrow pnX$ reaction. Events were simulated at the excess energy intervals of $Q_{cm} = (-30,-20)$ MeV and $Q_{cm} = (-20,-10)$ MeV with respect to the $pn\eta'$ system. From the comparison of the form of both spectra one realises that there is no noticeable difference in the shape at the missing mass range of the η' mass. The systematic error caused by the subtraction of the shifted and normalised histogram is

shown in the lower panel of figure 6.10. It is demonstrated that the fractional systematic error due to the multi-pion background subtraction is in order of one per cent of the background value within the range of 200 MeV in the vicinity of the kinematical limit.

6.3.2 Background subtracted missing mass distribution

As was already discussed, events with excess energies larger than zero were divided into intervals of $\Delta Q_{cm} = 8$ MeV. For each interval the missing mass was calculated separately. Next, for each distribution of the missing mass spectra, a corresponding background spectrum has been constructed from events with Q_{cm} belonging to the $(-30, -10)$ MeV range applying the method described in the previous section. As a cross check, to gain more confidence about the applied procedure we have constructed alternative background distributions taking events from a Q_{cm} range from -20 MeV to 0 MeV. The result of this investigation has shown a consistency of both background shapes in the order of 1%.

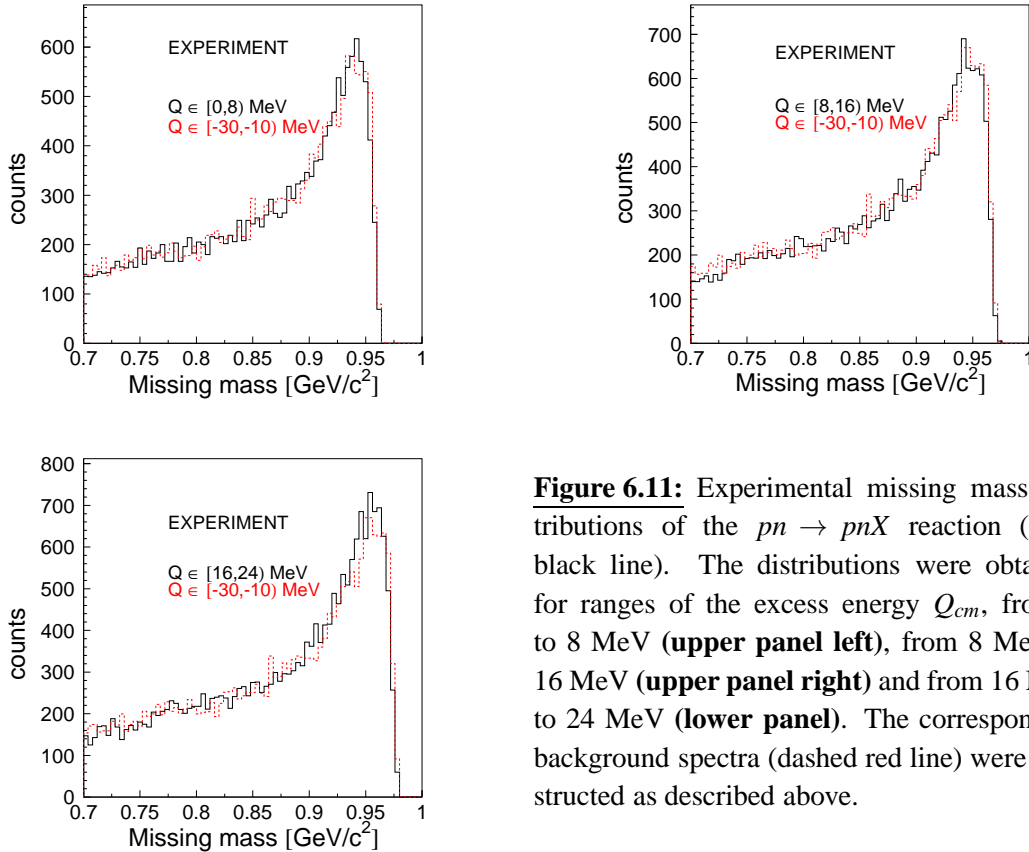


Figure 6.11: Experimental missing mass distributions of the $pn \rightarrow pnX$ reaction (solid black line). The distributions were obtained for ranges of the excess energy Q_{cm} , from 0 to 8 MeV (**upper panel left**), from 8 MeV to 16 MeV (**upper panel right**) and from 16 MeV to 24 MeV (**lower panel**). The corresponding background spectra (dashed red line) were constructed as described above.

Afterwards, to each distribution for $Q_{cm} \geq 0$ the corresponding background spectrum has been normalised for mass values smaller than $0.25 \text{ GeV}/c^2$ where no events from the η' are expected. In this region events correspond to the one pion production,

for which the total cross section remains nearly constant in the shown range of the excess energy. Figure 6.11 shows the experimental mass distribution for signal (solid black histogram) as determined for the excess energy ranges $[0, 8)$ MeV, $[8, 16)$ MeV, and $[16, 24)$ MeV. The dashed red line depicts the background spectrum, shifted to the kinematical limit and normalised accordingly.

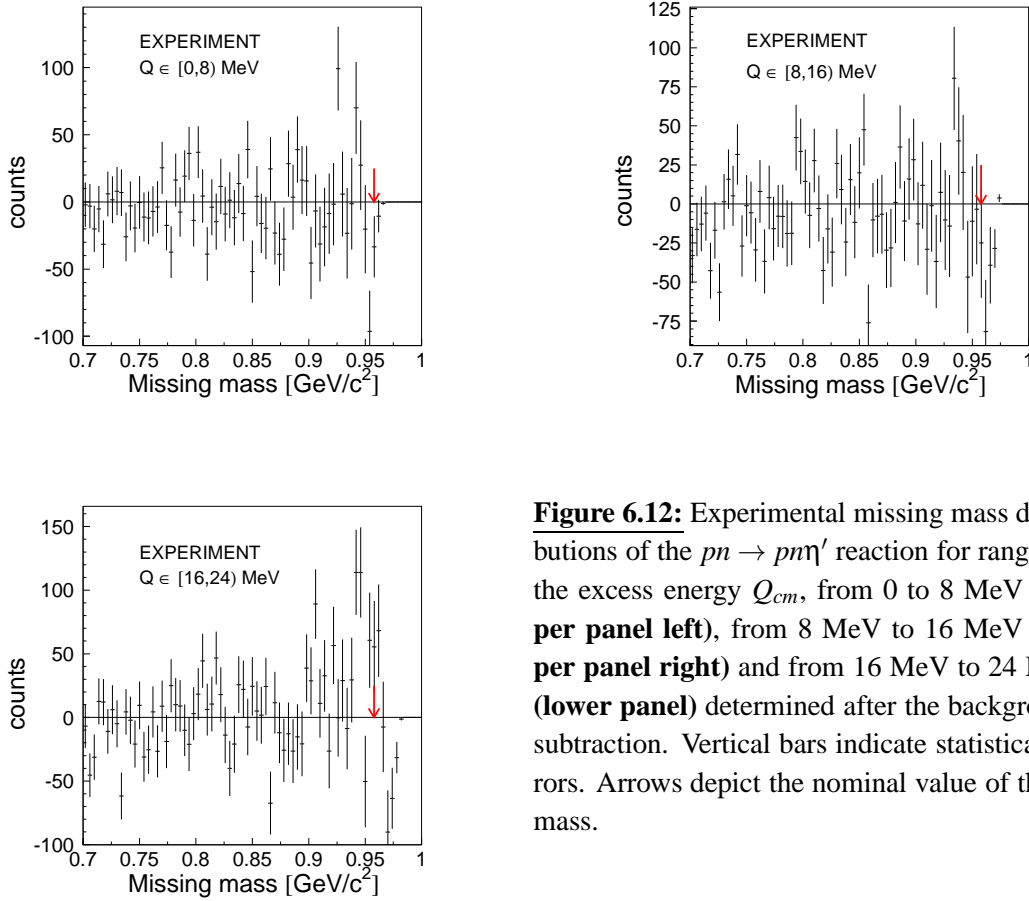


Figure 6.12: Experimental missing mass distributions of the $pn \rightarrow pn\eta'$ reaction for ranges of the excess energy Q_{cm} , from 0 to 8 MeV (**upper panel left**), from 8 MeV to 16 MeV (**upper panel right**) and from 16 MeV to 24 MeV (**lower panel**) determined after the background subtraction. Vertical bars indicate statistical errors. Arrows depict the nominal value of the η' mass.

Figure 6.12 shows distributions of the missing mass for the $pn \rightarrow pn\eta'$ reaction as determined after subtraction of the background. Due to the low statistics and very low signal-to-background ratio the signal from η' meson created in the proton-neutron collision is statistically insignificant. Therefore, in this thesis we can only estimate the upper limit for the η' meson production in the $pn \rightarrow pn\eta'$ reaction.

Expected missing mass distributions from the Monte Carlo simulations are presented in figure 6.13. In the simulation, based on the GEANT-3 package we took into account the momentum spread of the beam, beam and target dimensions, Fermi motion of nucleons inside the deuteron target, the geometry of the COSY-11 detector setup, multiple scattering of particles and other known physical effects were included in the GEANT-3 package [96]. The simulated data have been analysed in the same way as

the experimental one, taking into consideration position-, time- and energy-resolution of all detector components.

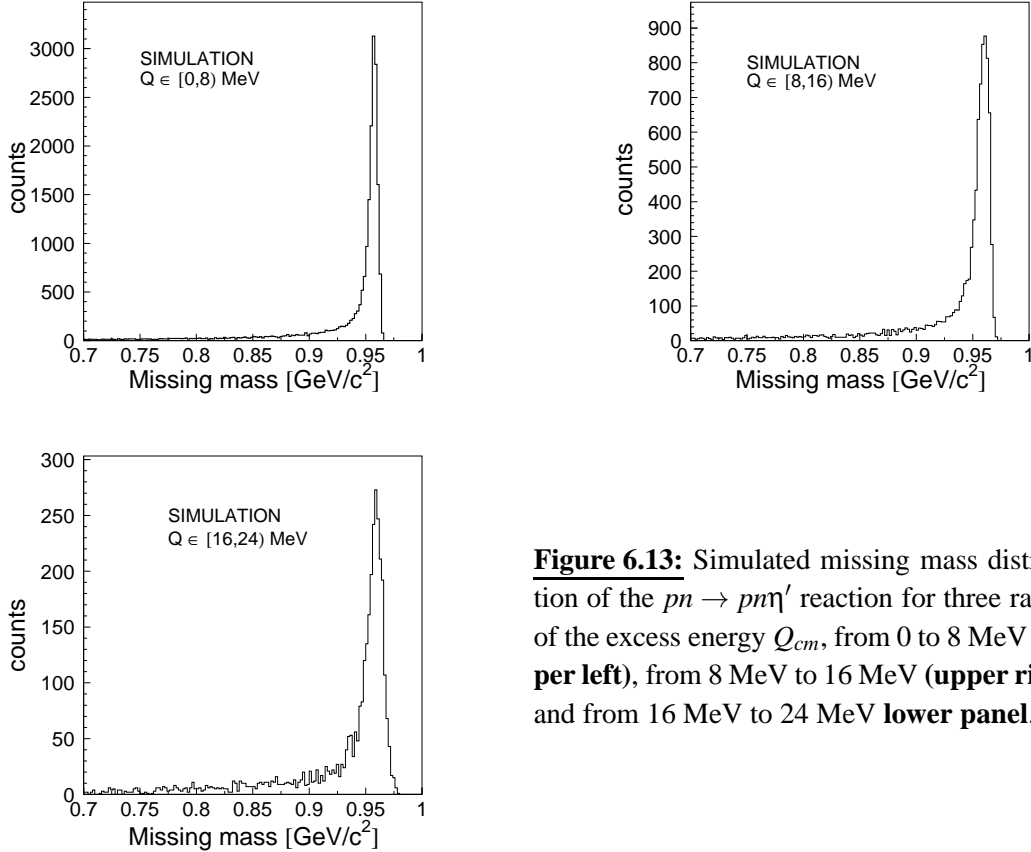


Figure 6.13: Simulated missing mass distribution of the $pn \rightarrow pn\eta'$ reaction for three ranges of the excess energy Q_{cm} , from 0 to 8 MeV (**upper left**), from 8 MeV to 16 MeV (**upper right**) and from 16 MeV to 24 MeV **lower panel**.

In order to estimate the systematic error of the number of the $pn \rightarrow pnX$ events, the change of the missing mass spectra has been studied by varying different parameters describing the experimental conditions (position of the detectors, time offsets, etc.) in the analysis and in the simulation. Change of the global time offset of the neutral particle detector by one standard deviation of its time resolution ($\sigma_t^N = 0.4$ ns) resulted in systematic error of the missing mass distribution of 3%. As was discussed above, the systematic error due to the method used for the background subtraction is equal to 1%. The uncertainty due to the model dependence calculation of the Fermi momentum distribution is equal to 2% [82] and was estimated as the difference between results determined using the Paris [60] and the CD-Bonn [103] potentials. A displacement of the spectator detector (fixed based on the experimental data) by 1 mm (standard deviation of its position accuracy) changes the number of events by 5%.

7. Luminosity determination

For the calculation of the absolute total cross section of the $pn \rightarrow pn\eta'$ reaction the knowledge of the integrated luminosity is mandatory. The determination of the luminosity is based on the registration of the quasi-free $pp \rightarrow pp$ reaction, which was measured simultaneously with the η' meson production in proton-neutron collisions. In this kind of scattering, the proton from the beam interacts with the proton bound inside the deuteron target. The outgoing protons were measured in coincidence with the S1 and S4 scintillator detectors (see figure 4.2). In the S4 scintillator and the position sensitive silicon detector - referred to as the monitor detector - the recoil proton is registered. The forward proton is bent in the magnetic field of the dipole towards the drift chambers and S1 scintillator detector. Figure 7.1 shows the measured correlation between the position in the S1 scintillator and the position in the monitor detector. The lower band arises from the free proton-deuteron scattering, whereas the broad distribution results from the quasi-free proton-proton scattering events.

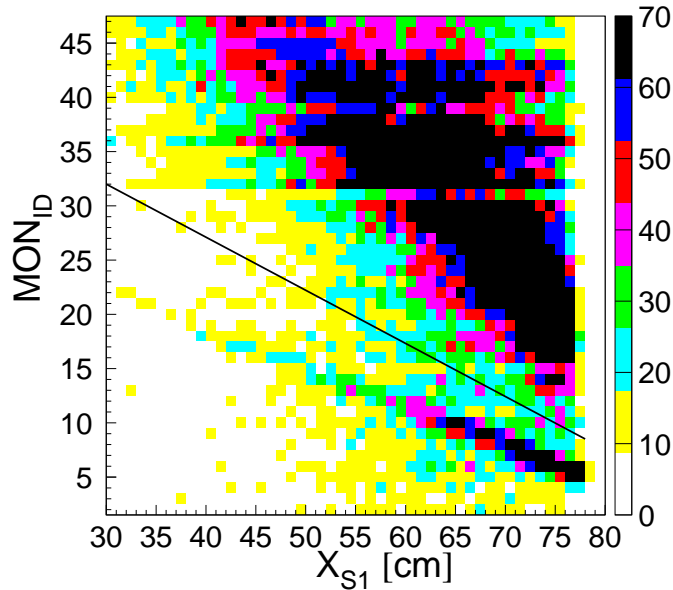


Figure 7.1: The hit position of the recoil particles measured in the monitor detector versus the position in the S1 detector of forward scattered particles. The pads number 15, 32 and 39 have lower counting rate due to a failure in their signal amplification. This imperfection was taken into account in the analysis.

In the off-line analysis we have separated the quasi-free proton-proton from the proton-deuteron scattering applying a cut on the histogram as depicted by black line in

figure 7.1. For the further analysis only events above the black line were taken. The determination of the luminosity by means of the quasi-free proton-proton reaction measurement takes advantage of the availability of the precise cross sections determined by the EDDA group [104]. The normalisation uncertainty of the EDDA differential cross sections is relatively small (equal to circa 4% [104, 105]), whereas the systematic error arising from the determination of the corresponding differential cross section for the proton-deuteron scattering is in order of 10% [106].

The momentum of the fast proton is determined by tracking back the trajectory reconstructed from the signals in the drift chambers through the magnetic field to the target point. Figure 7.2 (left) shows the parallel versus the transversal component of the reconstructed momentum of the forward scattered proton. Events corresponding to the elastically scattered protons are seen near the kinematical ellipse, which is marked as a dashed line. The right panel of figure 7.2 presents an analogous spectrum obtained from the Monte Carlo simulations taking into account the acceptance of the detection system, the Fermi motion of the nucleons, and the variation of differential cross section for the elastic scattering as a function of the scattering angle and energy as it will be described later in this section.

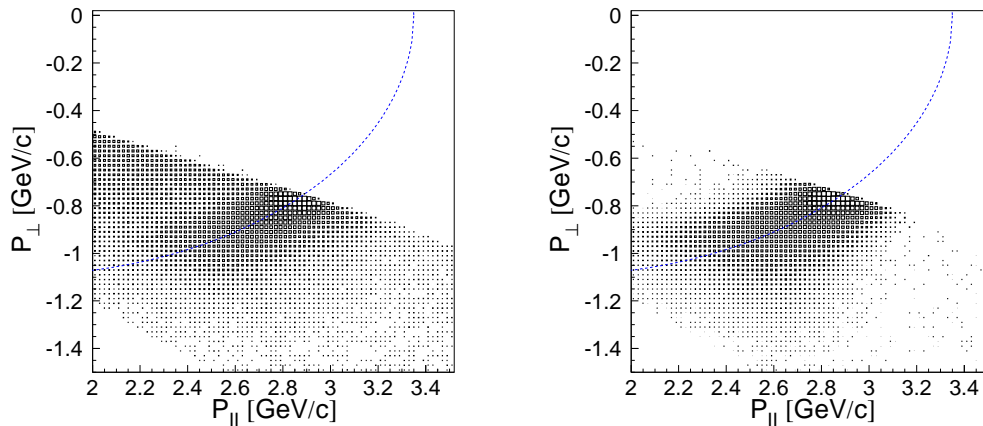


Figure 7.2: Transversal versus parallel momentum component of the reconstructed forward proton momentum as obtained in the experiment (**left**) and in the simulation (**right**)

In proton-proton experiments the elastic scattering $pp \rightarrow pp$ is taken as a reference reaction due to the wealth of high-precision data available from the measurements of the EDDA collaboration [104]. The additional advantage of selecting this channel is the relatively high number of events, being clearly selectable by a coincident detection of both ejectiles. To determine the luminosity, the known differential cross sections for elastically scattered protons are compared to the number of scattered protons from the experimental data.

In case of quasi-free elastic scattering we have to deal with the Fermi motion of the nucleons inside the deuteron. This motion implies that the value of the total energy in

the centre-of-mass system as well as the direction of the centre-of-mass velocity varies from event to event. To demonstrate the momentum spread caused by the Fermi motion let us consider the equivalent effective beam momentum as it is seen from the proton inside the deuteron. Figure 7.3 shows the distribution of the effective beam momentum for the quasi-free proton-proton scattering at the nominal value of the beam momentum equal to 3.35 GeV/c. The momentum changes significantly from 2.2 GeV/c up to 4.5 GeV/c, therefore this effect cannot be neglected. At this point we have to emphasise that due to this effect, in a single subrange of the scattering angle in the laboratory system there are events originating from scattering at different values of the total energy \sqrt{s} , as well as different scattering angles in the proton-proton centre-of-mass system.

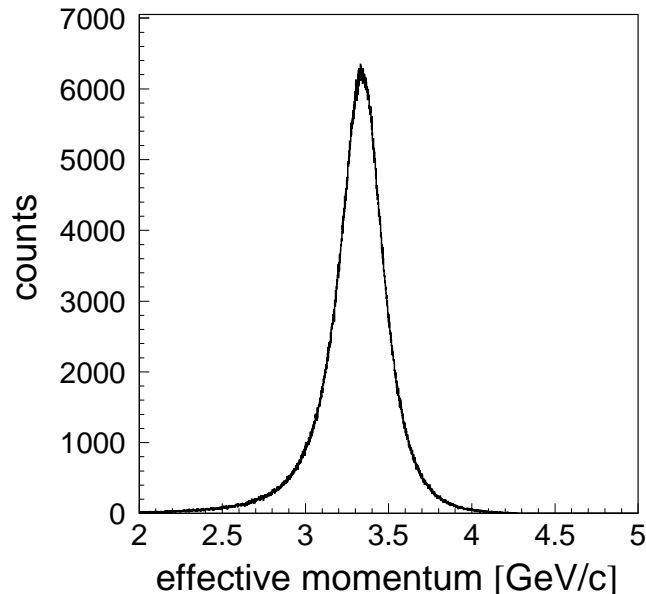


Figure 7.3: Distribution of the effective beam momentum for the quasi-free proton-proton scattering at the nominal proton beam momentum of $p_{beam} = 3.35$ GeV/c as it is seen from the proton in the target.

Therefore in order to calculate the integral luminosity we have to perform simulations taking into account these effects. Each simulated event has been associated with a weight corresponding to the differential cross section which is a function of the scattering angle and the total energy in the proton-proton centre-of-mass system \sqrt{s} [107]. For this purpose we have used cross section values for the $pp \rightarrow pp$ reaction computed by means of the SAID programme [108] because the accessible data base of the EDDA collaboration was insufficient. As it is seen in figure 7.3 the effective beam momentum which is seen from the nucleon inside the deuteron changes from 2.2 GeV/c up to 4.2 GeV/c whereas EDDA measurements were performed in the beam momentum range from 0.712 GeV/c to 3.387 GeV/c.

In order to calculate the integrated luminosity, available range of the x-coordinate along the S1 detector has been divided into four subranges. Further on, in order to separate the background originating from multi-particle reactions, the projection of the distance of the points from the kinematical ellipse was extracted for each subrange separately. The results for two subranges are shown in figure 7.4. Next, after the background subtraction the real number of scattered events $\Delta N_{exp}(\theta_{lab})$ into a given subrange of the S1 detector has been obtained.

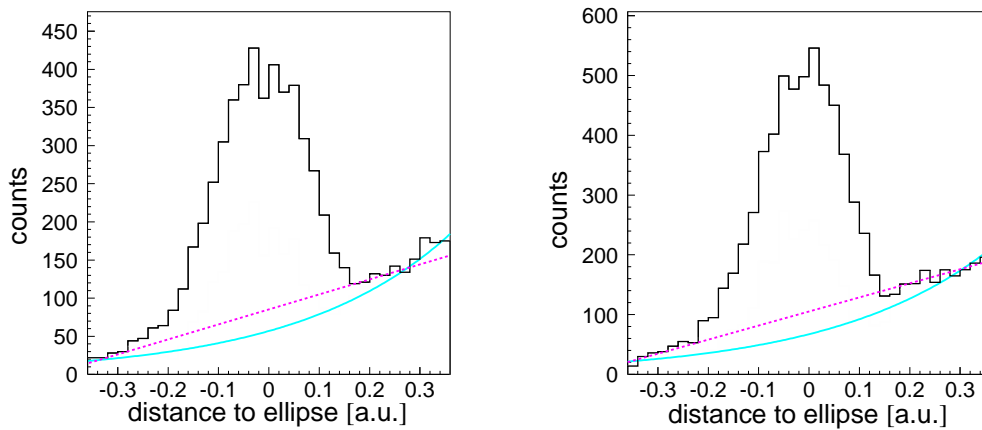


Figure 7.4: Projection of the experimental event distribution from fig. 7.2 (left) along the expected kinematical ellipse for two subranges of the S1 detector. The dash lines depict the background as interpreted under the assumption that it is linear. The solid lines outline the background described by an exponential function.

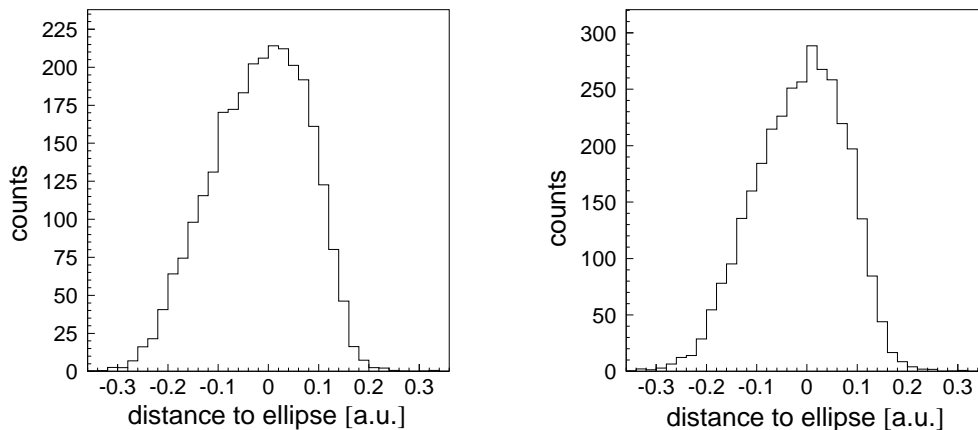


Figure 7.5: Projection of the simulated event distribution from fig. 7.2 (right) onto the expected kinematical ellipse for two subranges of the S1 detector.

In order to determine the $\Delta N_{MC}(\theta_{lab})$ number, we have simulated $N_0 = 10^8$ quasi-free $pp \rightarrow pp$ events, which have been analysed using the same procedure as in case of the experimental data and which were weighted with the values of the differential cross sections expressed in units of mb. The results for analogous subranges as for the experimental distributions are shown in figure 7.5.

The integrated luminosity was calculated as follows [107]:

$$L = \frac{N_0 \Delta N_{exp}(\theta_{lab})}{2\pi \Delta N_{MC}(\theta_{lab})} = \frac{N_0 \Delta N_{exp}}{2\pi \int_{\Delta\Omega(\theta_{lab}, \phi_{lab})} \frac{d\sigma}{d\Omega}(\theta^*, \phi^*, p_F, \theta_F, \phi_F) f(p_F, \theta_F, \phi_F) dp_F d\cos\theta_F d\phi_F d\phi^* d\cos\theta^*} \quad (7.1)$$

We have determined the integral luminosity for all subranges of the S1 detector individually. The weighted average integrated luminosity equals to $L = (4.77 \pm 0.06) \times 10^{36} cm^{-2}$. The estimated uncertainty is statistical only.

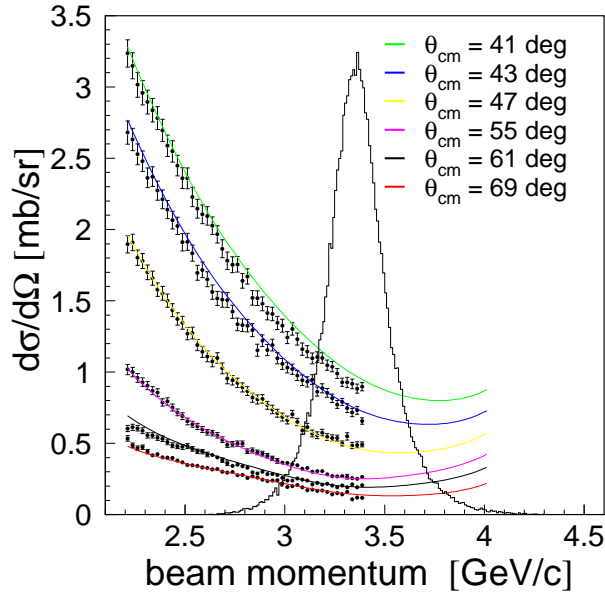


Figure 7.6: Differential cross sections as a function of the beam momentum for a few values of the scattering angle θ_{cm} in the centre-of-mass system. Black points stand for EDDA collaboration data [104], lines denote SAID calculations [108]. Distribution of the effective beam momentum for quasi-free $pp \rightarrow pp$ reaction calculated at the beam momentum of 3.35 GeV/c is also superimposed in the figure.

In addition we have estimated the systematic uncertainty. One of the possible sources of the systematic error may be attached to the background subtraction. For the evaluation of this systematic uncertainty, we have subtracted the background in two

ways, namely in one case the background was described by an exponential function, in the latter case we assumed a linear background (compare the dash and solid lines in figure 7.4). Finally the systematic error due to the background subtraction estimated as the difference between the results determined with the two methods is not larger than $\pm 4\%$.

The systematic error originating from the assumption of the potential model of the nucleon bound inside the deuteron is equal to about 2% [82]. Another source of the systematic error originates from the approximation of the differential cross section by the calculations using the SAID procedure [108]. The total cross section for the proton-proton scattering process has been measured up to beam momentum $p_{beam} \approx 3.4$ GeV/c, whereas the effective beam momentum for the studied reaction ranges up to 4.2 GeV/c. Therefore for events with effective $p_{beam} \geq 3.4$ GeV/c the differential cross sections were interpolated using the SAID programme. Figure 7.6 shows a comparison of the existing differential cross section from the EDDA measurement and the SAID calculations. In the same figure the distribution of the effective beam momentum is also shown. In order to estimate this uncertainty, we have calculated the luminosity assuming a linear dependence between the $\frac{d\sigma}{d\Omega}$ and the momentum for events with effective beam momentum larger than 3.0 GeV/c. Performed calculations show that the result obtained under this assumption differs from the result presented above by 5%.

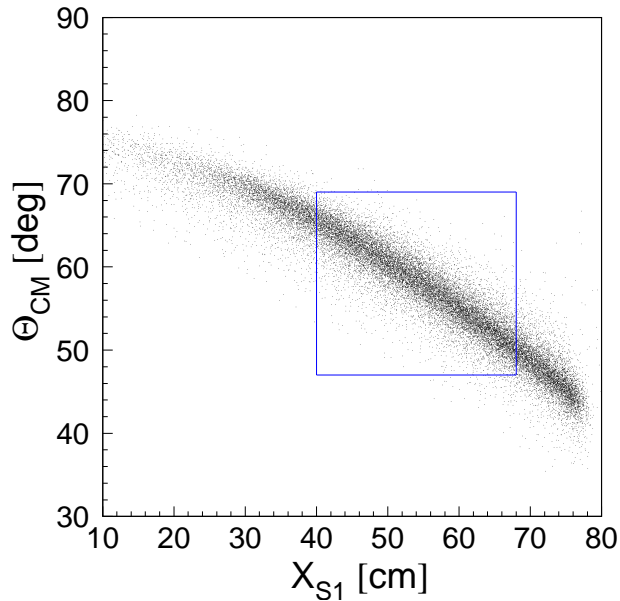


Figure 7.7: Relation between the centre-of-mass scattering angle and the position in the S1 detector for the quasi-free proton-proton scattering at $p_{beam} = 3.35$ GeV/c as has been obtained from Monte Carlo simulations of the quasi-free $pd \rightarrow ppn_{sp}$ reaction.

To reduce this systematic error as much as possible, events with such scattering

angles in the centre-of-mass system θ_{cm} have been selected for which the differential cross sections calculated using the SAID programme are in agreement with the $\frac{d\sigma}{d\Omega}(p)$ distributions measured by the EDDA collaboration (see figure 7.6). Figure 7.7 shows the relation between the available range of the θ_{cm} angles and the position in the S1 detector for the quasi-free proton-proton scattering at $p_{beam} = 3.35$ GeV/c as has been obtained in the Monte Carlo simulation. The rectangular area denotes the applied cut on the position in the S1 detector, which restricts the θ_{cm} angle to the range from 48 to 69 degrees a good agreement between the SAID calculations and EDDA data is given. Summarizing, we have estimated the overall systematic error of the integrated luminosity to be 7%.

8. Excitation function

In the following section we estimate the upper limit of the total cross section for the quasi-free $pn \rightarrow pn\eta'$ reaction as a function of the excess energy. Furthermore, an upper limit of the ratio $R_{\eta'} = \frac{\sigma(pn \rightarrow pn\eta')}{\sigma(pp \rightarrow pp\eta')}$ will be determined and compared to the analogous ratio calculated for the η meson [12, 42].

8.1 Upper limit of the total cross section

The total cross section for the $pn \rightarrow pn\eta'$ reaction was calculated using the formula:

$$\sigma^{TOT}(Q_{cm}) = \frac{N^{\eta'}}{L_{int} \times E_{eff}}, \quad (8.1)$$

where $N^{\eta'}$ is the number of η' mesons for a given excess energy Q_{cm} , L_{int} is the luminosity integrated over the time of the measurement and E_{eff} is the detection efficiency including the geometrical acceptance of the detector system.

The luminosity was established from the number of the quasi-free proton-proton scattering events (see chapter 7). The acceptance of the detector setup and efficiency was determined based on Monte Carlo studies. After subtracting the missing mass distributions for the negative values of Q_{cm} from the spectra for positive values of Q_{cm} – due to the very low signal-to-background ratio – the signal from the η' meson was found to be statistically insignificant. Therefore, we estimate the upper limit of the total cross section for the quasi-free $pn \rightarrow pn\eta'$ reaction.

The number of the η' mesons can be calculated as the difference between the number of events (N^{SIG}) in the peak for the signal (solid line in figure 6.11) and the number of events (N^{BACK}) of the background in the peak (dash line in figure 6.11):

$$N^{\eta'} = N^{SIG} - N^{BACK}; \quad \sigma N^{\eta'} = \sqrt{N^{SIG} + N^{BACK}} \quad (8.2)$$

The range for the integration has been chosen based on the simulation of the missing mass distributions (see figure 6.13). Assuming that in the experiment no η' mesons are observed ($N^{\eta'} = 0$) the $\sigma N^{\eta'}$ value was used to determine the upper limit of the total cross section for the $pn \rightarrow pn\eta'$ reaction at a 90% confidence level. The result is shown in figure 8.1 and in table 8.1.

Q_{cm} [MeV]	upper limit of $\sigma(pn \rightarrow pn\eta')$ at 90% CL [nb]
[0, 8)	63
[8, 16)	197
[16, 24)	656

Table 8.1: Upper limit of the total cross section for the $pn \rightarrow pn\eta'$ reaction as a function of the excess energy. The excess energy intervals correspond to the binning applied.

The horizontal bars in figure 8.1 represents the intervals of the excess energy, for which the upper limit of the total cross section was calculated.

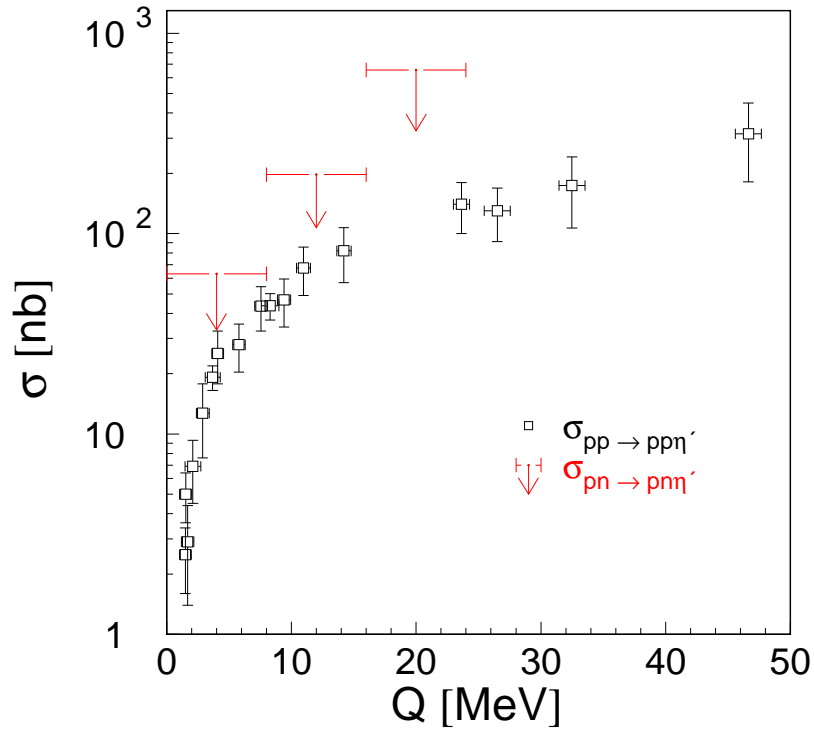


Figure 8.1: Total cross sections for the $pp \rightarrow pp\eta'$ reaction as a function of the excess energy (black open squares). Upper limit for the total cross section for the $pn \rightarrow pn\eta'$ reaction as a function of the excess energy (red dots).

The efficiency and the acceptance of the COSY-11 detector system was estimated based on Monte Carlo simulations. The error of the detection efficiency (σE_{eff}) is determined to be 3%. The main contribution of this systematic error comes from the un-

certainty in the efficiency in the neutron registration, as was discussed in section 5.3.4. The total systematic error of $\sigma^{TOT}(Q_{cm})$ was estimated as the quadratic sum of independent systematic errors originating from luminosity calculation ($\sigma_{L_{int}} \approx 7\%$), determination of the efficiency ($\sigma_{E_{eff}} \approx 3\%$) and estimation of the number of η' mesons ($\sigma_{N^{\eta'}} \approx 6\%$) and is equal to $\approx 10\%$.

8.2 Ratio

Figure 8.2 presents the upper limit of the ratio $R_{\eta'} = \frac{\sigma(pn \rightarrow pn\eta')}{\sigma(pp \rightarrow pp\eta')}$ of the total cross section for the $pn \rightarrow pn\eta'$ and $pp \rightarrow pp\eta'$ reaction as a function of the excess energy (red crosses). Analogous ratios but for the η meson are also shown as open squares.

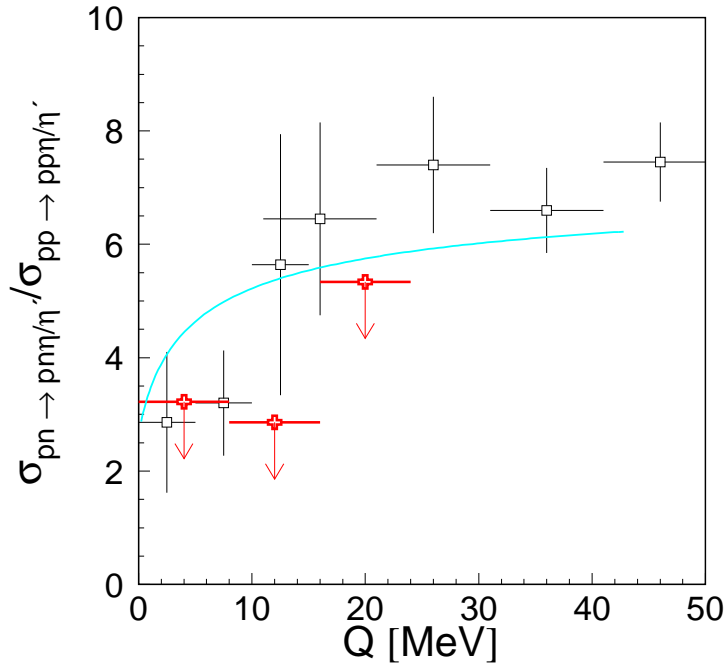


Figure 8.2: Upper limit of the ratio ($R_{\eta'}$) of the total cross sections for the $pn \rightarrow pn\eta'$ and $pp \rightarrow pp\eta'$ reactions (red crosses) in comparison with the ratio (R_{η}) determined for the η meson (open squares). The superimposed line indicates a result of the fit to the $R_{\eta'}$ data taking into account the final state interaction of nucleons [42].

The total cross section for the $pp \rightarrow pp\eta'$ reaction was measured in former experiments [13, 14, 15, 16, 17]. It reveals a strong excess energy dependence, especially very close to threshold and hence this dependence must be taken into account when

comparing to the results for the $pn \rightarrow pn\eta'$ reaction which were established for 8 MeV excess energy intervals. Therefore, for a given interval of excess energy, we have determined the mean value of the total cross section for $pp \rightarrow pp\eta'$ reaction using the parametrisation of Fäldt and Wilkin fitted to the experimental data [44, 45] (for details see appendix B).

Q_{cm} [MeV]	upper limit of $\sigma(pn \rightarrow pn\eta')$ at 90% CL [nb]	$\sigma(pp \rightarrow pp\eta')$ [nb]	upper limit of $R_{\eta'}$ at 90% CL
[0, 8)	63	19.6	3.2
[8, 16)	197	68.7	2.9
[16, 24)	656	122.7	5.3

Table 8.2: The columns of the table include from left to right: Excess energy range; Upper limit of the total cross section for the $pn \rightarrow pn\eta'$ reaction; Mean value of the $pp \rightarrow pp\eta'$ total cross section according to the parametrisation given in section B.2; Upper limit of the ratio $R_{\eta'}$ as a function of the excess energy.

The determined $pp \rightarrow pp\eta'$ total cross section values together with the upper limit of the ratio $R_{\eta'}$ are presented in table 8.2. In case of the η meson, the ratio of the total cross sections for the reactions $pn \rightarrow pn\eta$ and $pp \rightarrow pp\eta$ was determined to be $R_{\eta} \approx 6.5$ at excess energies larger than ≈ 15 MeV [12], what suggests the dominance of the isovector meson exchange in the production mechanism, whereas close to threshold the ratio falls down to about $R_{\eta} \approx 3$ [42]. This decrease may be explained by the different energy dependence of the proton-proton and proton-neutron final state interactions [44, 45]. For the η' meson the upper limit of the ratio for the excess energy range from 0 MeV to 8 MeV is nearly equal to values of the ratio obtained for the η meson, whereas for larger excess energies (from 8 MeV to 24 MeV) the ratio is notably lower.

9. Comparison with model predictions

The total cross section for the $pn \rightarrow pn\eta'$ reaction close to the threshold appeared to be too small to reveal a signal in the missing mass spectrum with the statistics achieved in the discussed experiment.

The established upper limit does not allow to verify the scenario of the production via the possible gluonic component in the η' wave function [9, 10]. However, the results also do not exclude this hypothesis and may be treated as a promising finding in this context since the established upper limits for the ratio $R_{\eta'}$ are lower than the values of the ratio for the η meson.

Recently, X. Cao and X. G. Lee [7] performed an analysis of $pN \rightarrow pN\eta'$ and $\pi N \rightarrow N\eta'$ reactions within an effective Lagrangian approach, assuming that the $S_{11}(1535)$ resonance is dominant in the η' production. Numerical results show that the π exchange is most important in the $pN \rightarrow pN\eta'$ process and predict a large ratio of $\sigma(pn \rightarrow pn\eta')$ to $\sigma(pp \rightarrow pp\eta')$ equal to $R_{\eta'} = 6.5$ in the excess energy range from 0 MeV to 160 MeV. Thus the authors assumed that the production of the η' meson proceeds in the same way as the production of the η meson, and as a consequence predicted a $R_{\eta'}$ value equal to the experimentally established R_{η} value.

Yet, the experimentally determined upper limit of $R_{\eta'}$ being the result of this thesis is considerably lower than the $R_{\eta'} = 6.5$ predicted in reference [7]. Therefore, on this stage of knowledge we can exclude the hypothesis that the dominant production mechanism of the η' meson in nucleon-nucleon collisions is associated with the excitation and de-excitation of the $S_{11}(1535)$ resonance.

Another model has been elaborated by L. P. Kaptari and B. Kämpfer [6], considering the production of the η' meson in the $pp \rightarrow pp\eta'$ and $pn \rightarrow pn\eta'$ reactions close to threshold by analysing the data within a covariant effective meson-nucleon theory by including meson and nucleon currents with resonances $S_{11}(1650)$, $P_{11}(1710)$ and $P_{13}(1720)$. In the framework of this model a reasonable agreement with data on $pp \rightarrow pp\eta'$ has been achieved with a contribution of the meson conversion currents. The total contribution of nucleonic and resonance currents was found to be small.

The predictions for the $pn \rightarrow pn\eta'$ reaction, based on this model [6] are seen as a dotted line in figure 9.1, and are confronted with the upper limits of the total cross sections for the $pn \rightarrow pn\eta'$ reaction (left) and the upper limits of the ratio $R_{\eta'}$ (right).

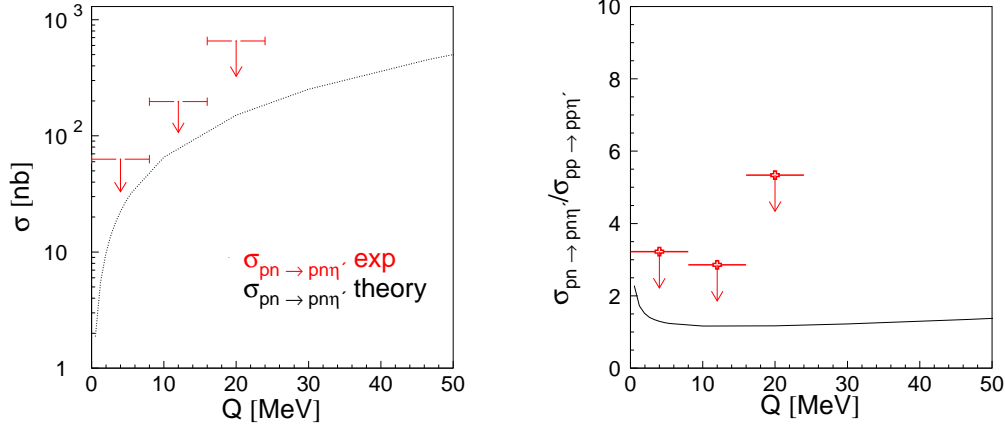


Figure 9.1: (Left:) Upper limit of the total cross section for the $pn \rightarrow pn\eta'$ reaction in comparison to calculations assuming that the η' production mechanism is associated with meson exchange [6]. **(Right:)** Upper limit of the ratio ($R_{\eta'}$) of the total cross sections for the $pn \rightarrow pn\eta'$ and $pp \rightarrow pp\eta'$ reactions (red crosses). The dotted line represents results of calculations from [6].

The experimentally determined values of the total cross sections for the $pn \rightarrow pn\eta'$ reaction, as well as the results achieved for the ratio $R_{\eta'}$ do not exclude the calculations of ref. [6].

For the $pp \rightarrow pp\eta'$ reaction, calculations of K. Nakayama and collaborators [41] yields the $S_{11}(1650)$ resonance as the dominant contribution to the production current, whereas the $P_{11}(1880)$ resonance, mesonic and nucleonic currents were found to be much smaller. The combined analysis of the $pp \rightarrow pp\eta'$ reaction and photoproduction reactions was crucial for these findings. The details of the excitation mechanism of the S_{11} resonance, however, are not constrained by the currently existing data. As the authors pointed out [41], to learn more about the relevant excitation mechanism, observables other than the cross sections, such as the invariant mass distribution [48] are necessary.

10. Summary and perspectives

The main goal of this dissertation is the determination of the excitation function of the total cross section for the quasi-free $pn \rightarrow pn\eta'$ reaction near the kinematical threshold. The motivation of the presented experiment was the comparison of the $pp \rightarrow pp\eta'$ and $pn \rightarrow pn\eta'$ total cross sections in order to learn about the production mechanism of the η' meson in the channels of isospin $I = 1$ and $I = 0$ and to investigate aspects of the gluonium component of the η' meson.

The experiment, which is described in this thesis has been performed at the cooler synchrotron COSY in the Research Centre Jülich by means of the COSY-11 detector system. For the purpose of this experiment the standard COSY-11 detector setup was extended by the neutral particle and spectator detectors. The quasi-free $pn \rightarrow pn\eta'$ reaction has been induced by a proton beam with a momentum of 3.35 GeV/c in a deuteron target. All outgoing nucleons have been registered by the COSY-11 detectors, whereas for the η' meson identification the missing mass technique was applied.

The upper limit of the total cross section for the $pn \rightarrow pn\eta'$ reaction in the excess energy range between 0 and 24 MeV determined for the first time ever is presented in this thesis. Having the total cross section for the $pp \rightarrow pp\eta'$ reaction in the same energy range, measured in previous experiments, the upper limit of the ratio $R_{\eta'} = \sigma(pn \rightarrow pn\eta') / \sigma(pp \rightarrow pp\eta')$ has been estimated. The achieved result differ from the analogous ratio R_{η} obtained for the η meson. This allows to conclude that the production mechanism of these mesons in nucleon-nucleon collisions are different and the meson η' is not dominantly created via the excitation of the $S_{11}(1535)$ resonance as it is the case for the η meson.

It is also shown, that the theoretical predictions assuming the production mechanism to be associated with the fusion of virtual mesons or with glue excited in the interaction region of the colliding nucleons are not excluded by the experimental data. However, it is not possible to distinguish between these mechanisms based on the existing data. This conclusion calls for further theoretical as well as experimental investigations.

For quantitative tests of these mechanisms an order of magnitude larger statistics and a larger energy range would be required. This can be reached with the WASA-at-COSY facility.

In parallel to the investigation of the $pn \rightarrow pn\eta'$ reaction, presented in this thesis, we have extended the experimental studies to a pure isospin zero state of the interacting nucleons by the measurement of the quasi-free $pn \rightarrow d\eta'$ reaction. This experiment was conducted using the proton beam with a momentum of 3.365 GeV/c and a deuteron target. Assuming that the ratio of the cross sections for the $pn \rightarrow d\eta'$ and $pp \rightarrow pp\eta'$ reactions will be in the same order of magnitude as the ratio already established [12] for the $pn \rightarrow d\eta$ and $pp \rightarrow pp\eta$ reactions it is expected to identify about 1000 $pn \rightarrow d\eta'$

events in the data sample [109].

Together with the results of the $pp \rightarrow pp\eta'$ and $pn \rightarrow pn\eta'$ reactions we would then complete the study of the η' meson production cross section in nucleon-nucleon collisions. This will further reduce significantly the ambiguities of theoretical models and will lead to a better understanding of the production mechanism of the η' meson in nucleon-nucleon collisions. The result will also be of importance for rate estimates for studying the η' meson decays with the WASA-at-COSY facility [67, 110].

A. Precision of the neutron momentum determination

The experimental precision of the missing mass determination of the $pn \rightarrow pnX$ reaction strongly relies on the accurate measurement of the momentum of neutrons. The neutron detector is designed to deliver the information about the time at which the registered neutron or gamma quantum induced a hadronic or electromagnetic reaction. The time of the reaction combined with this information allows to calculate the time-of-flight (TOF^N) of the neutron (or gamma) on the 7.36 m distance between the target and the neutron detector. Therefore the accuracy of the time-of-flight depends on *a*) the neutron detector time resolution and *b*) the time resolution of the S1 counter. The neutral particle detector time resolution was determined to be 0.4 ns [91] which corresponds to the time of flight in the scintillator material for a gamma quantum on a distance of a size of a single module. The neutron path (l) is defined as the distance between the position of the centre of the target-beam overlap and the centre of the module which provided a signal as the first one. The accuracy of this measurement amounts approximately to half the size of the module which is 4.5 cm. In case of neutrons the absolute value of the momentum (p) can be expressed as:

$$p = m \cdot \frac{l}{TOF^N} \cdot \frac{1}{\sqrt{1 - (\frac{l}{TOF^N})^2/c^2}}, \quad (\text{A.1})$$

where m denotes the mass of the neutron, l stands for the distance between the target and the neutral particle detector and TOF^N is the time-of-flight of the particle. Monte Carlo studies of the quasi-free $pp \rightarrow pp$ reaction via the $dp \rightarrow ppn_{spec}$ process have been performed in order to establish the momentum resolution of the neutron detector. A spectator neutron has been denoted as n_{spec} . This reaction was chosen since it could be identified in the data taken during previous COSY-11 measurements conducted with the deuteron beam [111], and hence the simulation results could have been corroborated by the experimental data [79]. The detection of both outgoing protons from the $dp \rightarrow ppn_{sp}$ reaction proceeds via the well established method [62] and the spectator neutron is measured by the neutral particle detector [79].

Figure A.1 (left) presents the difference ($\Delta P = P_{gen} - P_{rec}$) between the generated neutron momentum (P_{gen}) and the reconstructed neutron momentum from signals simulated in the detectors (P_{rec}). The value of (P_{rec}) was calculated taking into account the time resolution of the neutral particle detector ($\sigma = 0.4$ ns) [91] as well as the time resolution of the S1 counter ($\sigma = 0.25$ ns) [77]. The time at which the proton hits the S1 detector is needed to determine the time of the reaction in the target place. The distribution of ΔP – for neutrons possessing a momentum of 1.6 GeV/c – was fitted by a Gaussian function resulting in a momentum resolution of $\sigma(P) = 0.14$ GeV/c [79]. The

accuracy of the TOF^N measurement is approximately independent of the momentum of neutron, however, the relative resolution for determining the neutron momentum alters significantly as its momentum changes. This fractional momentum resolution – which is shown in figure A.1 (right) as a function of the neutron momentum – is given by the equation:

$$\frac{\sigma p}{p} = \frac{\frac{dp}{dt} \cdot \sigma_t}{p}, \quad (\text{A.2})$$

where $\sigma_t = \sqrt{\sigma_n^2 + \sigma_{S1}^2}$ accounts for the time resolution of both the neutral particle and the S1 detectors. The result presented in figure A.1 was obtained assuming that $\sigma_n = 0.4$ ns, $\sigma_{S1} = 0.25$ ns, and $l = 7.54$ m. The value of l corresponds to the distance between the target and the centre of the neutron detector.

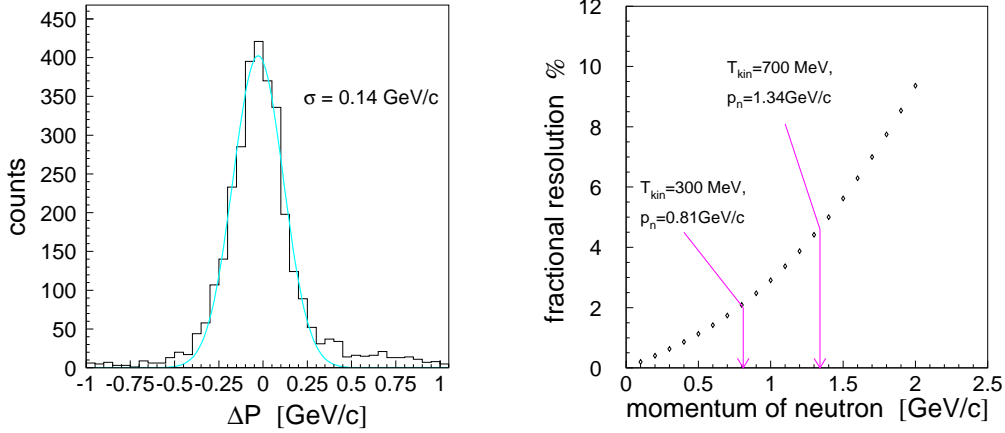


Figure A.1: **Left:** Difference between generated (P_{gen}) and reconstructed (P_{rec}) neutron momenta for the $dp \rightarrow p p n_{spec}$ reaction. **Right:** Fractional momentum resolution of the neutral particle detector as a function of neutron momentum. Arrows depict the kinetic energy and momentum range of neutrons originating from $pd \rightarrow p_{sp} p n \eta'$ reaction at the beam momentum of 3.35 GeV/c.

This fractional resolution depends on the neutron momentum and e.g. for the neutrons produced at threshold for the $pn \rightarrow pn\eta$ reaction ($p = 0.76$ GeV/c) it amounts to 2% and at threshold of the $pn \rightarrow pn\eta'$ reaction ($p = 1.06$ GeV/c) it is equal to 3.2%

B. Parameterisation of the $pp \rightarrow pp\eta'$ total cross section

In general the total cross section is defined as an integral of the probabilities to populate a given phase space interval over the whole kinematically available range normalised to the flux factor F according to formula:

$$\sigma(Q) = \frac{1}{F} \int dV_{ps} |M|^2, \quad (\text{B.1})$$

where $|M|^2$ denotes the production amplitude and V_{ps} is the phase space volume. Figure B.1 shows the total cross section for the $pp \rightarrow pp\eta'$ reaction as a function of the excess energy. It is clearly seen that near threshold the η' production strongly depends on the energy.

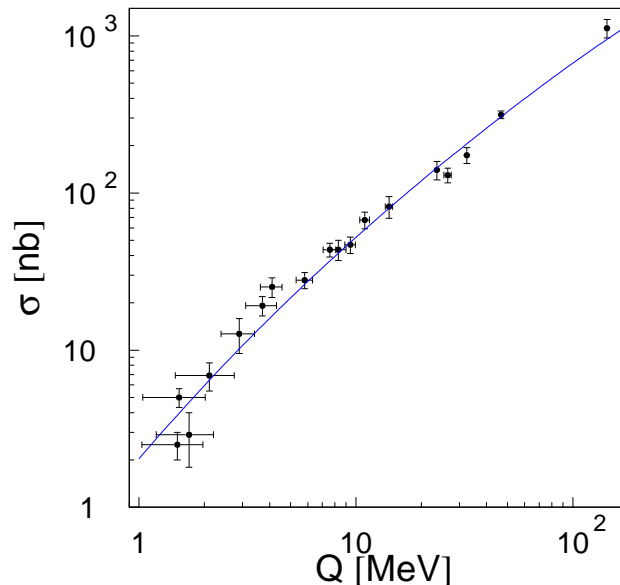


Figure B.1: Total cross sections for the $pp \rightarrow pp\eta'$ reaction as a function of the excess energy derived from the COSY-11, DISTO and SPESIII measurements [13, 14, 15, 16, 17]. The solid line depicts a parameterisation of the total cross section using formula B.2

The solid line depicts a parameterisation of the total cross section utilizing a factorisation of the production matrix element $|M|$ into the short range primary amplitude and the initial and final state interaction. The proton-proton FSI has been taken into

account according to the Fäldt and Wilkin model [44, 45] using the following formula:

$$\sigma(Q) = C_1 \frac{V_{ps}}{F} \left(1 + \sqrt{1 + \frac{Q}{\varepsilon}}\right)^{-2} = C_2 \frac{Q^2}{\sqrt{\lambda(s, m_1^2, m_2^2)}} \left(1 + \sqrt{1 + \frac{Q}{\varepsilon}}\right)^{-2} \quad (\text{B.2})$$

where C_1 , C_2 and ε have to be determined from the data, and the triangle function $\lambda(x, y, z)$ [112] is defined as:

$$\lambda(x, y, z) = x^2 + y^2 + z^2 - 2xy - 2xz - 2yz. \quad (\text{B.3})$$

The function B.2 was fitted to the data and as a result values of the free parameters C_2 and ε have been obtained [113]:

$$\begin{aligned} \varepsilon &= (0.62 \pm 0.13) \text{ MeV} \\ C_2 &= (84 \pm 14) \text{ mb} \end{aligned}$$

Applying the parameterisation from equation B.2 with known values of C_2 and ε one can compute the total cross section for the η' meson production at any value of the excess energy close to threshold.

At the end of this thesis, I would like to express my gratitude to a large number of people without whom this work wouldn't have been possible.

First of all, I want to express my profound gratitude to Prof. Paweł Moskal for the great help and invaluable advices toward bringing this dissertation to fruition, for the enormous patience and for encouraging me to succeed in achieving high goals. It was a great pleasure but above all a honour to work with You, Paweł. You are an example to follow as a scientist and educator.

I would like to express my deeply gratitude to Prof. Walter Oelert for giving me the opportunity to work within the COSY-11 group. I am also indebt for comments, valuable advice and encouragement.

Less direct but not less important has been the inspiration of Dr. Steven D. Bass.

I have also benefited from the great help and advice of Dr. Rafał Czyżykiewicz.

I am also very grateful to Prof. Paweł Moskal, Prof. Walter Oelert, Prof. Jerzy Smyrski, Dr. Dieter Grzonka and Dr. Steven D. Bass for careful reading and correcting this manuscript.

I want to express my appreciation to my Friends and Colleagues from the COSY-11 group with whom I have the great fortune to interact and work.

Dziękuję mojej Mamie za wsparcie podczas tych kilku lat studiów i nieustanną troskę. Dziękuję bratu Michałowi, że na mnie poczekał.

Za miłość, anielską cierpliwość i "doping" dziękuję mojemu kochanemu mężowi.

References

- [1] C. Amsler *et al.*, Phys. Lett. **B 667**, 1 (2008).
- [2] D. Du, Y. Yang, G. Zhu, Phys. Rev. **D 59**, 014007 (1999).
- [3] P. Ball, J. M. Frere and M. Tytgat, Phys. Lett. **B 365**, 367 (1996).
- [4] H. Fritzsch, Phys. Lett. **B 415**, 83 (1997).
- [5] K. Nakayama *et al.*, Phys. Rev. **C 61**, 024001 (2000).
- [6] L. P. Kaptari, B. Kämpfer, Eur. Phys. J. **A 37**, 69 (2008).
- [7] Xu Cao and Xi-Guo Lee, Phys. Rev. **C 78**, 035207 (2008).
- [8] P. Moskal, Habilitation thesis, Jagiellonian University, (2004),
e-Print: **hep-ph/0408162**.
- [9] S. D. Bass, Phys. Scripta **T 99**, 96 (2002).
- [10] S. D. Bass, Acta Phys. Polon. **B Proc. Supp. 2**, 11 (2009),
e-Print: **arXiv:0812.5047** [hep-ph].
- [11] S. D. Bass, Phys. Lett. **B 463**, 286 (1999).
- [12] H. Calén *et al.*, Phys. Rev. **C 58**, 2667 (1998).
- [13] P. Moskal *et al.*, Phys. Lett. **B 474**, 416 (2000).
- [14] A. Khoukaz *et al.*, Eur. Phys. J. **A 20**, 345 (2004).
- [15] F. Balestra *et al.*, Phys. Lett. **B 491**, 29 (2000).
- [16] P. Moskal *et al.*, Phys. Rev. Lett. **80**, 3202 (1998).
- [17] F. Hibou *et al.*, Phys. Lett. **B 438**, 41 (1998).
- [18] M. Zieliński, Diploma thesis, Jagiellonian University, **Jül-4277** (2008).
- [19] G. R. Kalbfleisch *et al.*, Phys. Rev. Lett. **12**, 527 (1964).

-
- [20] M. Goldberg *et al.*, Phys. Rev. Lett. **12**, 546 (1964).
- [21] F. J. Gilman and R. Kauffman, Phys. Rev. **D 36**, 2761 (1987).
- [22] J. L. Rosner, Phys. Rev. **D 27**, 1101 (1983).
- [23] A. Bramon, R. Escribano, M.D. Scadron, Eur. Phys. J. **C 7**, 271 (1999).
- [24] B. H. Behrens *et al.*, Phys. Rev. Lett. **80**, 3710 (1998).
- [25] C. P. Jessop *et al.*, Phys. Rev. **D 58**, 052002 (1998).
- [26] G. Brandenburg *et al.*, Phys. Rev. Lett. **75**, 3804 (1995).
- [27] S. Weinberg, Phys. Rev. **D 11**, 3583 (1975).
- [28] G. 't Hooft, Phys. Rev. Lett. **37**, 8 (1976).
- [29] E. Witten, Nucl. Phys. **B 156**, 269 (1979).
- [30] G. Veneziano, Nucl. Phys. **B 159**, 213 (1979).
- [31] S. L. Adler, Phys. Rev. **177**, 2426 (1969).
- [32] E. Kou, Phys. Rev. **D 63**, 054027 (2001).
- [33] D. Atwood and A. Soni, Phys. Lett. **B 405**, 150 (1997).
- [34] F. Ambrosino *et al.*, Phys. Lett. **B 648**, 267 (2007).
- [35] G. M. Shore and G. Veneziano, Nucl. Phys. **B 381**, 23 (1992).
- [36] S. Ozuka, Phys. Lett. **5**, 165 (1963).
- [37] G. Zweig, CERN Report No. TH412 (1964).
- [38] J. Iizuka, Prog. Theor. Phys. Suppl. **37–38**, 21 (1966).
- [39] S. D. Bass, "The spin structure of the proton", World Scientific (2007).
- [40] J. Ashman *et al.*, Phys. Lett. **B 206**, 364 (1988).
- [41] K. Nakayama *et al.*, Phys. Rev. **C 69**, 065212 (2004).
- [42] P. Moskal *et al.*, Phys. Rev. **C 79**, 015208 (2009).
- [43] R. Czyżykiewicz and P. Moskal, Acta Phys. Polon. **B Proc. Supp. 2**, 39 (2009),
e-Print: [arXiv:0905.2500](https://arxiv.org/abs/0905.2500) [nucl-ex].
- [44] G. Fäldt and C. Wilkin, Phys. Lett. **B 382**, 209 (1996).

- [45] G. Fäldt and C. Wilkin, Phys. Rev. C **56**, 2067 (1997).
- [46] R. Czyżykiewicz *et al.*, Phys. Rev. Lett. **98**, 122003 (2007).
- [47] S. D. Bass, A. W. Thomas, Phys. Lett. B **634**, 368 (2006).
- [48] P. Klaja, Ph.D. thesis, Jagiellonian University, (2009).
- [49] P. Moskal, M. Wolke, A. Khoukaz, W. Oelert, Prog. Part. & Nucl. Phys. **49**, 1 (2002).
- [50] H. Calén *et al.*, Phys. Rev. Lett. **79**, 2642 (1997).
- [51] J. Stepaniak, H. Calén, Schriften des FZJ, Matter and Materials **21**, 230 (2004).
- [52] S. Häggström, Ph.D. thesis, Uppsala University, Acta Universitatis Upsaliensis 13, (1997).
- [53] J. Smyrski *et al.*, Phys. Lett. B **474**, 182 (2000).
- [54] P. Moskal *et al.*, Phys. Rev. C **69**, 025203 (2004).
- [55] H. Calén *et al.*, Phys. Lett. B **366**, 39 (1996).
- [56] E. Chiavassa *et al.*, Phys. Lett. B **322**, 270 (1994).
- [57] A. M. Bergdolt *et al.*, Phys. Rev. D **48**, R2969 (1993).
- [58] F. Duncan *et al.*, Phys. Rev. Lett. **80**, 4390 (1998).
- [59] M. Abdel-Bary *et al.* Eur. Phys. J. A **29**, 353 (2006).
- [60] M. Lacombe *et al.*, Phys. Lett. B **101**, 139 (1981).
- [61] E. Chiavassa *et al.*, Phys. Lett. B **337**, 192 (1994).
- [62] S. Brauksiepe *et al.*, Nucl. Instr. & Meth. A **376**, 397 (1996).
- [63] P. Klaja *et al.*, AIP Conf. Proc. **796**, 160 (2005).
- [64] J. Smyrski *et al.*, Nucl. Instr. & Meth. A **541**, 574 (2005).
- [65] R. Maier, Nucl. Instr. & Meth. A **390**, 1 (1997).
- [66] http://wasasrv.ikp.kfa-juelich.de/WasaWiki/index.php/Main_Page.
- [67] H.-H. Adam *et al.*, Proposal for WASA-at-COSY, e-Print: **nucl-ex/0411038** (2004).
- [68] <http://www.fz-juelich.de/ikp/anke/de/index.shtml>.

- [69] <http://www.fz-juelich.de/ikp/pisa/pisa.html>.
- [70] <http://www.iskp.uni-bonn.de/gruppen/edda/publ/top.html>.
- [71] http://www.fz-juelich.de/ikp/publications/AR2003/en/vii_collaborations.shtml?jessica.
- [72] http://www.fz-juelich.de/ikp/COSY-TOF/index_e.html.
- [73] <http://usparc.ihep.su/spires/find/experiments/www2?ee=COSY-NESSI>.
- [74] <http://www.fz-juelich.de/ikp/gem/gem.html>.
- [75] <http://www.iskp.uni-bonn.de/gruppen/momo/momo.html>.
- [76] <http://www.iskp.uni-bonn.de/gruppen/hires/index.html>.
- [77] P. Moskal, Ph.D. thesis, Jagiellonian University, **Jül-3685** (1998).
- [78] M. Wolke, Ph.D. thesis, Universität Bonn, **Jül-3532** (1998).
- [79] J. Przerwa, Diploma thesis, Jagiellonian University, **Jül-4141** (2004), e-Print: **hep-ex/0408016**.
- [80] R. Bilger *et al.*, Nucl. Instr. & Meth. **A 457**, 64 (2001).
- [81] M. Sokołowski, FZJ Ann. Rep. 1990, IKP, **Jül-4052**, 219 (1991).
- [82] R. Czyżykiewicz, Diploma thesis, Jagiellonian University, **Jül-4017** (2002).
- [83] J. Smyrski, FZJ Ann. Rep. 2004, IKP, **Jül-4168**, 11 (2005).
- [84] T. Rożek, Ph.D. thesis, University of Silesia, **Jül-4184** (2005).
- [85] T. Rożek *et al.*, Phys. Lett. **B 643**, 251 (2006).
- [86] P. Moskal, FZJ Ann. Rep. 1996, IKP, **Jül-3365**, 35 (1997).
- [87] P. Moskal *et al.*, e-Print: **nucl-ex/0311003** (2003).
- [88] P. Moskal *et al.*, COSY Proposal No. **133** (2003).
- [89] P. Moskal, FZJ Ann. Rep. 2001, IKP, **Jül-3978**, 19 (2002).
- [90] T. Blaich *et al.*, Nucl. Instr. & Meth. **A 314**, 136 (1992).
- [91] T. Rożek and P. Moskal, FZJ Ann. Rep. 2002, IKP, **Jül-4052**, (2003).
- [92] T. Rożek — private communication (2004).

- [93] William R. Leo, "Techniques for Nuclear and Particle Physics Experiments", Springer; 2nd rev. ed. edition (1994).
- [94] T. Tanimori *et al.*, Nucl. Instr. & Meth. **216**, 57 (1983).
- [95] K. Hagiwara *et al.*, Phys. Rev. **D 66**, 010001 (2002).
- [96] CERN Application Software Group, GEANT 3.2, CERN Program Library Writeup Report No. W5013 (1994).
- [97] <http://www.fluka.org>
- [98] J. Zdebik, Diploma thesis, Jagiellonian University, Cracow (2008); e-Print: **arXiv:0811.1377** [physics.ins-det].
- [99] J. Klaja, P. Moskal and J. Zdebik, Acta Phys. Polon. **B Proc. Supp. 2**, 31 (2009), e-Print: **arXiv:0902.3895** [nucl-ex].
- [100] H. Dombrowski *et al.*, Nucl. Instr. & Meth. **A 386**, 228 (1997).
- [101] P. Moskal *et al.*, Nucl. Instr. & Meth. **A 466**, 488 (2001).
- [102] P. Moskal *et al.*, J. Phys. **G 32**, 629 (2006).
- [103] R. Machleidt *et al.*, Phys. Rev. **C 63**, 024001 (2001).
- [104] D. Albers *et al.*, Phys. Rev. Lett. **78**, 1652 (1997).
- [105] A. J. Simon *et al.*, Phys. Rev. **C 48**, 662 (1993).
- [106] H.-H. Adam *et al.*, Phys. Rev. **C 75**, 014004 (2007).
- [107] P. Moskal and R. Czyżykiewicz, AIP Conf. Proc. **950**, 118 (2007).
- [108] The CNS Data Analysis Center, <http://www.gwu.edu>.
- [109] B. Rejdych *et al.*, AIP Conf. Proc. **950**, 127 (2007).
- [110] A. Kupść, P. Moskal, M. Zieliński, e-Print: **arXiv:0803.2673** (2007).
- [111] C. Piskor-Ignatowicz *et al.*, Schriften des FZJ, Matter & Materials **21**, 272 (2004).
- [112] E. Byckling, K. Kajantie, "Particle Kinematics", John Wiley & Sons Ltd. (1973).
- [113] P. Moskal *et al.*, Int. J. Mod. Phys. **A 22**, 305 (2007).

